Padova University
Physics department "Galileo Galilei"

PHYSICS PH.D.

CICLE XIV

Study of the process $B_s \to J/\psi\eta$ at CDF

Coordinator: Ch.mo Prof. Attilio Stella

Supervisor: Ch.mo Prof. Dario Bisello

Ph.D. student: Dr. Roberto Rossin

DECEMBER, 31^{st} 2002

Study of the process $B_s \to J/\psi\eta$ a CDF

Roberto Rossin

December, 31^{st} 2002

Contents

Introduction

The sector of the "beauty" physics is rich of important aspects for the descriptions of the subnuclear world. From the study of the fauna of particles composing this world we can investigate phenomena as the creation of quarkonium states, the oscillation of quantum systems, the violation of discrete symmetries. Since 1977, year of the first observation of a resonance now known as $\Upsilon(1S)$, physicists dealt with these different aspects. This effort recently culminated in the measurement of the CP symmetry violation in $B^0-\overline{B}^0$ systems, which is the only measurement of violation of this symmetry after the one observed in the $K^0-\overline{K}^0$ system in 1964.

For several years, the CDF experiment at Tevatron (Fermilab) produced relevant results also for this kind of physics; mixing measurements on $B^0-\overline{B}^0$, mean lives measurements for $B^\pm$, B^0, Λ_b^0, and observation and characterization of the B_s strange meson and of the charmed one, B_c.
After LEP has been closed, the physics of "beauty" barions, of B_s and of B_c is an exclusive dominion of hadronic colliders as the Tevatron, which with its two detectors CDF and D0 is the only laboratory where new data for this kind of physics are under collection.

The contributes of LEP ad CDF in the sector of B_s physics led to the measurement of the mass and mean life of this particle, but despite the efforts it has not been possible to highlight any mixing phenomena in the $B_s-\overline{B}_s$ system, neither to measure $\Delta\Gamma_s$. The search of CP violating phenomena in these systems will continue with the new data taking just began at Tevatron.

The measurement of the CP asymmetry in the B_s system will allow to improve the knowledge on the parameters of CKM matrix and in particular the measurement of an angle of the second unitarity triangle. The theoretical expectations on this quantities are affected by small uncertainties, so any observed discrepancy from these values will provide an immediate signal of new physics. The decay channels $B_s \to J/\psi\eta^{(\prime)}$ represent the privileged channels for the study of CP violating phenomena even if their signatures are not so favorable as can be the ones of the $B_s \to J/\psi\phi$ decay, since their final states are CP eigenstates; these decays have never been observed and up to now exists only an upper limit on their *branching ratio* set by the L3 experiment.

We present here a search that aims to observe the $B_s \to J/\psi\eta$ decay and measure its *branching ratio*. This work is based on the data collected during 1994-1995 at CDF, for an integrated luminosity equal to 90 pb^{-1}. The theoretical predictions suggest that measurement of the *branching ratio* will be very difficult to perform in this study, as a consequence the search for a CP asymmetry will be a subject for following studies, based on the Run II data now collecting.

This work is structured in the following way.
In the first chapter we present an overview on the mixing and CP violation phenomena

in the Standard Model schema, with a particular attention to the $B_s \to J/\psi\eta^{(\prime)}$ decay channels.
Chapter 2 describes the experimental apparatus, from the Tevatron accelerator to the CDF detector, highlighting to the detectors more involved in this study.
Chapter 3 is devoted to the description of the adopted analysis strategy and of the Monte Carlo simulators.
In the fourth chapter we present the dataset selections and the J/ψ signal reconstruction, a fundamental step of this analysis.
Chapter 5 is dedicated to the reconstruction of the η signal by means of its decay in two photons. This represented the major effort of the whole analysis, given the limited energetic resolution of the CDF calorimeter for low impulse particles.
In chapter 6 we conclude the B_s signal reconstruction and we reconstruct also a reference signal $B^\pm \to J/\psi K^\pm$ in order to proceed to the *branching ratio* estimate.
In chapter 7 we finally present the measurement of limit on the *branching ratio*.

Chapter 1

Mixing and CP violation in the Standard Model

In this chapter a brief review of the flavour mixing and CP symmetry violation among the Standard Model (SM) will be presented; a particular attention will be turned to these phenomena in the B-physics field. In the end the decay channel $B_s \to J/\psi\eta^{(\prime)}$ will be introduced, describing the importance and the present experimental situation.

1.1 Discrete symmetries

The study of the symmetry properties peculiar of the physical phenomena is of great importance as related to conservation laws or to selection rules. In quantum mechanics, considerations based on symmetry of the interactions give hints on the structure of the Hamiltonian. In this contest, few discrete transformations are particularly relevant:

- spatial inversion, described by the parity operator P
- time reversal, described by the operator T
- particle-antiparticle exchange, described by the charge conjugation operator C

CPT theorem imposes, in a relativistic quantum theory, the invariance respect to the combined transformation of the three operators, C, P, T. As an immediate consequence mass and lifetime of particle and antiparticle must be equal. Up to now all the experimental observations obtained in sub-nuclear physics are consistent with this rule.

The three discrete symmetries C, P and T are singularly exact for strong and electromagnetic interactions, while in weak interactions the experimental observations show an evident violation of the symmetries spatial parity and charge conjugation; also for the combination CP a slight violation has been observed. In particular this last aspect has been pointed out in specific systems in the field of subnuclear physics, as neutral K mesons, for which the first observation traces back to 1964 [10] and more recently, for neutral B mesons [11].

This argument will not be touched in this work that can be considered as a first step in the direction of future analysis that will concern CP violation in B_s sector. In the following paragraphs a survey on the phenomenology will be presented.

1.2 "beauty" production at hadronic colliders

After the discovery of the Υ meson [3] in 1977 the physics of the "beauty" has greatly developed at experiments based both on e^+e^- colliders or on hadrons accelerators and colliders. To this field of research two new experiment are now devoted: BaBar and Belle, located at e^+e^- colliders of SLAC and KEK respectively. As regard the hadronic colliders, the UA1 collaboration, since the mid of eighties, showed that many items on the "beauty" sector were opened to the investigation also using high energy proton-antiproton collisions. The detectors at the $p\overline{p}$ collider at CERN were not designed specifically for this goal, neither were the first experiments at Fermilab. Only afterwords the development of the silicon microstrip detectors, placed close to the interaction region, allowed to improve the tracking system in order to identify "beauty" particles. These innovations had been so impressive that now the experiments at Tevatron in this sector are both competitive and complementary to the experiment at e^+e^- colliders. There are several reasons why to study B-physics at hadron colliders. The production cross section of "beauty" at Tevatron σ_b is $\sim 50\ \mu$b, in a rapidity region $|y| \leq 1$ more than 3 order of magnitude over the typical e^+e^- collider cross section which is ~ 1 nb at the energy of the $\Upsilon(4S)$ and ~ 7 nb at the Z^0 pole. Despite this high cross section allows, in 100pb^{-1} of integrated luminosity, to produce around $5 \cdot 10^9$ $b\bar{b}$ pairs, the huge total inelastic cross section $p\overline{p}$ is around three order of magnitude bigger and as a consequence the ways of identifying events containing B-particles at trigger level are extremely difficult. However it is important to notice other interesting elements characterizing the hadronic colliders in this sector:

- unlike from what happens at e^+e^- accelerators at $\Upsilon(4S)$ energy, at hadron colliders B-particles are produced in all species, B_s and B_d neutral mesons, B_u and B_c charged mesons and Λ_b barions.

- the typical transverse momentum of hadrons is higher in the production of B-hadrons than in light hadrons. The difference in momentum distribution can be exploited to increase the signal-to-noise ratio in the identification of their decay products.

- finally, analogously to e^+e^- colliders, $p\overline{p}$ initial states are symmetric CP states, where it is expected to obtain equal rates of B and $\bar{B}$ hadrons.

1.2.1 Parton model and parton distribution functions

In a static picture, a proton is a bound state of three quarks $|uud\rangle$, with a characteristic radius of about 1 fm. However, in hadronic collisions at Tevatron energy, a proton must be described as a beam of free partons: three constituent quarks (valence quarks), quark-antiquark pairs (sea quarks) and virtual gluons. The different partons don't necessarily divide up the proton energy equally. The distribution of partons within the proton is described by the so-called parton distribution functions (PDF) $F_i^a(x, Q^2)$, which represent, for every partonic species i, gluon or quark, the probability density to carry the fraction x of proton momentum when probed at a momentum transfer Q^2. PDF functions, measured at particular values of Q^2 in specific processes, mostly deep-inelastic scattering processes, can be evaluated as continuous function of Q^2, using the suitable evolution equations as DGLAP [1] developed among the Quantum Chromo Dynamics (QCD).

1.2.2 $b\bar{b}$ production

In the QCD picture, the heavy flavour production in proton-antiproton interactions (in particular of b-quarks) can be described at lowest order by the processes of annihilation quark-antiquark $q + \bar{q} \rightarrow Q\bar{Q}$, as shown in figure 1.1(a) and by processes $2 \rightarrow 2$ of gluon-gluon fusion $g + g \rightarrow Q\bar{Q}$, as shown in figure 1.1(b).

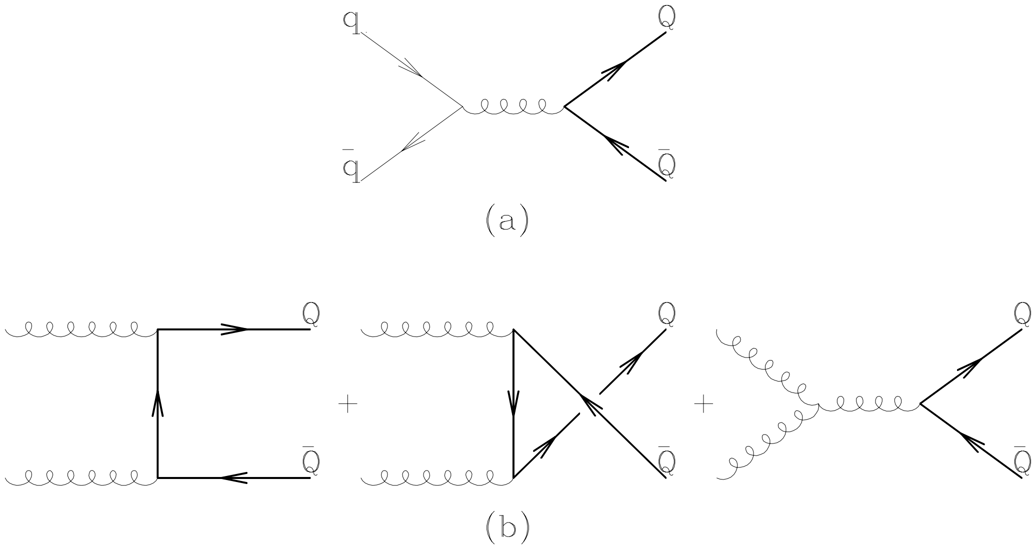

Figure 1.1: *Feynman graphs of HF production at Leading Order.*

In particular, at the energy of Tevatron $\sqrt{s} = 2\text{TeV}$ the dominant process is the gluon fusion. At order $O(\alpha_s^2)$ these processes show some peculiar characteristics, in particular:

- cross section $\hat{\sigma}$ at parton level is proportional to α_s^2/m_Q^2.
- Average transverse momentum P_T of heavy quarks grows approximately with their mass $\langle P_T(Q)\rangle \sim m_Q$, meaning that the average b quark transverse momentum is about $4 - 5$ GeV/c. In addition, the P_T distribution falls rapidly to zero as P_T becomes larger than the heavy quark mass.
- The heavy quark and antiquark are produced back-to-back in the parton-parton center-of-mass rest frame and are correspondingly back-to-back in the plane transverse to the colliding hadron beams.
- In addition, the rapidity distribution of the $Q\bar{Q}$ pair has a typical bell shape becoming wider and flatter as the partonic energy grows. This means that the heavy quark production is larger in the central region and falling at higher rapidities.

The higher order terms in the α_s expansion were originally considered 'corrections' to the leading order (LO) terms. It was instead noticed that the contributions of the next-to-leading order (NLO) processes, as $g + g \rightarrow g + Q + \bar{Q}$, can be important as the fundamental order terms.

Examples of order α_s^3 diagrams are displayed in figure 1.2. These precesses include real emission matrix elements and the interference of virtual matrix elements with the leading order diagrams. Other NLO contributions come from gluon splitting case, where Q and $\bar{Q}$ are produced close in phase space, and from processes of "flavour excitation", where a quark b is extracted from the sea quark of the proton or antiproton.

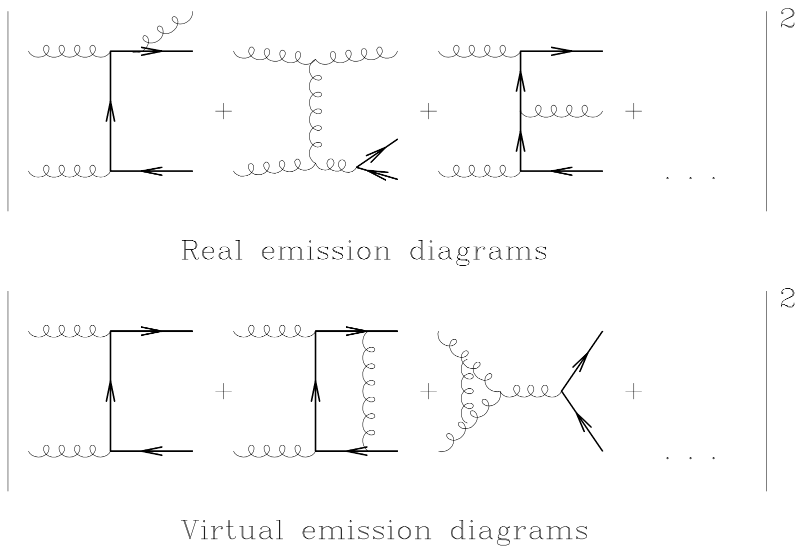

Figure 1.2: *Production diagrams of heavy quarks at Next to Leading Order.*

In summary, next-to-leading order processes are an important contribution to the calculation of the production cross section of b quarks in $\mathrm{p\overline{p}}$ collisions and modify the well defined topologies of the LO, making more difficult the event identification.

1.2.3 Hadronization of b quarks

Once b quarks are produced through the initial hard scattering, the process of forming B hadrons follows and is called hadronization or fragmentation. It is a low Q^2 process, for this reason it is beyond the reach of perturbative QCD calculations. The hadronization process is therefore described by semi-empirical models inspired by theory. Very common are the Feynman and Field [4] or the string fragmentation models. In a naive picture of the last one, we can imagine a "cloud" of gluons acting as a string between the b and the $\bar{b}$ quark pair, whose interacting potential increase linearly with the relative distance. As the quark and antiquark separate, the string stretches until it breaks and a new $q\bar{q}$ pair is created out of the vacuum. The process continues until there is no longer sufficient energy available to generate new $q\bar{q}$ pairs. The quarks are bound in non colored states, forming the particles observed in the detector. The fraction z of the initial b quark momentum transferred to the B hadron is commonly described by a fragmentation function, suggested, for example, by Peterson et al.[6] for the case of heavy quark forming a hadron together with a light quark u, d or s:

$$\frac{dN}{dz} = \frac{1}{z}\,(1 - \frac{1}{z} - \frac{\epsilon_b}{1-z})^{-2} \tag{1.1}$$

Here ϵ_b is the Peterson fragmentation parameter, related to the ratio of the effective light and heavy quark masses $\epsilon_b \approx (m_{\bar{q}}/m_Q)^2$ and its value is strictly connected to the momentum distribution of the heavy particles produced.

The comparison between the b quark and B meson production cross section has been faced for some time by CDF experiment. The behaviors of the total and differential cross section as a function of the transverse momentum has been studied and are shown respectively in figures 1.3 and 1.4. It is evident from the comparison between experimental data and theoretical predictions that consistent discrepancies still hold, even if this problem has been studied for many years either from the point of view of the analysis techniques or from the point of view of the theoretical models and their characteristic parameters. A recent analysis [7] ascribes the observed discrepancy to the non optimal use of the characteristic parameter of the fragmentation function which became one of the more important factor to estimate the production cross sections.

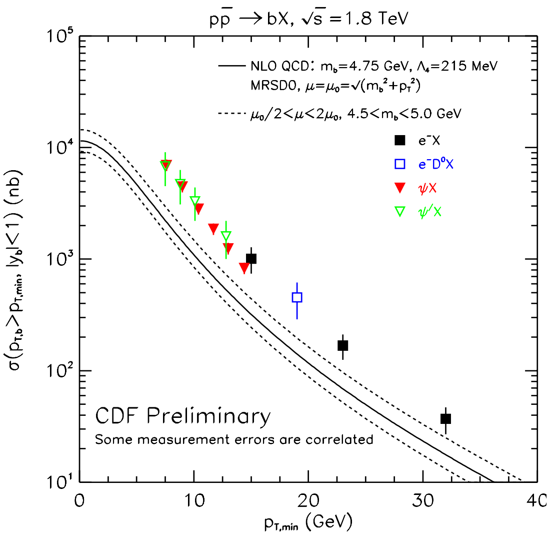

Figure 1.3: *Production cross section of b quark at CDF; it is expressed as a function of the minimum P_T of the b quark.*

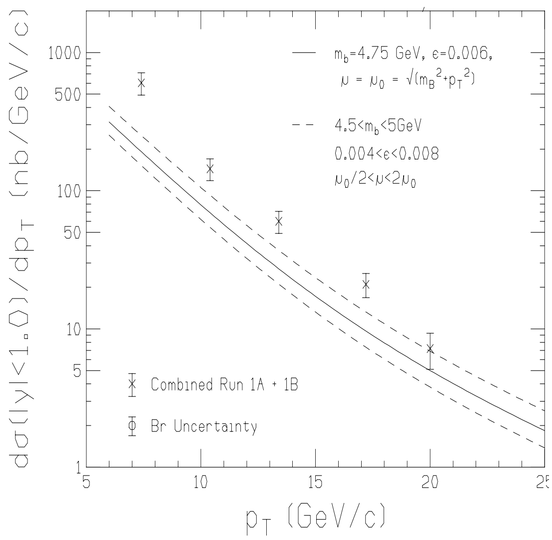

Figure 1.4: *Differential production cross section for B hadrons, from the study of the process $B^\pm \to J/\psi K^\pm$.*

1.2.4 f_s and f_u measurements

In fragmentation process the b quarks form different species of baryons or mesons. In this analysis it will be important to know the probability f_s for a b quark produced at Tevatron to associate to an antiquark $\bar{s}$ to form the B_s^0 meson. In particular we will be interested on the relative probability f_s/f_u respect to the formation of $B_u^\pm$ mesons.

LEP based experiment, with data collected at the energy of mass of Z^0, have obtained for f_s and the ratio the values [8] $f_s = 0.106 \pm 0.013$ and $f_d = f_u = 0.388 \pm 0.013$.

Also CDF has performed similar measurement [9] looking at several semileptonic and non-semileptonic decays, typical of the different species of hadrons, obtaining $f_u = f_d = 0.375 \pm 0.015$ and $f_s = 0.160 \pm 0.025$, results that stay around two standard deviations away from those found at LEP. Whether this difference hides a dependence on the kind of interaction, or on the characteristic Q^2 of the process, certainly different between LEP and Tevatron, has never been explained.

1.3 The CKM matrix

In the description of quarks and flavour, the Standard Model distinguishes between mass eigenstates and interaction eigenstates; the connection between the two basis is described by a suitable transformation matrix. In writing the weak charged interaction term, the "down" flavour eigenstates interact with the "up" eigenstates in combinations described by a unitary matrix V of dimension 3×3. An explicit parametrization of this mixing matrix in case of six flavours has been introduced in 1973 by Kobayashi and Maskawa [17], extending the description of the mixing between the d and s quarks, with only one parameter given by Cabibbo [16].

$$\begin{pmatrix} d' \\ s' \\ b' \end{pmatrix}_L = V_{CKM} \begin{pmatrix} d \\ s \\ b \end{pmatrix}_L ,$$

The unitary matrix V_{CKM} can be described by four independent parameters that can be identified with the three angle of rotation plus one complex phase which takes in account the violation of CP symmetry in weak interactions. The "standard" parametrization of this matrix [18], written below, refers explicitly to the three mixing angles

$$V_{CKM} = \begin{pmatrix} V_{ud} & V_{us} & V_{ub} \\ V_{cd} & V_{cs} & V_{cb} \\ V_{td} & V_{ts} & V_{tb} \end{pmatrix} = \begin{pmatrix} c_{12}c_{13} & s_{12}c_{13} & s_{13}e^{i\delta} \\ -s_{12}c_{23} - c_{12}s_{23}s_{13}e^{i\delta} & c_{12}c_{23} - s_{12}s_{23}s_{13}e^{i\delta} & s_{23}c_{13} \\ s_{12}s_{23} - c_{12}c_{23}s_{13}e^{i\delta} & -c_{12}s_{23} - s_{12}c_{23}s_{13}e^{i\delta} & c_{23}c_{13} \end{pmatrix}$$

where $c_{ij} = cos(\theta_{ij})$ and $s_{ij} = sen(\theta_{ij})$ with $i, j = 1, 2, 3$ indexes relative to the three generations. Also other parameterizations are possible, but among them this one presents some interesting features, in particular:

- s_{13} corresponds to $|V_{ub}|$, term of order 10^{-3}. This implies that $c_{13} \sim 1$ is a good approximation and that the terms V_{ud}, V_{us}, V_{cb} and V_{tb} can be determined by one parameter up to 10^{-4} order. This behavior greatly simplifies the parameter values extraction from the experimental data and the comparison with the expectations.
- s_{23} is directly connected to the transition $b \to c$
- CP violation, introduced with the phase δ, is suppressed of a factor s_{13}.

In order to describe this characteristic in a more quantitative manner it is useful to introduce the Wolfenstein parametrization [19] of the CKM matrix. After defining $\lambda = s_{12}$, $A\lambda^2 = s_{23}$, and $s_{13}e^{-i\delta} = A\lambda(\rho - \mathrm{i}\eta)$, the order of magnitude of these terms is determined by $\lambda \sim 0.22$. In a power expansion on the parameter λ, up to the third order, the matrix takes the form:

$$V_{CKM} = \begin{pmatrix} 1 - \lambda^2/2 & \lambda & A\lambda^3(\rho - i\eta) \\ -\lambda & 1 - \lambda^2/2 & A\lambda^2 \\ A\lambda^3(1 - \rho - i\eta) & -A\lambda^2 & 1 \end{pmatrix} + O(\lambda^4) \tag{1.2}$$

The unitarity of the matrix expressed in this way is verified up to the order $O(\lambda^3)$. The most interesting correction is $\Im V_{ts} = -A\lambda^4\eta$. It is useful to define also the parameters

$$\bar{\rho} = \rho(1 - \lambda^2/2) \ , \ \bar{\eta} = \eta(1 - \lambda^2/2) \tag{1.3}$$

so that $\bar{\rho} + i\bar{\eta} = -\frac{V_{ud}V_{ub}^*}{V_{cd}V_{cb}^*}$. The unitarity of the matrix allows a geometrical interpretation that will be described in the following paragraph.

1.3.1 Unitarity triangles

The unitarity of the matrix V_{CKM} allows to write 6 independent equations which constrain the parameter values:

$$\sum_k V_{ki} V^*_{kj} = \delta_{ij} \tag{1.4}$$

These equations, for $i \neq j$ become for instance:

$$\begin{array}{llccc} (a) & ds & V_{ud}V^*_{us} + & V_{cd}V^*_{cs} + & V_{td}V^*_{ts} = 0 \\ & & \lambda & \lambda & \lambda^5 \end{array} \tag{1.5}$$

$$\begin{array}{llccc} (b) & sb & V_{us}V^*_{ub} + & V_{cs}V^*_{cb} + & V_{ts}V^*_{tb} = 0 \\ & & \lambda^4 & \lambda^2 & \lambda^2 \end{array} \tag{1.6}$$

$$\begin{array}{llccc} (c) & db & V_{ud}V^*_{ub} + & V_{cd}V^*_{cb} + & V_{td}V^*_{tb} = 0 \\ & & \lambda^3 & \lambda^3 & \lambda^3 \end{array} \tag{1.7}$$

The order of magnitude of each term in the λ power series is reported below each equation. Only for the equation 1.7 the three angles are of the same order in λ, as can be seen in figure 1.5. In all other cases one of the angles will be really smaller than other two. In the case of the equation 1.7, dividing all the terms by $V_{cd}V^*_{cb}$ and representing the three contribution in a complex plane, the triangle is completely determined by the quantities $\bar{\rho}$ and $\bar{\eta}$, as can be seen in figure 1.6.

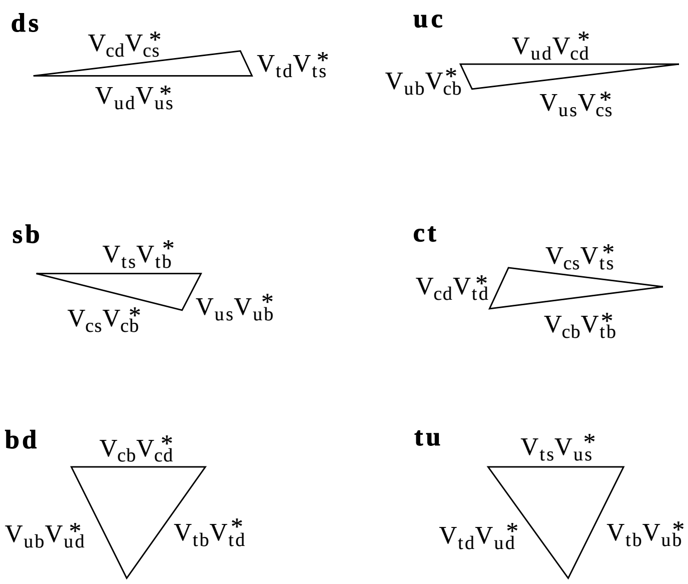

Figure 1.5: *Unitarity triangles.*

The triangle angles, usually named α, β and γ are related to the matrix parameter by the following equations:

$$\alpha \equiv \arg\left[-\frac{V_{td}V_{tb}^\star}{V_{ud}V_{ub}^\star}\right]$$

$$\beta \equiv \arg\left[-\frac{V_{cd}V_{cb}^\star}{V_{td}V_{tb}^\star}\right]$$

$$\gamma \equiv \arg\left[-\frac{V_{ud}V_{ub}^\star}{V_{cd}V_{cb}^\star}\right]$$

From these relations it is evident that a measurement of these angles giving results different from 0° or 180° implies a non zero value of the phase of the matrix V_{CKM} and indicates the violation of the CP symmetry.

Characteristic angles of unitarity triangles can be defined also from the equations 1.6 and 1.5; in particular can be considered the χ angle of the **sb** triangle and the χ' relative to the triangle **ds** defined as

$$\chi \equiv \arg\left[-\frac{V_{cb}V_{cs}^\star}{V_{tb}V_{ts}^\star}\right] = \lambda^2\eta + O(\lambda^4), \qquad \chi' \equiv \arg\left[-\frac{V_{us}V_{ud}^\star}{V_{cs}V_{cd}^\star}\right] = O(\lambda^4) \tag{1.8}$$

respectively of order $O(\lambda^2)$ and $O(\lambda^4)$. It is interesting to notice that another parametrization [20] of the V_{CKM} matrix make use only of the angles β and γ of the **db** triangle and χ and χ' relative to the triangle **sb** and **ds** respectively.

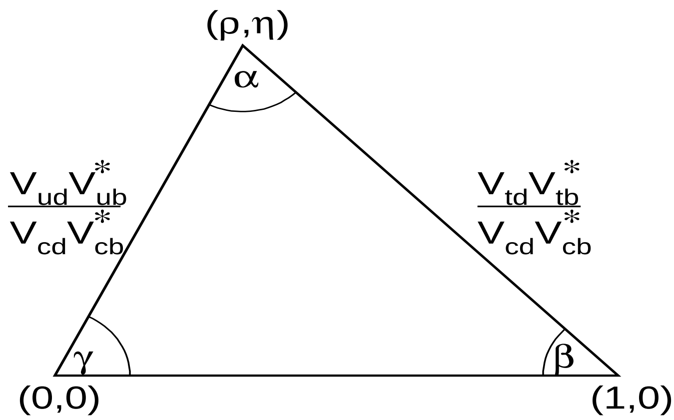

Figure 1.6: *Normalized* ***db*** *unitarity triangle.*

1.3.2 Experimental constraints on CKM elements

The amplitudes of elements $|V_{u_i d_j}|$ of the V_{CKM} matrix, where $u_i = u, c, t$ and $d_j = d, s, b$, are measured mainly on semi-leptonic disintegrations ($d_j \to u_i e^- \bar{\nu}_e$). In the case of contribution of just one diagram at tree level, the effective cross section will depend on only one of the parameters of the matrix. However the theoretical predictions are subject to uncertainty due to the non-perturbative nature of the process of hadronization and interaction in the final states.

We resume here the present knowledge on the matrix elements and the experimental sources:

- $|V_{ud}|$ - In nuclear β decays the transitions at partonic level are $d \to ue^-\bar{\nu}_e$. From the comparison between the decays described by vector currents and the μ decay, considering the radiative corrections to the matrix element, can be extracted the value:
$$|V_{ud}| = 0.97400 \pm 0.00014 \pm 0.00048 \tag{1.9}$$
The value of $|V_{ud}|$ can be extracted also from the measurement of the neutron mean life; in this case the theoretical uncertainty is lower, but the precision on measurement of the ratio g_V/g_A significantly affects the result:
$$|V_{ud}| = 0.9725 \pm 0.0013 \tag{1.10}$$

- $|V_{us}|$ - The analysis of the semileptonic disintegrations of the hyperons and of the kaons allows to extract the value of this parameter. For instance the K_{e3} decays provide a value of:
$$|V_{us}| = 0.2196 \pm 0.0026 \tag{1.11}$$

- $|V_{ub}|$ - This parameter can be estimated from the study of the inclusive decays $b \to ul^-\bar{\nu}_l$, for example characterizing the energy spectrum of the lepton, over the limit of the channels $b \to cl^-\bar{\nu}_l$; another determination comes from the study of exclusive processes, i.e. $B \to \pi l\nu$ or $B \to \rho l\nu$, where however the description of the weak current matrix element introduces relevant uncertainties. From measurements of the experiments at LEP and CLEO this parameter is estimated to be [12]:
$$|V_{ub}| = (3.6 \pm 0.7) \times 10^{-3}$$

- $|V_{cb}|$ - As for $|V_{ub}|$, the amplitude $|V_{cb}|$ can be measured both by exclusive methods, i.e. $B^0 \to D^{*-}l^+\nu_l$ or inclusive methods, i.e. $B \to X_c l\bar{\nu}_l$. The current estimate is:
$$|V_{cb}| = (41.0 \pm 1.6) \times 10^{-3} \tag{1.12}$$

- $|V_{cd}|$ - The processes that allow to measure this amplitude are mostly related to the “charm” production in neutrino and antineutrino high energy interactions with valence quarks, in experiment as CDHS at CERN. The measurement of the μ pairs production cross section in these weak interactions allows, once known the fraction of semileptonic decays of “charm” states, to extract the current estimate:
$$|V_{cd}| = 0.224 \pm 0.014 \tag{1.13}$$

- $|V_{cs}|$ - The measurements of this parameter can be obtained from the study of the semileptonic decay of charmed particles produced in neutrino interactions. As for $|V_{cd}|$, these measurement are affected by consistent theoretical uncertainties, of the order of 10%. A new approach consists in the identification of charm flavour in the decays of the W vector boson. This technique, used at LEP experiments, led to:

$$|V_{cs}| = 0.97 \pm 0.09 \pm 0.07 \tag{1.14}$$

Using the constraint of unitarity of the V_{CKM} matrix, which means $\sum_{i,j} |V_{ij}|^2 = 2$, ($i = u, c$ and $j = d, s, b$), it is possible to obtain a tighter bond. The ratio of hadronic W decays to leptonic decays has been measured at LEP, giving the result that $\sum_{i,j} |V_{ij}|^2 = 2.032 \pm 0.025$. Since five of the elements are well measured or contribute negligibly to the sum, can be extracted the value:

$$|V_{cs}| = 0.996 \pm 0.013 \tag{1.15}$$

- $|V_{tb}|$ - The identification of top production events in the experiments at Tevatron has considered also semileptonic decays $t \to b, s, dl^+\nu_l$. From an estimation of the fraction of decays $t \to bl^+\nu_l$ with respect to all the semileptonic decays, CDF experiment published the first direct estimate obtaining:

$$|V_{tb}| = 0.99 \pm 0.15 \tag{1.16}$$

1.4 Mixing of neutral B mesons

In the system composed of a pair of neutral self-conjugate B mesons different neutral states can be identified:

- two flavour eigenstates, which have defined quark content and are most useful to understand particle production and particle decay processes
- eigenstates of the Hamiltonian, states of definite mass and lifetime, which propagate through space in a definite fashion.

If CP were a good symmetry, the mass eigenstates would also be CP eigenstates, namely under a CP transformation they would transform into themselves with a definite eigenvalue ± 1. But since CP is not a good symmetry, the mass eigenstates can be different from CP eigenstates. In any case the mass eigenstates are not flavour eigenstates, and so the flavour eigenstates are mixed with one another as they propagate through space. The flavour eigenstates for B_d are $B^0 = \bar{b}d$ and $\bar{B}^0 = \bar{d}b$, for B_s are $B^0 = \bar{b}s$ and $\bar{B}^0 = \bar{s}b$.

The following description regards both the meson species.

An arbitrary linear combination of the neutral B-meson flavour eigenstates,

$$|\psi(t)\rangle = a(t)|B^0\rangle + b(t)|\bar{B}^0\rangle \tag{1.17}$$

is governed by a time-dependent Schrödinger equation

$$i\frac{d}{dt}|\psi(t)\rangle = H^{eff}|\psi(t)\rangle \equiv (M - \frac{i}{2}\Gamma)|\psi(t)\rangle \tag{1.18}$$

where M and Γ are both 2×2 Hermitian matrices, while the effective Hamiltonian H_{eff} is not, in order to account for decays. In details:

$$M = \begin{pmatrix} M_{11} & M_{12} \\ M_{12}^* & M_{22} \end{pmatrix} \qquad \Gamma = \begin{pmatrix} \Gamma_{11} & \Gamma_{12} \\ \Gamma_{12}^* & \Gamma_{22} \end{pmatrix} \tag{1.19}$$

CTP invariance guarantees $H_{11} = M_{11} - \frac{i}{2}\Gamma_{11} = H_{22} = M_{22} - \frac{i}{2}\Gamma_{22}$.
The off-diagonal terms in these matrices, M_{12} and Γ_{12}, are particularly important in the discussion of CP violation. They are the dispersive and absorptive parts respectively of the transition amplitude from B^0 to $\bar{B}^0$. In the standard model these contribution arise from the box diagrams with two W exchanges. The large mass of the B makes the QCD calculation of these quantities much more reliable than the corresponding calculation for K mixing.

The light B_L and heavy B_H mass eigenstates are given by:

$$|B_L\rangle = p|B^0\rangle + q|\bar{B}^0\rangle, \tag{1.20}$$
$$|B_H\rangle = p|B^0\rangle - q|\bar{B}^0\rangle. \tag{1.21}$$

The complex coefficients p and q obey the normalization condition $|q|^2 + |p|^2 = 1$.

The mass difference Δm_B and width difference $\Delta\Gamma_B$ between the neutral B mesons are defined as follows:

$$\Delta m_B \equiv M_H - M_L, \qquad \Delta\Gamma_B \equiv \Gamma_H - \Gamma_L, \tag{1.22}$$

Finding the eigenvalues of (1.18), one gets

$$(\Delta m_B)^2 - \frac{1}{4}(\Delta\Gamma_B)^2 = 4(|M_{12}|^2 - \frac{1}{4}|\Gamma_{12}|^2), \tag{1.23}$$
$$\Delta m_B \Delta\Gamma_B = 4\Re(M_{12}\Gamma^*_{12}). \tag{1.24}$$

While the ratio q/p is given by

$$\frac{q}{p} = -\frac{\Delta m_B - \frac{i}{2}\Delta\Gamma_B}{2(M_{12} - \frac{i}{2}\Gamma_{12})} = -\frac{2(M^*_{12} - \frac{i}{2}\Gamma^*_{12})}{\Delta m_B - \frac{i}{2}\Delta\Gamma_B} \tag{1.25}$$

Within the CKM model, the dispersive M_{12} and absorptive Γ_{12} mass matrix elements satisfy:

$$|M_{12}| \gg |\Gamma_{12}| \tag{1.26}$$

This relation is empirically valid for both the meson B^0 systems. Primarily $|\Gamma_{12}| \leq \Gamma$ because the Γ_{12} term comes from the decays to common final states for B^0 and $\bar{B}^0$. Besides, the experimental measurements suggest that $\Gamma_s \ll \Delta m_s$, this implies $\Gamma^s_{12} \ll \Delta m_s$ and, from equations 1.24

$$\Delta m_s \approx 2|M_{12}|, \ |\Delta\Gamma_s| \leq 2|\Gamma^s_{12}. \tag{1.27}$$

In the case of the B^0_d meson the experiment gives $\Delta m_d \approx 0.75\Gamma_d$ and the Standard Model expectation is $|\Gamma^d_{12}|/\Gamma_d \approx O(1\%)$ since the common decay channels are all suppressed by the V_{CKM} terms. In this case the ratio q/p can be expressed as

$$\frac{q}{p} = -\frac{M^*_{12}}{|M_{12}|} \tag{1.28}$$

1.4.1 Phase conventions

The states B^0 and $\bar{B}^0$ are related through CP transformation:

$$CP|B^0\rangle = e^{2i\xi_B}|\bar{B}^0\rangle, \quad CP|\bar{B}^0\rangle = e^{-2i\xi_B}|B^0\rangle. \tag{1.29}$$

The phase ξ_B is arbitrary. A phase transformation,

$$|B^0_\zeta\rangle = e^{-i\zeta}|B^0\rangle, \quad |\bar{B}^0_\zeta\rangle = e^{i\zeta}|\bar{B}^0\rangle, \tag{1.30}$$

has therefore no physical effects. In the new basis, CP transformations take the form

$$(CP)_\zeta|B^0_\zeta\rangle = e^{2i(\xi_B-\zeta)}|\bar{B}^0_\zeta\rangle, \quad (CP)_\zeta|\bar{B}^0_\zeta\rangle = e^{-2i(\xi_B-\zeta)}|B^0_\zeta\rangle \tag{1.31}$$

The various quantities discussed in this chapter change can be rewritten as:

$$M^\zeta_{12} = e^{2i\zeta}M_{12}, \quad \Gamma^\zeta_{12} = e^{2i\zeta}\Gamma_{12}, \quad (q/p)_\zeta = e^{-2i\zeta}(q/p). \tag{1.32}$$

the decay amplitudes defined by

$$A_f = \langle f|H|B^0\rangle, \quad \bar{A}_f = \langle f|H|\bar{B}^0\rangle \tag{1.33}$$

are also affected by the phase transformation (1.30):

$$(A_f)_\zeta = e^{-i\zeta}A_f, \quad (\bar{A}_f)_\zeta = e^{i\zeta}\bar{A}_f. \tag{1.34}$$

Similar phase freedom exists in redefining the mass eigenstates $|B_L\rangle$ and $|B_H\rangle$ and in defining the CP transformation law for a possible final state $|f\rangle$ and its CP conjugate $|f\rangle = e^{2i\xi_f}\bar{f}$. While both (q/p) and A_f acquire overall phase redefinitions when phase rotations are made, the quantity

$$\lambda_f = \frac{q}{p}\frac{\bar{A}_f}{A_f} \tag{1.35}$$

has a convention independent phase that has physical significance.

1.4.2 Time dependences

Supposing that a B^0 ($\bar{B}^0$) is created at a time $t = 0$, and denoting by $B^0(t)$ ($\bar{B}^0(t)$) the state that it evolves into after a time t, measured in its rest frame, to find out the time evolution we can use the expressions (1.20) and their evolution operators:

$$|B_i(t)\rangle = e^{-im_H t - \frac{\Gamma_H}{2}t|B_i\rangle}, \quad i = H, L \tag{1.36}$$

$$|B^0(t)\rangle = g_+(t)|B^0\rangle - \frac{q}{p}g_-(t)|\bar{B}^0\rangle \tag{1.37}$$

$$|\bar{B}^0(t)\rangle = -\frac{p}{q}g_-(t)|B^0\rangle + g_+(t)||\bar{B}^0\rangle \tag{1.38}$$

where

$$g_\pm(t) \equiv \frac{1}{2}\left(e^{-iM_H t - \frac{\Gamma_H}{2}t} \pm e^{-iM_L t - \frac{\Gamma_L}{2}t}\right). \tag{1.39}$$

The probability that at time t an initial state B^0 has turned to a $\bar{B}^0$ will be

$$|\langle\bar{B}^0|B^0(t)\rangle|^2 = |g_+(t)|^2 = \frac{1}{4}(e^{-\Gamma_L} + e^{-\Gamma_H} + 2e^{-\frac{\Gamma_L+\Gamma_H}{2}t}cos(\Delta Mt)) \tag{1.40}$$

the function shows a modulation with a characteristic period equal to $T = \frac{2\pi}{\Delta M}$. The following paragraph will be devoted to the description of the meaning and the measure of ΔM parameter. If the initial flavour of the neutral B meson has been tagged, for instance by reconstructing the decay of the hadron produced in association with the meson and with opposite flavour, the study of the decay widths in a specific final state, in particular the difference on the widths, emphasizes the characteristic parameters of the oscillation phenomenon:

$$\Gamma[B^0(t) \to f] = |A_f|^2\{|g_+(t)|^2 + |\lambda_f|^2|g_-(t)|^2 - 2\Re\left[\lambda_f g_+^*(t)g_-(t)\right]\},$$
$$\Gamma[\bar{B}^0(t) \to f] = |A_f|^2\left|\frac{q}{p}\right|^2\{|g_-(t)|^2 + |\lambda_{\bar{f}}|^2|g_+(t)|^2 - 2\Re\left[\lambda_f g_+(t)g_-^*(t)\right]\}. \tag{1.41}$$

It will be shown afterwards that the quantity $1-|q/p|$ is related to CP symmetry violation phenomena in mixing. Assuming the effect to be small in order to consider $|q/p| \sim 1$, the asymmetry between the decay widths of B^0 and $\bar{B}^0$ becomes:

$$\frac{\Gamma[B^0(t) \to f] - \Gamma[\bar{B}^0(t) \to f]}{|A_f|^2e^{-\Gamma t}} = \left(1 - |\lambda_f|^2\right)cos(\Delta m_B t) + 2\Im\lambda_f sin(\Delta m_B t) \tag{1.42}$$

However flavour tagging is a heavy request in terms of efficiency and in purity of the selected dataset; moreover, for instance for the B_s meson, the ratio $\Delta m_B/\Gamma_B$, which corresponds to the ratio between mean life and oscillation period, can be too large to be experimentally resolved, these considerations suggest to take into account also untagged data samples and their decay rates:

$$\frac{\Gamma[B^0(t) \to f] + \Gamma[\bar{B}^0(t) \to f]}{|A_f|^2e^{-\Gamma t}} = \left(1 + |\lambda_f|^2\right)cosh\frac{\Delta\Gamma_B t}{2} - 2\Re\lambda_f sinh\frac{\Delta\Gamma_B t}{2}. \tag{1.43}$$

The time dependencies of the B^0 meson decays are governed by two scales, $1/\Delta m_B$ and $1/\Delta\Gamma_B$. Nevertheless the equation 1.43 shows that the rapid time-dependent oscillations due to $\Delta m_B t$ cancel and the only remaining time-dependences are that of the two exponential falloffs included in $\Delta\Gamma_B t$. In this way the study of datasets of untagged production flavour events allows the measurement of $\Delta\Gamma_B$, which is complementary to Δm_B measurement, as will be shown in the next paragraph.

1.4.3 Δm_B mass difference

The mass difference Δm_B (different between B_d and B_s) can be measured looking at the time evolution of specific decays $B^0 \to f$, in particular for the final states opened only to one of the two flavours, B^0 or $\bar{B}^0$, where $\lambda_f = 0$. One example is given by the semileptonic direct decays, where the charge of the lepton is related to the flavour of the meson.

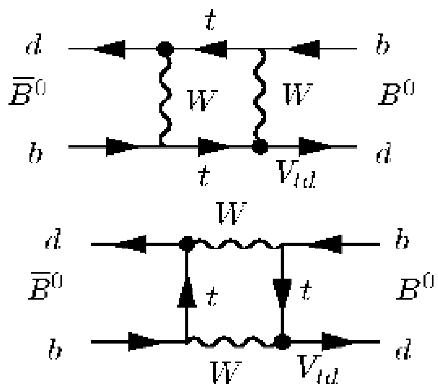

Figure 1.7: *Box diagrams represent the main contribution to the mixing phenomenon.*

In the Standard Model picture Δm_B is connected to the transition amplitude with $|\Delta B| = 2$, responsible of the mixing. The contribution at tree level is due to box diagrams 1.7 with a W vector bosons double exchange. In writing the effective Hamiltonian of the transition it is necessary to introduce contributes due to non perturbative effects. The result take the form of:

$$\Delta m_q = 2|M_{12}^q| = \frac{|H^{\Delta B=2}|}{m_{B_q}} = \frac{G_F^2}{6\pi^2}\eta_B m_{B_q}\hat{B}_{B_q} f_{B_q}^2 M_W^2 S(\frac{m_t^2}{M_W^2})|V_{tb}V_{tq}^*|^2 \tag{1.44}$$

where $q = s$ or d. In this expansion η_B represents the QCD contribution to higher orders, $S(\frac{m_t^2}{M_W^2})$ is a kinematic factor evaluated from box diagrams and the quantity $\hat{B}_{B_q} f_{B_q}^2$ provides the value of the matrix element. In this picture the last factor represents the main uncertainty source and reflects on the $|V_{tb}V_{tq}^*|$ estimate when evaluated from a Δm_B measurement.

Nevertheless the B^0 meson system presents an important aspect: there are two species of meson that can show flavour mixing effects. In this case the ratio between the two characteristic mixing parameters, Δm_d and Δm_s is related in a simpler way to the V_{CKM} matrix elements:

$$\frac{\Delta m_d}{\Delta m_s} = \frac{m_d}{m_s}\frac{\hat{B}_d f_d^2}{\hat{B}_s f_s^2}|V_{td}/V_{ts}|^2 \tag{1.45}$$

In this case the ratio of the quantities $\hat{B}_{B_q} f_{B_q}^2$ for the two species is affected by a lower uncertainty.

There are several Δm_d measurements obtained by experiments at LEP, or at beauty factories, by CDF and SLD. The current estimate [12] is $\Delta m_d = 0.489 \pm 0.05 \pm 0.07 ps^{-1}$ and corresponds to an oscillation period of ~ 8.3 mean lives ($x_d = \Delta m_d/\Gamma_B = 0.76$).

For the B_s^0 the experimental situation is different, no signal of oscillation has been observed. The current published results [12] estimate $\Delta m_s > 13.1 ps^{-1}$ ($x_s = \Delta m_d/\Gamma_B > 19$) at 95% of confidence level, which corresponds to about 0.3 mean lives. Other updated results have been recently presented and are reported here. It's interesting to notice that the ratio $\Delta\Gamma/\Delta m = |\Gamma_{12}/M_{12}|$ is the same in the two systems $B_d^0\bar{B}_d^0$ e $B_s^0\bar{B}_s^0$ and can be evaluated using lattice QCD calculations. As a matter of fact Δm_q can be estimated from the dispersive contribution in box diagrams, but also $\Delta\Gamma$ can be expressed in an analogous shape:

$$\Delta\Gamma_q = 2|\Gamma_{12}| = \frac{|H^{\Delta B=2}|}{m_{B_q}} = \frac{G_F^2}{4\pi}\eta_B' m_b^2 m_{B_q}\hat{B}_{B_q} f_{B_q}^2 |V_{tb}V_{tq}^*|^2 \tag{1.46}$$

where the various terms have the same meaning in the Δm expression.

The ratio $\Delta\Gamma/\Delta m$ can be nevertheless rewritten as

$$\frac{\Delta\Gamma_q}{\Delta m_q} = |\frac{\Gamma_{12}}{M_{12}}| = \frac{3\pi}{2}\frac{m_b^2}{m_W^2}\frac{1}{S(\frac{m_t^2}{M_W^2})} \approx O(\frac{m_b^2}{m_t^2}) \tag{1.47}$$

independent on the parameters of the V_{CKM} matrix. This quantity has been estimated to be $\sim 5\times10^{-3}$ with uncertainties around 30%, independent on the meson species. The lower limit on Δm_s, presented above, can be translated on a constraint on the difference of mean life $\Delta\Gamma_s/\Gamma_s > 10\%$. It is then important to measure $\Delta\Gamma_s$ in case of high Δm_s values.

1.5 CP violation in neutral B sector

The possible manifestations of CP symmetry violation can be classified in a model-independent way:

- CP violation in decay (which occurs in both charged and neutral decays), when the amplitude for decay and its CP conjugate process have different magnitudes;

$$|\frac{\bar{A}_{\bar{f}}}{A_f}| \neq 1 \tag{1.48}$$

- CP violation in mixing, which occurs when the two neutral mass eigenstates cannot be chosen to be CP eigenstates;

$$|\frac{q}{p}| \neq 1 \tag{1.49}$$

- CP violation in the interference between decays with and without mixing, which occurs in decays into final states that are common to B^0 and $\bar{B}^0$.

$$|\lambda_f| = |\frac{q}{p}\frac{\bar{A}_f}{A_f}| = 1, \quad \Im\lambda_f \neq 0 \tag{1.50}$$

1.5.1 CP violation in decay

For any final state f, the quantity $|\bar{A}_{\bar{f}}/A_f|$ is independent of phase conventions discussed on 1.4.1 and physically meaningful. There are two types of phases that may appear in A_f and $\bar{A}_{\bar{f}}$. Complex parameters that contributes to the amplitude will appear in complex conjugate form in the CP conjugate amplitude. Two are the kind of phases appearing in A_f and $\bar{A}_{\bar{f}}$: weak phases that contribute to the amplitude with opposite signs, that come from the V_{CKM} matrix and that are so related to the electroweak side of the processes; and the strong phases which contribute with terms of the same sign to A_f and $\bar{A}_{\bar{f}}$ and are connected to strong rescattering phenomena. Thus it is useful to write each contribution to A in three parts: its magnitude A_i, its weak-phase term $e^{i\phi_i}$, and its strong phase term $e^{i\delta_i}$. Then if several amplitudes contribute to $B^0 \to f$, the amplitude A_f and the CP conjugate amplitude $\bar{A}_{\bar{f}}$ are given by:

$$A_f = \sum_i A_i e^{i(\delta_i+\phi_i)}, \quad \bar{A}_{\bar{f}} = e^{2i(\xi_f-\xi_B)} \sum_i A_i e^{i(\delta_i-\phi_i)} \tag{1.51}$$

where ξ_f and ξ_B are defined in (1.4.1). (If f is a CP eigenstate then $e^{2i\xi_f} = \pm 1$ is its CP eigenvalue).
The convention independent quantity is then:

$$\left|\frac{\bar{A}_{\bar{f}}}{A_f}\right| = \left|\frac{\sum_i A_i e^{i(\delta_i-\phi_i)}}{\sum_i A_i e^{i(\delta_i+\phi_i)}}\right| \tag{1.52}$$

This relation shows that when the modulus of the ratio of the two amplitudes is not equal to one, this is due to the presence of weak phases and it is a signal of CP violation:

$$|\bar{A}_{\bar{f}}/A_f| \neq 1 \Longrightarrow CP\ violation \tag{1.53}$$

This type of CP violation will not occur unless at least two terms that have different weak phases acquire different strong phases. This can occur only if there are at least two terms with different weak phases and strong phases. In term of the decay amplitudes the CP asymmetry becomes:

$$a_f = \frac{1 - |\bar{A}_{\bar{f}}/A_f|^2}{1 + |\bar{A}_{\bar{f}}/A_f|^2} \tag{1.54}$$

1.5.2 CP violation in mixing

A second quantity that is independent of phase conventions and physically meaningful is

$$\left|\frac{q}{p}\right|^2 = \left|\frac{M_{12}^* - \frac{i}{2}\Gamma_{12}^*}{M_{12} - \frac{i}{2}\Gamma_{12}}\right| \tag{1.55}$$

When CP is conserved, the mass eigenstates must be CP eigenstates. In that case the relative phase between M_{12} and Γ_{12} vanishes. Therefore eq. (1.55) implies

$$|q/p| \neq 1 \Longrightarrow CP\ violation \tag{1.56}$$

This kind of CP violation is called CP violation in mixing; it is often referred to as indirect CP violation. It results from the mass eigenstates being different from the CP eigenstates. For the B^0 system, this effect could be observed through the asymmetries in semileptonic decays. In term of $|q/p|$:

$$a_{sl} = \frac{\Gamma(\bar{B}^0(t) \to l^+\nu X) - \Gamma(B^0(t) \to l^-\bar{\nu} X)}{\Gamma(\bar{B}^0(t) \to l^+\nu X) + \Gamma(B^0(t) \to l^-\bar{\nu} X)} = \frac{1 - |q/p|^4}{1 + |q/p|^4} \tag{1.57}$$

In order to calculate the deviation of $|q/p|$ from 1, $\Im(\Gamma_{12}/M_{12})$ has to be calculated; this involves large hadronic uncertainties, in particular in the hadronization model for Γ_{12}. Thus even if such asymmetries are observed, it will be difficult to relate their rates to V_{CKM} parameters.

1.5.3 CP violation in the interference between decays with and without mixing

Let's consider again neutral B decays into final CP eigenstates, f_{CP}. Such states are accessible in both B^0 and $\bar{B}^0$ decays. The quantity of interest here that is independent of phase conventions and physically meaningful is λ_f, described in 1.4.1. When CP is conserved we know that $|q/p| = 1$, $|\bar{A}_{\bar{f}_{CP}}/A_{f_{CP}}| = 1$, and furthermore the relative phase between (q/p) and $(\bar{A}_{\bar{f}_{CP}}/A_{f_{CP}})$ vanishes. We have yet analyzed the consequences of CP violation in decay ($|\bar{A}/A| \neq 1$) and in mixing ($|q/p| \neq 1$), however, it is possible that, to a good approximation, $|q/p| = 1$ and $|\bar{A}/A| = 1$, and still observe CP violation if:

$$|\lambda_f| = 1, \quad \Im\lambda \neq 0 \tag{1.58}$$

This type of CP violation is called CP violation in the interference between decays with and without mixing. We want now to point out the importance of the mechanism we have just described. The theoretical estimate of direct-CP-violating quantities is usually plagued by hadronic uncertainties which consist for instance in the difficulty to estimate the strong phases, and so to extract the weak phases.

In this case instead, for processes dominated by a single amplitude, the strong phase will cancel and the asymmetry can be written as:

$$a_{CP}(t) = \frac{\Gamma[B^0(t) \to f] - \Gamma[\bar{B}^0(t) \to f]}{\Gamma[B^0(t) \to f] + \Gamma[\bar{B}^0(t) \to f]} = \frac{\Im\lambda_f sin(\Delta m_B t)}{cosh(\Delta\Gamma_B t/2) - \Re\lambda_f sinh(\Delta\Gamma_B t/2)} \tag{1.59}$$

which, in case $\Delta\Gamma$ can be neglected, become:

$$a_{CP}(t) = \Im\lambda_f sin(\Delta m_B t) \tag{1.60}$$

directly connected to λ_f. A well known example of this kind of violation is given by the asymmetry in the decay $B_d^0 \to J/\psi K_s^0$ dominated by the process $b \to c\bar{c}s$ and by his CP conjugate. The measurement of $\lambda_{J/\psi K_s^0}$ is related to the parameters of V_{CKM} matrix and in particular to the β angle of the unitarity triangle presented in figure 1.8 as:

$$\lambda_{J/\psi K_s^0} = -\left(\frac{V_{tb}^* V_{td}}{V_{tb} V_{td}^*}\right)\left(\frac{V_{cb} V_{cs}^*}{V_{cb}^* V_{cs}}\right)\left(\frac{V_{cs} V_{cd}^*}{V_{cs}^* V_{cd}}\right) = e^{-2i\beta} \tag{1.61}$$

Figure 1.8 summarizes the current results on the parameter described and their link with the V_{CKM} matrix elements.

1.6 B_s sector

The identification of B_s states is quite recent. CDF experiment has observed this state for the first time in 1993 [14] and has measures the his mass. Afterwards also the experiment at LEP has faced the study of this state, obtaining in the following years the mean life measurement. Nevertheless, the $B_s\bar{B}_s$ mixing, despite the efforts of the experiments both at LEP and Tevatron, has not been observed; besides, the $\Delta\Gamma_s$ measurement has not been achieved up to now.

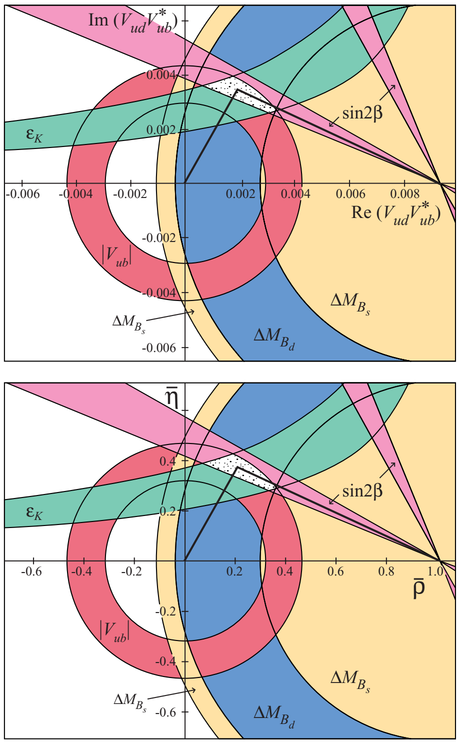

Figure 1.8: *Experimental results on the $\bar{\rho} - \bar{\eta}$ plane.*

In the previous paragraphs it has been mentioned that the comparison between the mixing measurements on this sector and the ones on the sector of the $B_d\bar{B}_d$ will represent a further step in the knowledge of the V_{CKM} matrix parameters. In the next few years only the experiments at Tevatron will be able to study this sector, since the e^+e^- machines work at the $\Upsilon(4S)$ energy and so they don't produce B_s states.

The mass and mean life measurements obtained by the LEP experiments and by CDF were based mostly on the study of semileptonic decay channels with D_s meson production and in particular of the rare decay to $J/\psi\phi$ where the low branching ratio $\mathcal{B}(B_s^0 \to J/\psi\phi) \approx 10^{-3}$ is compensated in CDF by a clear signature and good signal to noise ratio.

1.6.1 The $J/\psi\eta^{(\prime)}$ channel

The decay processes to $J/\psi\eta^{(\prime)}$ final states represent the analogous to the $J/\psi K^0$ decays in the B_d sector. The final state is a CP eigenstate with eigenvalue $\eta_{J/\psi\eta} = -1$, unlike the final states $B_s \to J/\psi\phi$ where, due to the presence of two vector mesons J/ψ and ϕ, both CP eigenstates are present. The subprocess at quark level $\bar{b} \to \bar{c}c\bar{s}$ is dominated by the diagram with a W emission. Contributions to more complex diagrams are of order $O(\lambda^2)$. The estimations of the decay ratio in these channels [4] are based in the comparison with the channel $B_d^0 \to J/\psi K_s^0$. The amplitudes of the two processes indeed differ only for the kinematic and for the non perturbative hadronic contributions; they don't depend from the V_{CKM} matrix elements that, at tree level, are the same. A further factor rises from the mixing angle θ_P of the pseudoscalar states η and η' in the SU(3) flavour classification, angle not yet well defined between an interval $-20° < \theta_P < -10°$. After these hypothesis, the decay ratio of $B_s \to J/\psi\eta$ can be expressed as:

$$\mathcal{B}(B_s^0 \to J/\psi\eta) = \mathcal{B}(B_d^0 \to J/\psi K^0)|S_\eta|^2(\frac{m_{B_d}^3}{m_{B_s}^3})(\frac{\lambda_{B_s}}{\lambda_{B_d}})^{3/2} \tag{1.62}$$

where the function λ includes the kinematic effects in the decays and where $S_\eta = sin(\theta_P)/\sqrt{3}$. Using the value 8.7×10^{-4} [12] for the decay ratio of $B_d \to J/\psi K^0$ we obtain a result varying between 8.3 and 9.5×10^{-4} when correspondingly varying the mixing angle θ_P.

The CP asymmetry in this case is dominated by the interference between decay with and without mixing and is given by:

$$\Im\lambda_{J/\psi\eta^{(\prime)}} = -sin(2\chi) \tag{1.63}$$

where the angle χ has been previously defined (1.8) and regards the unitarity triangle **sb**. If in a way this angle is expected to be of order $O(\lambda^2)$ and so really more difficult to measure with respect to the β angle relative to the **bd** triangle, on the other hand new physics phenomena beyond Standard Model can reveal themselves in unexpected behaviors of the asymmetry variables.

1.6.2 Experimental aspects of the $J/\psi\eta^{(\prime)}$ channel

The decay ratio of the B_s^0 mesons has never been observed; only an upper limit at 90% of confidence level has been set $\mathcal{B}(B_s^0 \to J/\psi\eta) < 3.8 \times 10^{-3}$, obtained by the L3 experiment at LEP. As will be shown later on in this work, the J/ψ is identified in the channel $J/\psi \to \mu\mu$, process well studied at CDF experiment and which present high identification efficiencies and an high signal to noise ratio yet at muon trigger level.

From an experimental point of view, between the different decay channels of the η and η', the three more interesting final states are $\eta \to \gamma\gamma$ (39%) , $\eta' \to \eta\pi^+\pi^-$ (44%) $\to \gamma\gamma\pi^+\pi^-$ and finally $\eta' \to \rho\gamma$ (31%) $\to \pi^+\pi^-\gamma$. It is evident from this list of final states that the more delicate point of this research is the identification of low (as regard CDF) energy photons, down to ~ 1 GeV. This work has the aim to begin an investigation on these processes, starting from the first of them, $\mathcal{B}(B_s^0 \to J/\psi\eta \to \mu^+\mu^-\gamma\gamma)$, and will be in future extended to the other channels and to the new data currently collecting at CDF.

It is important here to remind that BaBar experiment has studied the production of final states $\eta \to \gamma\gamma$, $\eta \to \pi^+\pi^-\pi^0$ and $\eta' \to \eta\pi^+\pi^-$ in association with the J/ψ obtaining for the B_d^0 the upper limits $\mathcal{B}(B_d^0 \to J/\psi\eta) < 2.7\times10^{-5}$ and $\mathcal{B}(B_d^0 \to J/\psi\eta') < 6.4\times10^{-5}$. In this case the same model used for the B_s^0 for the branching ratio estimates provides the values between 1.6 and 4.1×10^{-6}, since this process is suppressed by the V_{CKM} matrix element $|V_{cd}|^2 \approx \lambda^2$. We can then expect in this search the channel with B_d^0 mesons to be strongly suppressed with respect to the case of B_s^0.

Bibliography

[1] G. Altarelli, G. Parisi, "Asymptotic freedom in parton language", *Nucl. Phys. B* **126**, 298 (1977)

Y.N. Gribov, L.N. Lipatov, "Deep Inelastic $e-p$ Scattering in Perturbation Theory", *Yad. Fiz.* **15**, 781 (1972)

Y.L. Dokshitzer, "Calculation of structure functions of deep-inelastic scattering and e^+e^- annihilation by perturbation theory in quantum chromodynamics", *Sov. Phys. JETP* **46**, 641 (1977)

[2] G. Ridolfi, "An Introduction to the Standard Model of Electroweak Interactions", lecture notes.

[3] S.W. Herb, *et al.*, "Observation of Dimuon Resonance at 9.5 GeV in 400-GeV Proton-Nucleus Collisions", *Phys. Rev. Lett.* **39**, 252 (1977)
W.R. Innes, *et al.*, "Observation of Structure in the Υ Region", *Phys. Rev. Lett.* **39**, 1240 (1977)

[4] R.D. Field, R.P. Feynman, "Quark elastic scattering as a source of high-transverse-momentum mesons ", *Phys. Rev. D* **15**, 2590 (1977)

[5] B. Andersson, *et al. Zeit. Phys. C* **20**, 317 (1983).

[6] C. Peterson *et al.*, "Scaling violations in inclusive e^+e^- annihilation spectra", *Phys. Rev. D* **27**, 105 (1983)

[7] P. Nason *hep-ph/0207362*
Pres. at: 6th International Workshop on Heavy Quarks and Leptons, Vietri sul Mare, Salerno, Italy, 27 May - 1 Jun 2002

[8] ALEPH, CDF, DELPHI, L3, OPAL, SLD, "Combined results on b-hadron production rates and decay properties", CERN-EP/2001-050, (Jun 2001)

[9] T. Affolder *et al.*, "Measurement of b-Quark Fragmentation Fractions in $p\overline{p}$ Collisions at $\sqrt{s} = 1.8$ TeV", *Phys. Rev. Lett.* **84**, 1663 (2000)

[10] J.H. Christenson *et al.*, "Evidence for the 2π Decay of the K_2^0 Meson", *Phys. Rev. Lett.* **13**, 138 (1964)

[11] B. Auber *et al.*, "Observation of CP Violation in the B^0 Meson System", *Phys. Rev. Lett.* **87**, 091801 (2001)
K. Abe *et al.*, "Observation of Large CP Violation in the Neutral B Meson System", *Phys. Rev. Lett.* **87**, 091802 (2001)

[12] K. Hagiwara *et al.*, "Review of Particle Physics", *Phys. Rev. D* **66**, 010001 (2002)

[13] "31st International Conference on High Energy Physics, ICHEP02, Amsterdam (The Netherlands)", July 24-31, 2002

[14] F. Abe *et al.*, "Observation of the Decay $B_s^0 \to J/\psi\phi$ in p$\overline{\text{p}}$ collisions at $\sqrt{s} = 1.8$ TeV ", *Phys.Rev.Lett.* **71**, 1685 (1993)

[15] P. Z. Skands, "Branching ratios for $B_{d,s} \to J/\psi\eta$ and $B_{d,s} \to \eta\ell^+\ell^-$, extracting γ from $B_{d,s} \to J/\psi\eta$, and possibilities for constraining C_{10A} in semileptonic B decays", *J. High Energy Phys*, 01 (2001) 008

[16] N. Cabibbo, "Unitary Symmetry and Leptonic Decays", *Phys. Rev. Lett.* **10**, 531 (1963)

[17] M. Kobayashi, K. Maskawa, *Progr. Theor. Phys.* **49**, 652 (1973)

[18] L. Chau, W Keung, "Measurements of Spin-Correlation Parameter A_{NN} and Analyzing Power at 90° for $p_{pol}p_{pol} \to d/\pi^+$ ", *Phys. Rev. Lett.* **53**, 1802 (1984)
H. Harari, M. Leurer, "Recommending a standard choice of Cabibbo angles and KM phases for any number of generations", *Phys. Lett. B* **181**, 123 (1986)
F. Botella, L. Chao, "Anticipating the higher generations of quarks from rephasing invariance of the mixing matrix", *Phys. Lett. B* **168**, 97 (1986)

[19] L. Wolfenstein, "Final-state interactions and *CP* violation in weak decays", *Phys. Rev. D* **D43**, 151 (1991)

[20] R. Aleksan, B. Kayser, D. London, "Determining of the Quark Mixing from *CP*-violating Asymmetries", *Phys. Rev. Lett.* **73**, 18 (1994)

Chapter 2

The CDF detector

This chapter will be devoted to the description of the CDF detector, the experimental apparatus used to collect the data analyzed in this thesis. CDF is one of the two detectors installed on the main ring of Tevatron, the proton-antiproton collider of the Fermi National Accelerator Laboratory in Batavia, Illinois (USA).

A particular emphasis will be put on the tracking system, included the silicon vertex detector, on the μ detector chambers and on the electromagnetic calorimeter, whose performance is crucial in this analysis.

The data here analyzed were collected during the Run I, began in August 1992, ended on July 1995 and divided in two periods: Run Ia and Run Ib. During the interval between the two periods (May 1993-January 1994) both Tevatron and CDF underwent many major upgrades. The silicon vertex detector has been substituted, and also the muon coverage has been extended. The description of the detector here presented will concern the Run Ib configuration (whose integrated luminosity is ~ 5 times the Run Ia luminosity), and only the differences will be pointed out.

2.1 The Tevatron $\mathrm{p\overline{p}}$ Collider

The acceleration of protons and antiprotons to the final energies of 900 GeV is accomplished by the use of a sequence of six particle accelerators. A schematic diagram of the structure is presented in figure 2.1. The two main goals are to obtain high energy colliding beams and high interaction probability. The first requirement is related to the need of having the highest possible energy for studying the production processes of jets, heavy quarks as *bottom* and *top*, electroweak bosons and new physics. The second requirement is directly connected to the collected statistics; the number of event produced for a process with cross section σ in an interval Δt is:

$$N = \int_{\Delta t} \mathcal{L} dt \cdot \sigma \quad ,$$

where $\mathcal{L}$ is the instantaneous luminosity. This quantity depends on the particle density and on the revolution frequency of the p and $\bar{p}$ bunches by means of:

$$\mathcal{L} = \frac{N_p \cdot N_{\bar{p}} \cdot n \cdot f_0}{4\pi\Sigma} \quad , \tag{2.1}$$

where N_p ($N_{\bar{p}}$) is the number of protons (antiprotons) in a single bunch, n is the number of

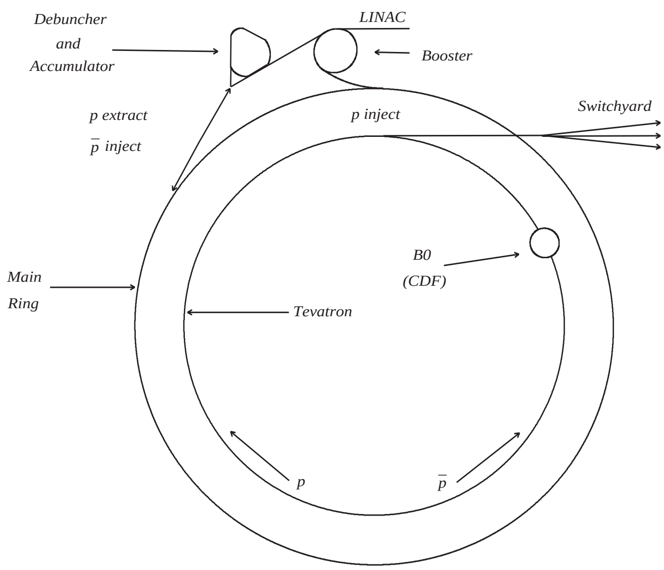

Figure 2.1: *Schematic representation of the accelerator; the highlighted devices are the ones used for the building the of particle beams.*

bunches circulating in the ring, f_0 the revolution frequency (for the Tevatron $f_0 \approx 50\ kHz$) and Σ is the transverse dimension of the beam.

2.1.1 Production of the proton buckets

The production sequence begins with the conversion of gaseous H_2 molecules to H^- ions, a Cockroft-Walton electrostatic accelerator then provides the ions an energy of 750 keV which subsequently enter a 150 m linear accelerator (Linac), where they are accelerated to energies of 400 MeV by a sequence of drift-tube induced oscillating electric fields. At the end of the Linac stage the H^- ions are guided into the Booster, an alternating gradient synchrotron with a radius of $\sim$ 75 m, in which they make $\sim$ 16000 revolutions and acquire an energy of 8 GeV and the typical bunch structure. Each bunch is composed by about 10^{10} protons. During the injection into the Booster, both electrons are stripped from the H^- ions passing through a carbon foil. The 8-GeV protons are injected from the Booster into the 1 Km radius Main Ring, a proton synchrotron with 1014 conventional magnets, where they are accelerated to typical energies of $\approx$ 150 GeV, ready to be injected into the Tevatron.

2.1.2 Production of the anti-proton buckets

Part of the protons circulating inside the Main Ring, reached the energy of 120 GeV, are extracted and are made to strike to a 7 cm thick nickel or copper target, producing, among the others, antiprotons. In this stage is important to collect the maximum number of antiproton with the minimum angular and momentum spread (i.e. minimum emittance[1]): this is essential to obtain bunches with small transverse section and then high luminosity in the collisions.

[1]The emittance ϵ of a beam particle is defined as the occupied volume in the phase space $\epsilon = \int dxdp$.

The transverse size of the beam Σ of the equation 2.1 strongly depends on the focusing magnets inside the ring and in particular on those placed closer to the interaction point, the so called low beta quadrupoles. In order to minimize the transverse size, the antiprotons are focused by means of a liquid lithium lens and then directed to the debuncher, which is a ring 520 m in circumference where the antiproton beam aperture and energy distribution are reduced by means of stochastic cooling and debunching techniques respectively. The antiprotons are then transferred to the accumulator ring, which is concentric with the debuncher, for storage and further cooling, up to a total number of antiprotons of 6×10^{11}.
The stochastic cooling is implemented with a set of sensors and deflectors, in general placed at a distance where the phase is changed by $\frac{\pi}{2}$ along the accumulation ring. The sensors measure the beam displacement with respect to the equilibrium position and send this information to the deflectors. The bending field influences not only the displaced particle, but also the orbit of the neighbors, introducing noise in the system: for this reason the process is very slow and several hours are needed in order to obtain an acceptable number of collimated particles. The antiprotons, whose momentum dispersion has been reduced from 3.5% to 0.2%, are then ready for the injection (6 bunches) into the Main Ring where they are boosted to 150 GeV and then inserted into the Tevatron where other 6 protons bunches are yet circulating in opposite direction.

2.1.3 $p\overline{p}$ interactions

Once injected into the Tevatron, the six proton and antiproton bunches are accelerated from 150 to 900 GeV. Then the bunches are made to collide at interaction regions such as $B0$ and $D0$ where the two experimental apparatus CDF and DØ are placed. The

Center of mass energy	$1.8\ TeV$
Circumference	$6.2831\ km$
Time per single revolution	$20.9586\ \mu s$
Number of magnets	1113
Frequency of RF	$53.105\ MHz$
Peak luminosity	$2.6 \times 10^{31}\ cm^{-2}s^{-1}$
Average luminosity	$8 \times 10^{30}\ cm^{-2}s^{-1}$
Bunch crossing interval	$3.5\ \mu s$
Number of p and $\bar{p}$ bunches	6
Average number of protons per bunch	10×10^{10}
Average number of antiprotons per bunch	5×10^{10}
Proton emittance, ϵ_p	$15\pi\ mm \cdot mr$
Antiproton emittance, $\epsilon_{\bar{p}}$	$18\pi\ mm \cdot mr$

Table 2.1: *Tevatron working parameters.*

Tevatron is a separated functions synchrotron where the bending of the particles orbit is provided by dipolar magnets, while the focusing is given by pairs of quadrupoles rotated by a 90° angle. This allows to place focusing magnets close to the interaction point and then increase the luminosity.
The duration of a store, the time with circulating colliding beams, is about 15-20 hours;

during this period the luminosity decreases quickly in the first 4-5 hours due to the beam-gas interactions, then it continues to decrease slowly down to a value of $0.7 - 0.8 \times 10^{30} cm^{-2} s^{-1}$, when the beam is dumped.
Table 2.1.3 resumes the typical Tevatron working parameters.

2.2 The CDF detector

The Collider Detector at Fermilab (CDF) is a general purpose 5000 tons detector designed to study the physics of $p\overline{p}$ collisions at a center of mass energy near 2 TeV.
The basic design goals of the CDF detector, pictured in figures 2.2 and 2.3, is to identify leptons and measures the momenta and energies of particles originating from the $B0$ interaction region. Since the phase space for high energy hadronic collision is typically described by rapidity, transverse momentum and azimuthal angle, it's natural that the CDF detector components have an approximately cylindrical symmetry and uniform segmentation in pseudorapidity and azimuthal angle[2]. Tracking detectors, which detect charged particles and measures their momenta, reside nearest the interaction region and inside a $\approx$ 1.4 T magnetic field. The field is generated by a large electromagnet of Nb-Ti/Cu superconductor that constitutes a solenoid 4.8 m in length, 1.5 m in radius, and 0.85 radiation lengths in radial thickness. The tracking systems surround an evacuated beryllium beam pipe that is 3.8 cm in diameter and has walls 0.5 mm thick. Section 2.3 describes the CDF tracking system in some detail.
The detector is divided into a central region ($|\eta| < 1.1$), two end plug regions ($1.1 < |\eta| < 2.4$), and two forward-backward regions ($2.4 < |\eta| < 4.2$). The tracking volume and solenoid are surrounded by sampling calorimeters that measure electromagnetic and hadronic energy flow from the collision point for particles with $|\eta| < 4.2$. The calorimeter systems are segmented into projective $\eta - \phi$ towers, each of which points back toward the nominal interaction region and has an electromagnetic shower counter in front of a corresponding hadronic calorimeter cell. Section 2.4 describes the calorimeter system in more detail.

2.3 The Tracking Systems

The reconstruction of exclusive B-meson decay relies heavily on the precise measurements of the daughter particle decay vertexes, momenta, and charges. The CDF detector's main tracking capabilities consist of four distinct but complementary tracking subsystems. These systems, listed in order of increasing distance from the interaction region, are the silicon vertex detector, the vertex time projection chamber, the central tracking chamber, and the central drift tube array.

[2]The CDF coordinate system is right handed with x pointing out of the Tevatron ring, y is vertical, and z in the proton beam direction. The polar beam angle, θ, is measured with respect to the proton direction; the pseudorapidity, η, is defined by $\eta = \ln(\tan\ (\theta\ /\ 2))$, with θ measured assuming a z-vertex position of zero; the azimuthal angle is represented by ϕ and defined with respect to the plane of the Tevatron; and the transverse displacement coordinate is denoted by r.

Figure 2.2: *CDF detector section: shown are the subsystems. The detector is symmetric with respect to* $\eta = 0$.

2.3.1 The SVX Detector

The silicon microstrip vertex detector (SVX) enables the identification in the $r-\phi$ plane of secondary vertexes displaced from the $\mathrm{p\overline{p}}$ collision point resulting from the weak decays of b quarks. Installed in the CDF detector in 1992, the SVX was the first detector of its kind to be operated successfully in a hadron collider environment. In 1993, a more radiation hard and low noise version of the SVX, the SVX', was commissioned for the 1994-1995 Tevatron collider run[3]. The SVX consists of two identical cylindrical modules, one of which is pictured in figure 2.4, each comprising four concentric cylindrical layers with radii of 2.9, 4.3, 5.7, and 7.9 cm. Since the luminous $\mathrm{p\overline{p}}$ interaction region is rather elongated in the z direction (with a Gaussian distribution having a standard deviation of $\sim$ 30 cm), approximately 40% of $\mathrm{p\overline{p}}$ collision vertices lie outside the acceptance of the SVX, which has an active length of 51.1 cm.

On both of the SVX barrels, the four layers are each segmented into twelve 'ladders' that subtend approximately 30° in azimuth and are oriented parallel to the beam axis. Figure 2.5 depicts a typical ladder situated in the third layer of the SVX. Three single-sided 8.5 cm long silicon microstrip detectors are electrically bonded together with aluminum wire along the z direction to form a 25.5 cm active silicon region on each ladder module. The detectors consist of an n-doped silicon wafer, 300 μm thick, with p^+ strips on one side;

[3] Unless noted otherwise, references to the SVX apply to the SVX' as well.

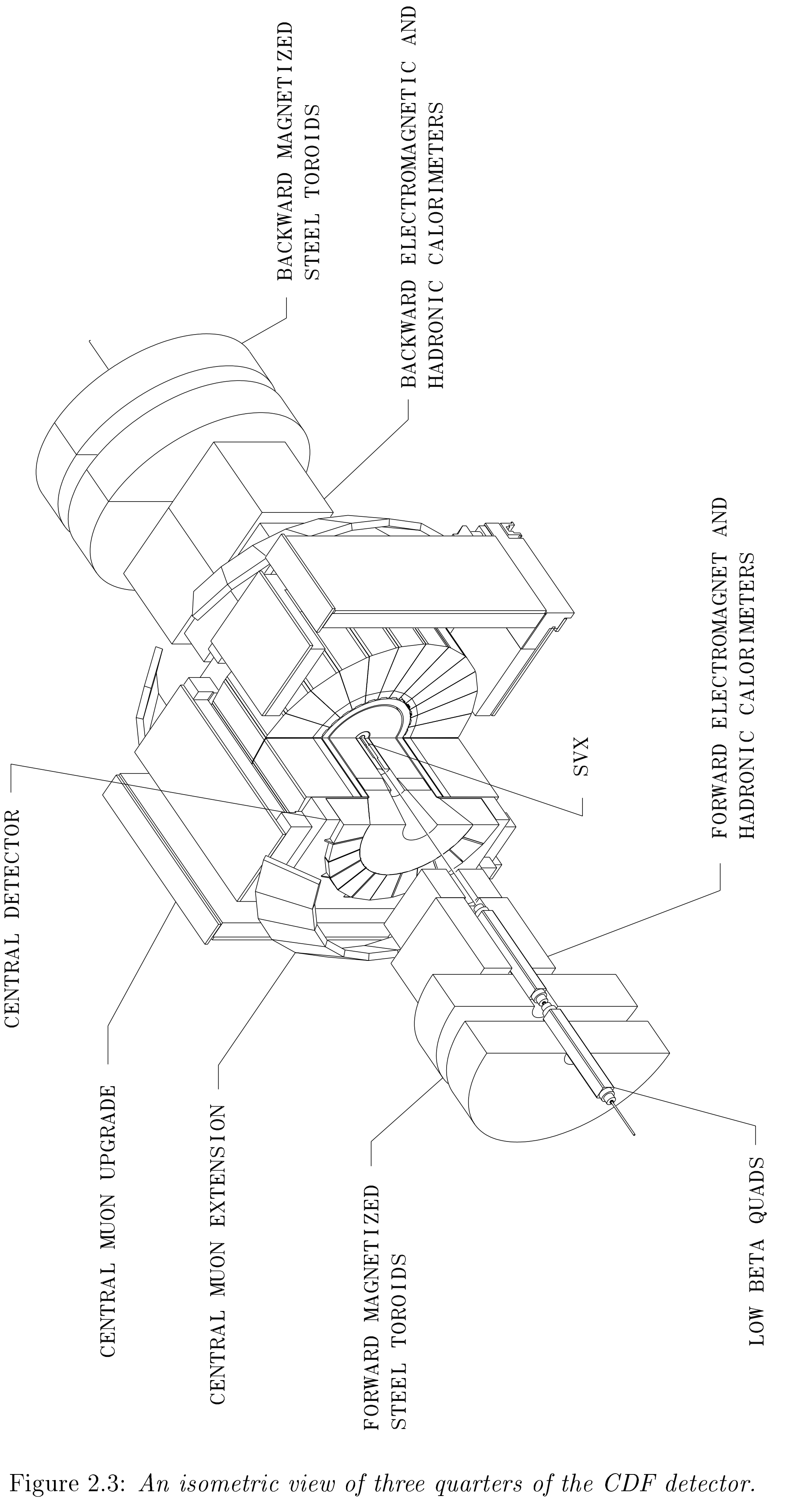

Figure 2.3: *An isometric view of three quarters of the CDF detector.*

the strip pitch of the inner three SVX layers is 60 μm and that for the outermost layer is 55 μm. The average position resolutions for the SVX and the SVX' were measured to be 13 μm and 11.6 μm, respectively, and the high transverse momentum (asymptotic) impact parameter resolution was determined to be 17 μm for the SVX and 13 μm for the SVX'.
As shown in figure 2.5, the outside end of each ladder has a small circuit board that contains the front end readout chips, which serve 128 channels. Because the ladder widths increase with increasing r, the number of readout chips on a given ladder module depends upon the layer in question. The innermost layer, for example, has two readout chips per ladder module whereas the outermost layer has six chips per ladder module. The total number of instrumented strips in the SVX is 46080.
The readout electronic typically generate $\sim$ 50 W of heat in each of the two barrels. Cooling pipes transport chilled de-ionized water at a temperature of 13 °C and a flow rate of 10 g/s to the beryllium bulkhead (see figure 2.4) and the readout circuit boards (see figure 2.5) to maintain an operating temperature near 20 °C. The cooling circuits runs at a sub-atmospheric pressure to minimize the potential damage due to breach in the cooling pipes. Controlling the temperature not only minimize leakage currents in the silicon microstrips and prevents damage to the front end electronics, but also discourages thermal gradients in the mechanical support structure that can distort the internal alignment of the SVX.

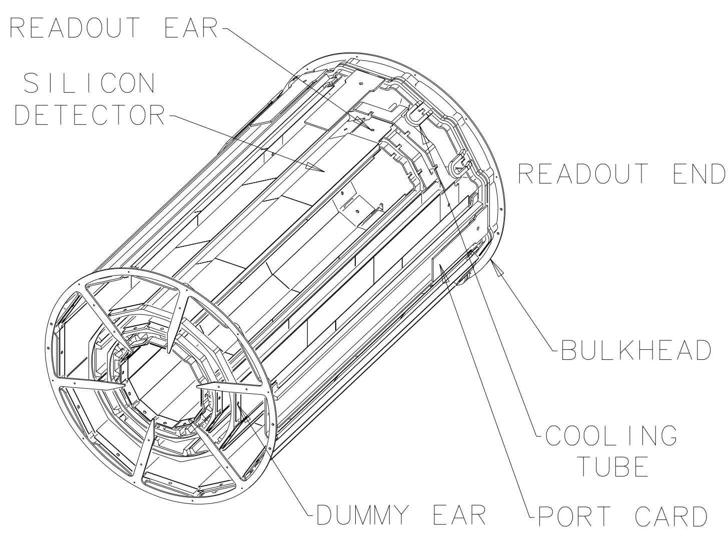

Figure 2.4: *Isometric view of one of the two silicon microstrip vertex detector barrels. The dummy-ear sides of both barrels are conjoined (with an effective gap of 2.15 cm) at* $z = 0$ *position inside the CDF detector.*

Table 2.2 resumes the main properties of the SVX detector. During the Run I no trigger system was based on the informations collected by SVX, informations used only by offline codes; such a trigger (SVT) has been implemented for the Run II data taking.

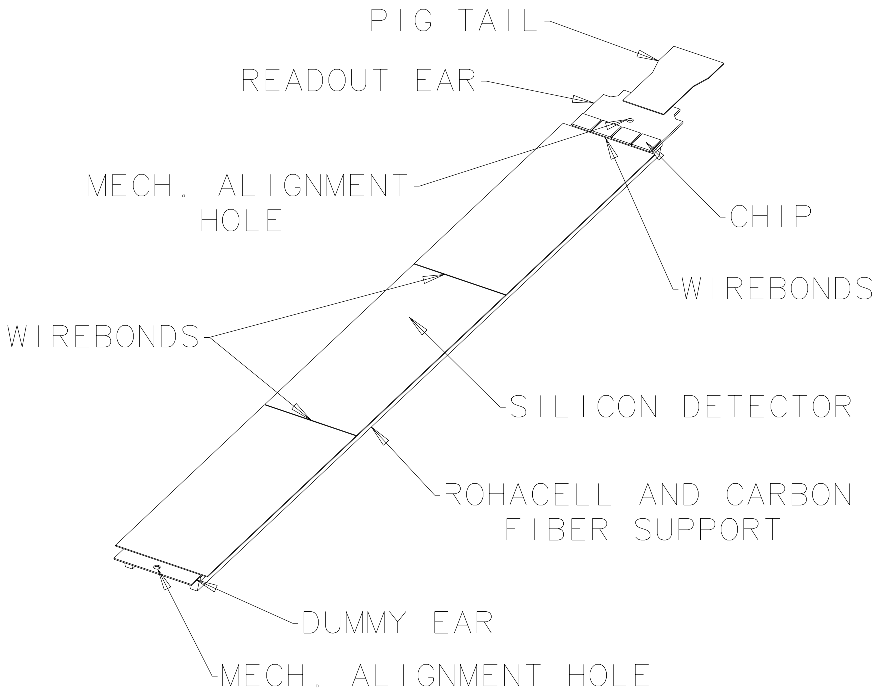

Figure 2.5: *Layout of a ladder module in the third layer of the SVX. Three single sided silicon microstrip detectors are wire bonded together to constitute each ladder module.*

Layer	Width (μm)	Active width (μm)	Radius (cm)	Pitch (μm)	Channels
0	16040	15300	3.005	60	256
1	23720	22980	4.256	60	384
2	31400	30660	5.687	60	512
3	42925	42185	7.866	55	768

Table 2.2: *Geometrical properties of the SVX silicon layers.*

2.3.2 VTX detector

A vertex time projection drift chamber (VTX) surrounds the SVX. It was designed to measure the trajectories of charged particles in the $r-z$ plane in the pseudorapidity range $|\eta| \lesssim 3.0$. The VTX is important for the determination of the z position of the primary vertex and the identification of multiple interactions in the same beam crossing. The VTX resolution of a primary vertex location along the beamline, nominally 2 mm, depends on the number of detected tracks originating from that location and the number of primary $p\overline{p}$ interactions in the event and is limited by the multiple scattering of the tracks inside SVX. Table 2.3 presents the technical characteristics of the VTX detector.

2.3.3 The Central Tracking Chamber

The most prominent subsystem in the CDF detector is the central tracking chamber, or CTC. It is the only CDF tracking device that can perform three dimensional momentum and position measurements, both of which are essential to the reconstruction of exclusive B-meson decays. The CTC surrounds the VTX and SVX subsystems and has a coaxial bicylindrical geometry with a 3201.3 mm length (including the endplates), a 2760.0 mm

Length	3.2 m
Diameter	50 cm
Pseudorapidity coverage	$\|\eta\| \leq 3.5$
Modules	28
Sense wires	8412
Maximum drift distance	4 cm
Electric field	1.6 kV/cm
Readout gain	5×10^3
Gas	*Argon/Ethan/Ethanol* (49.6%:49.6%:0.8%)
z spatial resolution	200 μm
z spatial resolution extrapolated to the vertex	2 mm

Table 2.3: *VTX technical characteristics.*

outer diameter, and a 554.0 mm inner diameter. Aluminum is used in the construction of the outer cylinder; carbon fibre reinforced plastic constitutes the inner cylinder wall.
The CTC is a drift chamber that contains 84 layers of 40 μm diameter gold-plated tungsten sense wires arranged into nine 'superlayers', five of which have their constituent sense wires oriented parallel to the beam axis (axial superlayers), and four of which have their wires canted at angles of either $+3°$ or $-3°$ with respect to the beamline (stereo superlayers). The innermost and outermost sense wires have radii of 309 mm and 1320 mm, respectively. The axial and stereo superlayers alternate with increasing radius and each consists of twelve and six sense wire layers, respectively. The configuration is illustrated in figure 2.6, which shows the wire slot locations in the aluminum endplates. The majority of the CTC pattern recognition is done using data from the axial layers, which provide tracking information in the $r - \phi$ view. The stereo layers furnish tracking information in the $r - z$ view.
The superlayers are functionally segmented into open drift cells. A drift cell contains a superlayer of (either 12 or 6) sense wires alternating with (either 13 or 7) stainless steel potential wires, which serve to control the gas gain on the sense wires. Two planes of stainless steel field wires on either side of the sense wire superlayers define the fiducial boundaries of each drift cell and control the strength of the electric field in the $\lesssim 40$ mm drift regions. The number of cells in each superlayer increases with r such that the drift distance, which translates into a maximum drift time of ~ 800 ns, is approximately constant for all cells in the CTC. To keep the electric field uniform throughout the fiducial volume of every drift cell, extra stainless steel shaper and guard wires are located near the cell perimeters, bringing the number of wires in the CTC to a total of 36504. This translates to a total wire tension of 245 kN and a combined wire length that is in excess of 110 km. As is evident in figure 2.6, the CTC drift cells are tilted such that the angle between the radial direction and the electric field direction is approximately 45°. Such a large cant angle is necessary to offset the 45° Lorentz angle, which results from the combined effects of the ~ 1.4 T magnetic field, the argon-ethane-ethanol gas mixture used (in the proportions 49.6% : 49.6% : 0.8%), and the relatively low ~ 1.35 kV/cm electric field. The drift trajectories in the CTC are therefore approximately parallel to the azimuthal direction. Every high transverse-momentum track passes close to at least one sense wire in each superlayer

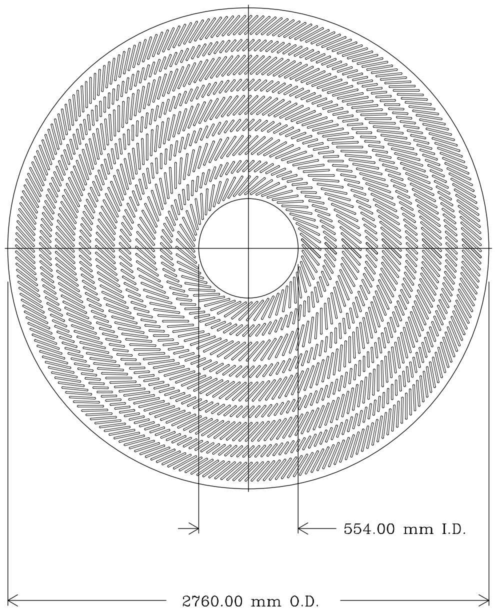

Figure 2.6: *Aluminum endplate of the central tracking chamber (CTC), viewed from along the beam axis. The wire slot locations for the alternating axial and stereo superlayers are apparent.*

Preamplifiers mounted on the endplates of the CTC are connected to the sense wires, whose analog signals are amplified further, shaped, and discriminated by circuitry mounted on the solenoid return yoke. The discriminator signals undergo time-to-digital (TDC) conversion in a counting room located at the end of 70 m of flat cable. The 1 ns resolution TDCs can record > 7 hits per wire per event. The CTC double track resolution is < 5 mm due to the approximately 100 ns minimum separation between two resolved hits. The CTC has a single hit resolution of < 200 μm, and the overall momentum resolution of the combined SVX-CTC system is $\delta_{P_T}/P_T = [(0.0009 P_T)^2 + (0.0066)^2]^{1/2}$, where P_T is the transverse momentum measured in units of GeV/c. It's worthwhile to remind here that only tracks with transverse momentum $P_T \gtrsim 300$ MeV/c are able to cross all the nine superlayers, while the others loop inside the chamber; besides, the P_T resolution is function also of the pseudorapidity, since the high-η tracks don't cross all the superlayers. The high signal collection speed and the detection efficiency of the chamber allow the use of the CTC also as a trigger device. A fast processor, CFT (Central Fast Tracker), finds high P_T tracks: the output signal, and the signals collected by the calorimeters and muon chambers, provide the fast reconstruction of high-momentum electrons and muons.
During the Run IB the electronic for the readout of the ionization energy loss (dE/dx) has been added to 54 layers, with a resolution of $\sim 15\%$, increasing thus the separation between electrons and charged pions up to a $P_T < 4$ GeV/c, and between pions and $K^{\pm}$ up to $P_T < 700$ MeV/c. Table 2.4 resumes the features and performances of the central tracking chamber.

Internal diameter	55.4 *cm*
External diameter	276 *cm*
Length	3214 *cm*
Total wires	30504
Sense wire layers	84
Superlayers	9
Distance between sense wires	10 *mm*
Sense wires stereo angle	$0° \ +3° \ 0° \ -3° \ 0° \ +3° \ 0° \ -3° \ 0°$
Cells angle	45°
Sense wires diameter	40 μm *gold-plated Tungsten*
Field wires diameter	140 μm *stainless steel*
Gas	*Argon/Ethan/Ethanol* (49.6%:49.6%:0.8%)
Electric field uniformity	$dE_o/E_o \sim 1.5\%$ (*rms*)
r–ϕ spatial resolution	200 μm
z spatial resolution	4 *mm*
P_T resolution	$\delta P_T/P_T^2 \leq 0.002\ (GeV/c)^{-1}$

Table 2.4: *Properties and performances of the CTC.*

2.3.4 Central Drift Tube Array

The central drift tube array, or CDT, is situated at radius of 1.4 m, between the outer cylinder of the CTC and the inner wall of the solenoid cryostat. The CDT system consists of stainless steel circular tubes; these are 1.27 cm in diameter, 3 m in length, and 2016 in number. Closely packed into three layers, the tubes are each strung with 50 μm diameter stainless steel anode wires. By virtue of its charge division capability on the anode wires, the CDT can provide tracking information in both the $r-\phi$ and $r-z$ views with a respective resolution of 200 μm and 2.5 mm. For the analysis described in this thesis, CDT tracking information was not used explicitly in the reconstruction of particle tracks; however, the CDT was used to identify cosmic ray muons as coincident hits with $\Delta\phi \sim 180°$. Cosmic ray muons were used to perform the initial relative alignment of the SVX, VTX, and CTC subsystems within the CDF detector.

2.3.5 Tracks reconstruction

In a homogeneous magnetic field a charged particle follows an helicoidal trajectory, with the axis parallel to the field. This trajectory is described in CDF using the following 5 parameters:

$cot\theta$, cotangent of the polar angle at the point of minimum distance from the z axis;
C , curvature (same sign of the electric charge);
z_0 , z coordinate at the point of minimum distance from the z axis;
d , impact parameter (minimum distance between the helix and the z axis);
ϕ_0 , azimuthal direction at the point of minimum distance from the z axis.

The track reconstruction procedure inside the silicon detector is based on a, so called, "Outside-In" algorithm. A track fitted inside the CTC defines a "road" whose size is

related to the covariant matrix; the road is propagated inside the SVX and the hits[4] found inside the road are associated to the track. Each time an hit is associated, moving from the outermost layer to the innermost, the track is refitted and new track parameters are calculated; then the track is again propagated to the next SVX inner layer.
The impact parameter measurement is fundamental in this analysis, in order to highlight the presence of secondary vertexes. The error on this variable is due to two different contributions: the first is the limited spatial resolution of the primary vertex position; the second one is due to the intrinsic resolution of the tracking apparatus. This second contribution is shown in figure 2.7 as a function of the track transverse momentum. The

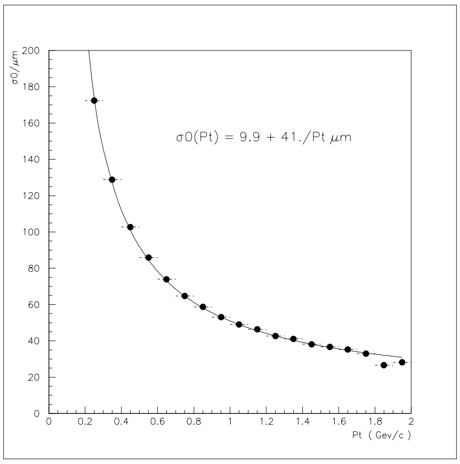

Figure 2.7: *Impact parameter resolution as a function of the track transverse momentum, SVX informations have been included.*

limited resolution for low transverse momentum tracks is due to multiple scattering. The fit with the function:

$$\sigma_d(P_T) = A + B \cdot \frac{1}{P_T}$$

gives: $A \approx 10\ \mu$m e $B \approx 41\,\mu$m GeV/c.
The asymptotic resolution ($P_T \to \infty$), A, depends on the distance of the first detection plane from the interaction point and on the intrinsic resolution of the detector. The slope B depends on the amount of material causing multiple scattering.

2.4 Calorimeters

A system of calorimeters surrounds the tracking volume and the solenoid coil. Their purpose is to measure the energy of electrons and photons as well as of "jets" of particles. The system is composed by an electromagnetic section followed by an hadronic section and since the particles originating from the $p\overline{p}$ collision are uniformly distributed in $\eta - \phi$ space it's segmented into projective towers that point toward the nominal $p\overline{p}$ interaction point. The CDF detector is divided into a central ($|\eta| < 1.1$)[5], two plug

[4] A hit is a reconstructed charge cluster.
[5] The central hadron detector is mechanically composed by a "Central" and an "End Wall" subsections which are based on similar detection units, except for geometric details.

($|1.1 < |\eta| < 2.4)$) and forward-backward ($2.5 < |\eta| < 4.2$)[6] regions (see figure 2.2). All the CDF calorimeters are sampling devices with the active material being scintillating plastic for the central electromagnetic (CEM) central hadronic (CHA) and wall hadronic (WHA) while it is 50% – 50% Argon-Ethan gas mixture for the plug electromagnetic (PEM) plug hadronic (PHA) forward electromagnetic (FEM) and the forward hadronic (FHA) calorimeters. The absorbing materials are lead for the electromagnetic and iron for the hadronic calorimeters. Table 2.5 summarizes some characteristics of the CDF calorimeters.

Electromagnetic calorimeters			
	Central	End Plug	Forward
$|\eta|$ coverage	$0 - 1.1$	$1.1 - 2.4$	$2.2 - 4.2$
$\Delta\eta \times \Delta\phi$ granularity	$\sim 0.1 \times 15^o$	0.09×5^o	0.1×5^o
Active material	*Scintillator*	*Proportional tubes*	
Active material size	$0.5\ cm$	$0.7 \times 0.7\ cm^2$	$1.0 \times 0.7\ cm^2$
Absorber	Pb	Pb	$94\%Pb, 6\%Sb$
Absorber thickness	$0.32\ cm$	$0.27\ cm$	$0.48\ cm$
Energy resolution at 50 $GeV(\sigma/E)$	2%	4%	4%

Hadronic calorimeters				
	Central	End Wall	End Plug	Forward
$|\eta|$ coverage	$0 - 0.9$	$0.7 - 1.3$	$1.3 - 2.4$	$2.3 - 4.2$
Tower size $\Delta\eta \times \Delta\phi$	$\sim 0.1 \times 15^o$	$\sim 0.1 \times 15^o$	0.09×5^o	0.1×5^o
Active material	*Scintillator*		*Proportional tubes*	
Size	$1.0\ cm$	$1.0\ cm$	$1.4 \times 0.8\ cm^2$	$1.5 \times 1.0\ cm^2$
Absorber	Fe	Fe	Fe	Fe
Thickness	$2.5\ cm$	$5.1\ cm$	$5.1\ cm$	$5.1\ cm$
Energy resolution at 50 $GeV(\sigma/E)$	11%	14%	20%	20%

Table 2.5: *Characteristics of the CDF electromagnetic and hadronic calorimeters.*

2.5 Central electromagnetic calorimeter

The central electromagnetic calorimeter (CEM) is fundamental in this analysis since it's used to identify the photons from the $\eta \to \gamma\gamma$ decay. The CEM calorimeter has a cylin-

[6]The F-B calorimeters are placed at a distance of 6.5 m from the interaction vertex; the presence of the focusing quadrupoles in the same region limits the azimuthal coverage in the region $|\eta| \geq 3.6$, this implies that the missing E_T can be calculated only up to $|\eta| \leq 3.6$.

drical geometry with an inner radius of $\simeq$ 172 cm and a radial depth of 32 cm ($\simeq 18X_0$), enough to contain the electromagnetic showers of electrons and photons, created by virtue of the bremsstrahlung and pair production processes when an energetic photon or electron enters the CEM volume (see also figure 5.12). The CEM provides full azimuthal coverage and, in order to make mechanical construction easier and to be able to roughly locate incoming particles, it is divided into 48 wedges, each covering 15° in ϕ. The wedges are grouped into four arches; two arches of wedges each cover the positive z region, with the remaining two arches covering the negative z region. Each wedge is segmented in ten towers each extending $\sim$ 0.11 units in pseudorapidity and 15° in ϕ, as can be seen in figures 2.2 and 2.8. The towers have a projective geometry pointing back to the nominal interaction region since we want to contain the energy deposition of photons and jets flying out of the p$\overline{\text{p}}$ collision point in as few towers as possible and avoid losing energy in the tower boundary regions. The central electromagnetic calorimeter is a sampling

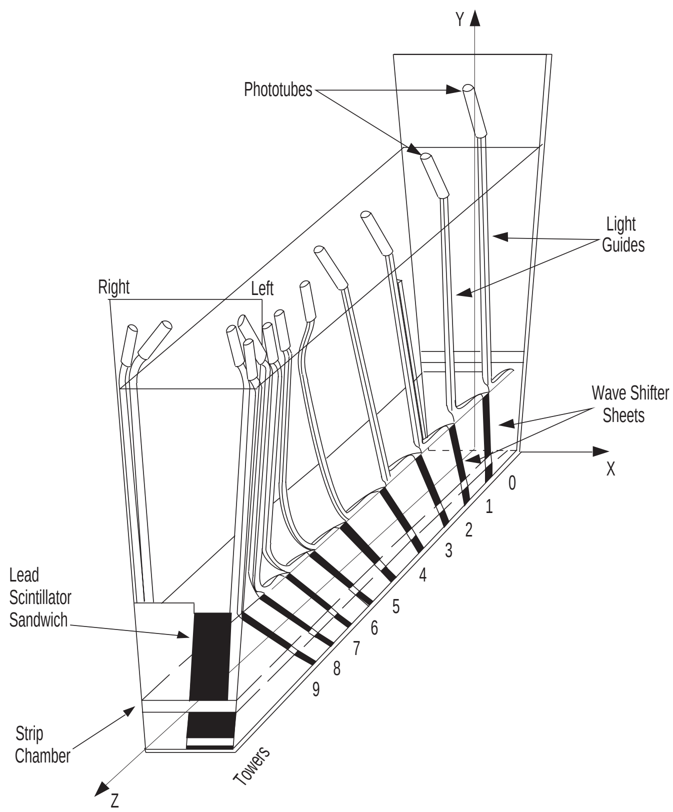

Figure 2.8: *One of the wedges of the CEM calorimeter with the towers that form it. Also shown are the wavelength shifter and the light guides that carry to the photomultipliers the photons produced in the plastic scintillators.*

calorimeter like all the CDF calorimeters. The towers are sandwich structures of 31 layers of 5 mm thick polystyrene scintillator interleaved with 30 layers of 0.318 cm thick lead. Lead is chosen for its high density and atomic number which ensures that the radiation length in the CEM is small (around 1.8 cm) and therefore results in a reasonable size calorimeter. In order to maintain a constant radiation length thickness as polar angle varies acrylic is substituted for lead in certain layers of the $|\eta| > 0.2$ towers .

The electrons of an electromagnetic shower excite molecules in the scintillator material which consequently emit blue light that is collected in 3 mm thick acrylic wavelength shifter (WLS) sheets. There is one WLS sheet at each ϕ side of a tower collecting light from all 31 scintillator layers in that tower and transporting it through light guides into the two photomultiplier tubes per tower (see figure 2.8). The (total of 956) photomultipliers operate at 1 kV giving a gain of about 10^5. Twelve-channel charge integrating amplifier modules are used to read out the photomultipliers; they saturate at about 350 GeV and have a high gain for good pedestal systematics for minimum ionizing particles (muons deposit about 300 MeV of their energy in the CEM). Each ϕ side of a wedge is covered by 4.76 mm of steel skin and between the wedges there are gaps of 6.4 mm in ϕ. WLS sheets steel skins and gaps represent 4.8% of the azimuth. In order to avoid having photons and electrons traverse the ϕ gaps escaping detection, there are crack detectors in front of the ϕ boundaries, each consisting of a preradiator (9 radiation lengths thick uranium bar which forces the incoming particles to shower) and a proportional chamber which detects particles going through the cracks. The information from the crack detectors is used for veto purposes.

Note that the CEM design with the steel skins and ϕ gaps between wedges does not allow electromagnetic showers to have a significant fraction of their energy shared between neighboring wedges. The transverse development of electromagnetic showers is characterized by the Moliere radius, R_M with $\sim$ 95% of the shower energy contained within a radius of $2R_M$. For the CEM material $R_M \simeq 3.53$ cm, resulting in electromagnetic showers mostly contained in a single CEM tower. This fact along with the good CEM hermeticity for the longitudinal development of the showers (depth of 18 X_0) and the scintillator and WLS characteristics results in the CEM measuring the energy of electromagnetic showers with a resolution of:

$$\frac{\sigma_E}{E} = \sqrt{\left(\frac{13.5\%}{\sqrt{E \cdot \sin\theta}}\right)^2 + (2\%)^2}.$$

The CEM is followed by an hadronic section, with the same $\eta - \phi$ segmentation but with coverage up to $|\eta| < 0.9$. Each tower of the central hadronic calorimeter is composed of 32 layers of steel and scintillators. The light produced inside the scintillators is collected, transported and detected with an apparatus similar to the CES one. The total interaction length, for orthogonally incident particles, is $\sim 5\lambda$. The energy resolution for the central hadron calorimeter has been measured on a test beam with charged π and is equal to:

$$\frac{\sigma_E}{E} = \sqrt{\left(\frac{75\%}{\sqrt{E \cdot \sin\theta}}\right)^2 + (3\%)^2}.$$

2.5.1 Proportional chambers, *CES*

Proportional strip chambers are inserted inside the CEM wedges between the eighth lead layer and the ninth scintillator layer. This depth corresponds to $\sim 5X_0$ from the CEM face and $\sim 5.9X_0$ from the $p\overline{p}$ interaction point. At this depth the electromagnetic shower for a particle of energy $\sim 1 \div 10$ GeV (see figure 5.12) reaches its maximum development.

The CES chambers [6] are essential for the determination of the shower position inside the EM tower and the shower transverse development as a means to distinguish electromagnetic showers induced by electrons or photons from π^0.

The CES chambers are proportional chambers with wires running along the z direction and strips along the ϕ direction, i.e. perpendicular to the wires, thus enabling the CES to locate a shower along both the ϕ (from wire information) and z (from strip information) coordinates. The gas used is 95% argon and 5% CO_2 and the high voltage (1420 V corresponding to a prompt gain of 10^3) is set up to give an occasional (few %) channel saturation for 150 GeV/c test beam electrons near normal incidence.

A right handed local coordinate system $(x_{CES}, y_{CES}, z_{CES})$ is defined for each CEM wedge as follows: the z_{CES} coordinate is coincident with the global CDF z coordinate. The x_{CES} axis is parallel to the face of the CES, with $x_{CES} = 0$ in the centre of the chamber and with positive values for increasing ϕ. The y_{CES} coordinate is orthogonal to the face of the chambers. The CES chambers are physically segmented in z into two pieces per wedge one at $6.2 < |z_{CES}| < 121.2$ cm (i.e. towers 0 to 4) and the other at $121.2 < |z_{CES}| < 239.6$ cm (towers 5 to 9). Each CES segment has 32 wires spaced 1.45 cm apart, covering the region $-22.5 < x_{CES} < 22.5$ cm. There are 128 strips per wedge, each width $\simeq 0.159$ cm; 69 in the first half-wedge, 59 in the second one, spaced 1.67 and 2.01 cm apart respectively.

The response of the CES as a function of the incident energy is not linear, since the depth at which the transverse development of an electromagnetic shower reaches its maximum increases with the energy of the incident photon or electron (see figure 5.12). The response of the CES (both in energy and in position) is a function of $\sin\theta$ due to the widening of the showers in the strip view as can be seen in figure 2.9.

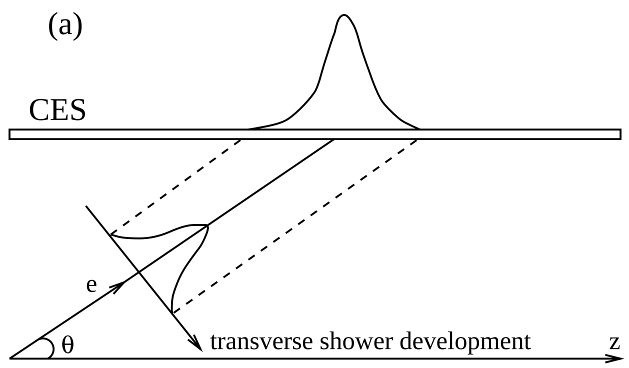

Figure 2.9: *The* $1/\sin\theta$ *widening of the showers in the strip view.*

The shape of the transverse development of the electromagnetic shower can be used to distinguish between showers induced by a single electron/photon or a neutral pion (or an η). The $\pi^0 \to \gamma\gamma$ and $\eta \to \gamma\gamma$ decays produce two photons which the more are collimated the more is the energy of the generating particle: this can lead the two γs to hit the same tower and then to an overlap of the two electromagnetic showers. Also for this reason the presence for the proportional chambers is fundamental (see [7]).

The γ/π^0 separation has been increased with the introduction, for the Run1b, of one proportional chamber layer in the region $|\eta| < 0.7$. These chambers, called CPR (Central PreRadiator)[2], are placed immediately outside the solenoid coil, which is used as radiating material. The usefulness of this chamber is evident especially for π^0s (or ηs) with initial momentum of few tenths of GeV/c which decay into two photons. For these energies the small opening angle of the photons prevents the discrimination of the signal into two separate showers in the CES detector. The CPR operating idea is then based on the simple consideration that the probability to generate a shower inside the detector is higher for two photons with respect to one single photon (almost double). So, even if it's difficult to separate the two showers, it's possible to apply some selections based on two different probabilistic behavior of π^0s and single photons.

2.6 μ chambers

The ability to identify muons and their trajectories is essential to the reconstruction of J/ψ mesons in the dimuon channels. Muon identification can be achieved by exploiting the relatively high muon critical energy[7], which is several hundred GeV in materials such as iron[3], significantly higher than the critical energy for other ionizing particles. This ability of the muon to penetrate matter thus motivates the location of the muon subsystems in the outer regions of the CDF detector that can only be reached by those charged particles that originate from the interaction region and that penetrate the intervening material. This material, consisting primarily of the calorimeters, serves to filter out the majority of hadrons and electrons before they reach the muon subsystems. Refer to figure 2.2 for the locations of the three central muon subsystems: the central muon detector (CMU), the central muon upgrade detector (CMP), and the central muon extension (CMX). A map of the $\eta - \phi$ muon detection coverage in the central region is shown in figure 2.10. The forward muon toroid subsystem is not considered in this study due to its poor intrinsic momentum resolution and the lack of overlap in acceptance between it and the CTC and SVX tracking systems.

	CMU	CMP	CMX
$\lvert\eta\rvert$ coverage	0–0.63	0–0.60	0.62–1.0
ϕ coverage	84%	63%	71%
minimum track P_T (GeV/c)	1.4	2.7	1.6

Table 2.6: *μ detectors properties.*

2.6.1 Central Muon Detector

The CMU covers the region $55° \leq \theta \leq 125°$ ($|\eta| \leq 0.6$) and resides on the outer edge of the central hadronic calorimeter, 347 cm from the beam axis, as indicated in figure 2.11. The detector keeps the 24 wedge structure, each with an effective ϕ coverage of 12.6° by means of three flanked modules. A CMU module, shown in figure 2.12, consists of four towers, each with four layers of rectangular drift cells. The outermost and second innermost cells in each tower are oriented such that their sense wires lie on a radial that originates from the centre of the CDF detector. The innermost and second outermost drift cells lie on another radial that is offset from the first by 2 mm at the midpoint (in r) of the CMU. The offset cells in each tower resolve the side of the radial, in azimuth, on which the track passed. As indicated in figure 2.12, the absolute difference in drift electron arrival times for a pair of cells having sense wires on the same radial determines the angle between the candidate muon track and that radial. This angle can be related to the transverse momentum of a muon candidate and is therefore exploited by the trigger

[7]The muon critical energy is the energy at which losses due to radiation and ionization are equal.

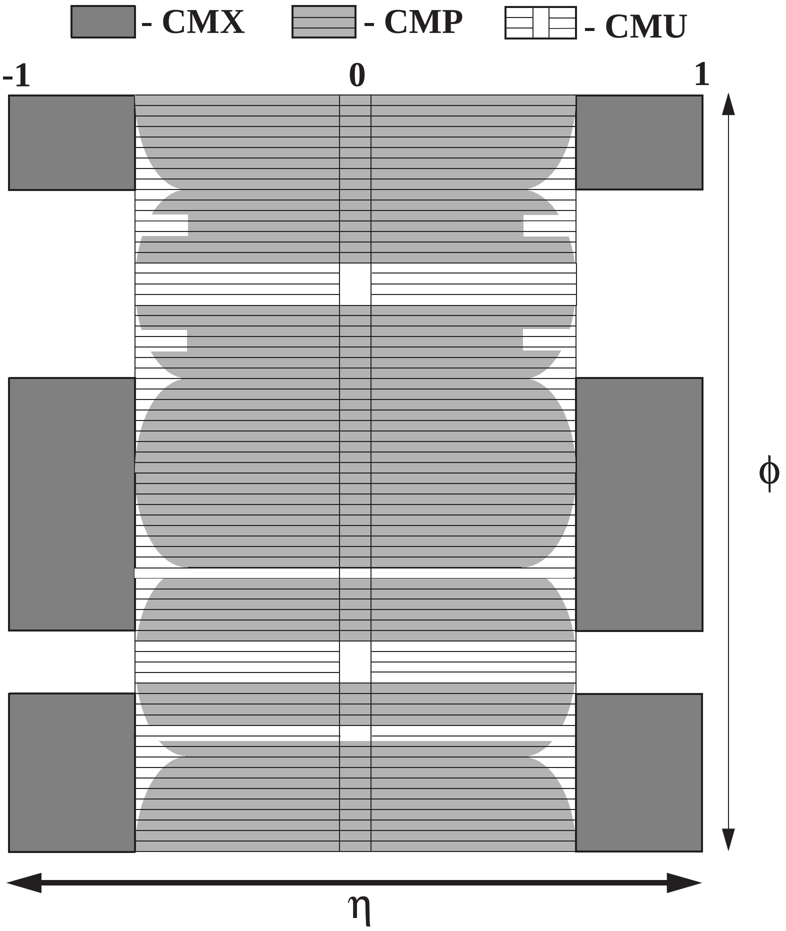

Figure 2.10: *Coverage of the central muon subsystem in pseudorapidity (η) and azimuth (ϕ). The lack of CMX coverage at $\phi \sim 90°$ and $\phi \sim 270°$ results from the interference due to the Main Ring bypass beampipe and the concrete collision hall floor, respectively.*

system (refer to section 2.7.1). A drift cell in the CMU, shown in figure 2.13, is rectangular with dimensions 63.5 mm x 26.8 mm x 2261 mm and has a single 50 μm stainless steel sense wire strung through its centre. The drift cells are operated in limited streamer mode using a 50:50 admixture of argon and ethane gas, and potentials of +3.15 kV on the sense wires and -2.5 kV on the I-beams, which are electrically isolated from the top and bottom aluminum plates by 0.62 mm of insulation. The position of a muon candidate track along the sense wire (z) direction can be determined with a resolution of 1.2 mm using charge division electronics. The position resolution in the drift (ϕ) direction is 250 μm.

2.6.2 Central Muon Upgrade

An average of 5.4 pion interaction lengths lies between the CMU and the $p\overline{p}$ collision region, resulting in approximately 1 in 200 high energy hadrons traversing the calorimeters unchecked. This 'noninteracting punch-through' results in an irreducible false muon background rate. The central muon upgrade detector (CMP), shown in figures 2.2 and 2.3, was commissioned to contend with this punch-through hadron rate. The CMP surrounds the central region of the CDF detector with 630 tons of additional steel. The geometry

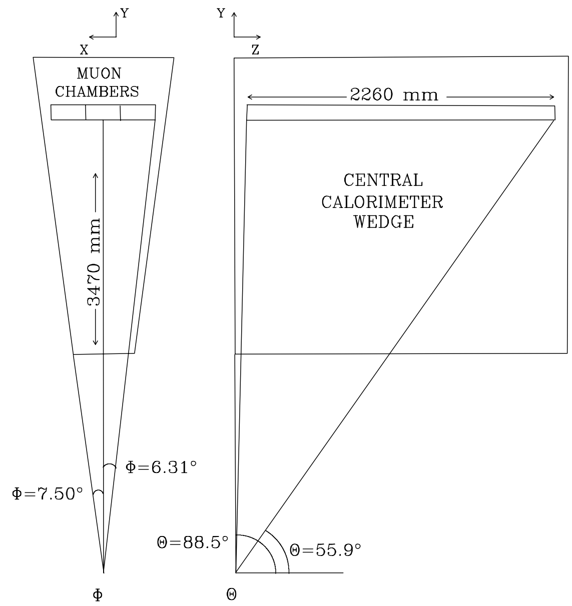

Figure 2.11: *The layout of a central muon (CMU) wedge with respect to a central calorimeter wedge in both azimuthal (left) and polar (right) views.*

is box-like, with the return yoke of the solenoid providing the absorption steel on the top and bottom, and two retractable 60 cm thick slabs arranged as vertical walls on each side. The additional absorption material brings the number of pion interaction lengths to 7.8 at $\eta = 0$. Figure 2.10 illustrates the variation in pseudorapidity coverage with azimuth caused by the geometry of the CMP. The active planes of the CMP consist of four layers of half-cell staggered single-wire drift tubes operating in proportional mode. Each drift cell, of which there are 864 in the CMP, consists of a rectangular extruded aluminum tube 25.4 mm high, 152.4 mm wide, and with a length that depends upon where the tube is mounted. The anode, a 50 μm gold-plated tungsten wire, is biased to a potential of 5.6 kV, the wide central field-shaping cathode pad is biased to 3 kV, and the eight narrow field-shaping strips have decreasing voltages from the centre of the cell out to the edges. The maximum drift time is 1.4 μs.

2.6.3 Central Muon Extension

The central muon extension, or CMX, provides additional pseudorapidity acceptance in the region $0.65 \leq |\eta| \leq 1.0$. Shown in figures 2.2 and 2.3, the CMX modules possess geometries that correspond to the surfaces of two halves of truncated cones each with a base at $z = 0$ and an axis along either the proton or antiproton direction. The azimuthal coverage of the CMX is not continuous; due to the floor of the collision hall, there is a 90° gap in ϕ at the bottom of the CDF detector, and, due to the Main Ring bypass beampipe, there is a 30° gap at the top of the detector. The 1536 proportional drift cells that constitute the CMX modules are shorter than, but otherwise identical to, those used in the CMP. No additional absorber was added between the CMX and the interaction region; however, the smaller polar angle through the hadronic calorimeter and magnet return yoke yields a shielding thickness of 6.2 pion interaction lengths at $\theta = 55°$. The CMX is organized into four stacks, two on the proton side and two on the antiproton side of the

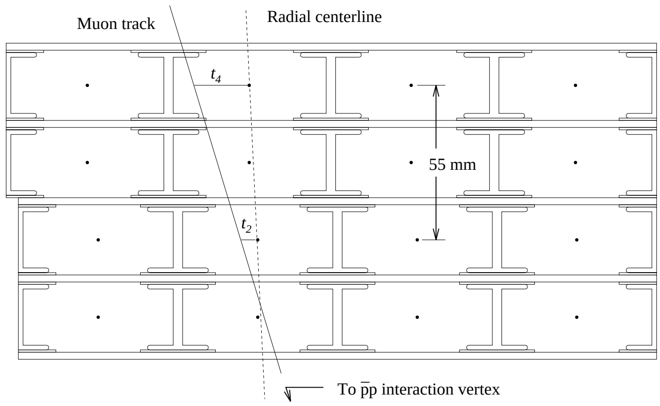

Figure 2.12: *Layout of a central muon detector (CMU) module showing the four towers, each with four layers of rectangular drift cells. The outermost and second innermost cells in each tower are oriented such that their sense wires lie on a radial that originates from the geometric centre of the CDF detector. The other two drift cells are offset to determine which side of the radial the track passed. The quantities t_2 and t_4 represent drift electron arrival times; their difference, $|t_4 - t_2|$, determines the angle between the candidate muon track and the radial, thus providing a crude but fast measurement of transverse momentum that can be used in a low level trigger. Analogous information from t_1 and t_3 yields a second independent measurement.*

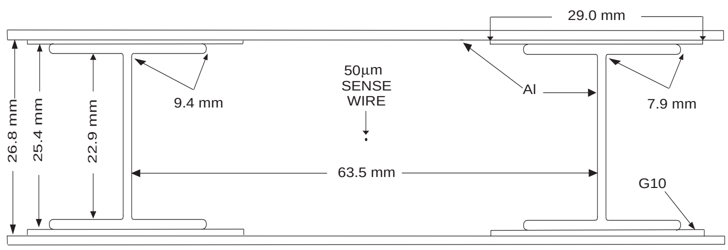

Figure 2.13: *Layout of a central muon detector (CMU) drift cell, showing the 0.79 mm aluminum top and bottom plates and the aluminum I-beams that separate adjacent towers.*

CDF detector. Each stack consists of eight modules, which each subtend 15° in azimuth. A module comprises 48 proportional drift cells that are grouped in eight half-cell staggered layers of six tubes each. The maximum CMX drift time, 1.4 μs, is such that the spread of arrival times due to background particles is short by comparison. Background rejection and a high speed trigger are provided by an array of scintillation counters mounted on the inner and outer sides of each CMX module. Four such scintillators, each with its own photomultiplier tube, are located on both sides of every 15° CMX module, for a total of 256 scintillation counters. Background effects are vetoed in the trigger by requiring that both the inner and outer scintillators adjacent to a CMX hit produce pulses that are coincident with the $p\overline{p}$ beam crossing to within a few nanoseconds.

2.7 The trigger

In the course of Run1 data acquisition, proton and antiproton bunch crossings in the Tevatron collider occurs every 3.5 μs, corresponding to a crossing frequency of 286 kHz. With typical instantaneous luminosities of $\mathcal{L} = 5 \times 10^{30}\text{cm}^{-2}\text{s}^{-1}$ and a measured $p\overline{p}$ total cross section of $\sigma_{tot} = 80.03 \pm 2.24$ mb at $\sqrt{s} = 1.8$ TeV, an average of $\gtrsim 2$ $p\overline{p}$ interactions per beam crossing is expected. A CDF event, which amounts to the digitized information from a single beam crossing that can be read out from the CDF detector at a given time, had a data length of $\sim$ 165 kB. Such an event size could only be reliably written out to several 8 mm magnetic tapes at a rate of approximately 10 Hz. This constitutes the principal limitation to the CDF data acquisition rate and necessitates a trigger system that can both accommodate the $p\overline{p}$ interaction rate and select interesting physics events with a $\sim$1/30000 rejection factor. The CDF trigger consists of three successive levels, each of which imposes a logical "OR" of a limited number of programmable selection criteria that collectively reduces the data rate exposed to the next higher trigger level. The reduction in the rate presented to the higher trigger levels provides time for more sophisticated analysis of potential events with the accrual of less dead time[8].

2.7.1 General description

Level 1

The Level 1 trigger requires less time than the 3.5 μs beam crossing period to reach a decision on whether or not a given event is suitable for consideration by the higher trigger levels; it therefore incurs no dead time. At an instantaneous luminosity of $\mathcal{L} = 5 \times 10^{30}\text{cm}^{-2}\text{s}^{-1}$, the Level 1 trigger acceptance rate is approximately 1 kHz. Although it could have been configured to base its decisions on information from several different CDF subsystems, the Level 1 trigger primarily uses signals from the calorimeters and the three muon systems, CMU, CMP, CMX.
The calorimetry component of the Level 1 trigger considers analog signals on dedicated cables from the scintillator photomultiplier tubes in the central calorimeter subsystems and from cathode pads in the plug and forward calorimeter subsystems (refer to table 2.5). For the purposes of the trigger, the calorimeters are logically segmented into 'trigger towers' with $\Delta\phi = 15°$ e $\Delta\eta = 0.2$. For each subsystem listed in table 2.5, the individual tower minimum-energy thresholds can be specified to the trigger, which sums the deposited energies, weighted by the polar angle θ to determine the transverse energy $E_T = Esin\theta$, for all those trigger towers that are above these thresholds. If the total E_T, measured in this manner, exceeds a given global threshold, then the Level 1 trigger accepts the event. There is also a similar Level 1 calorimetry trigger with significantly reduced tower energy thresholds (prescaled by a factor of 20 or 40) used to collect events for trigger efficiency studies.

The muon component of the Level 1 trigger exploits the relative drift electron arrival times (Δt) between pairs of drift cell layers in a given CMU module, as described in section 2.6. Since the muon chambers are placed outside the hadronic calorimeter, and then in a weak magnetic field region, the tracks are reconstructed as straight segments

[8] In this context, 'dead time' refers to the amount of time that the CDF detector was unable to consider subsequent $p\overline{p}$ collisions.

called 'muon stubs' that were defined by the existence of any wire pair in a 4-tower 4.2° muon detector module (see figure 2.12). The trigger logic operates on these objects. The difference (Δt) on the drift time among the chambers provides a slope angle measurement, which is related to the transverse momentum of the candidate by means of:

$$\alpha \simeq \frac{eL^2B}{2DP_T}$$

where B is the magnetic field, L is the radius of the region with field and D is the distance between the muon chambers and the beam. Due to the multiple scattering inside the calorimeters (and inside the steel return yoke) and the non-uniformity of the magnetic field inside the solenoid, the measurement of the transverse momentum in the muon chambers is by far less precise than the CTC measurement.

Level 2

In a $p\overline{p}$ beam crossing for which the Level 1 trigger did not fire, a timing signal from the Tevatron announcing the occurrence of the next beam crossing would cause the stored signals in the CDF detector to be cleared in preparation for the next crossing. If the Level 1 trigger did fire, then subsequent timing signals are inhibited from clearing information stored in the CDF detector for a period of about $20-30$ μs, during which the Level 2 trigger makes its decision and $6-9$ disregarded beam crossings can occur; the dead time introduced is $\lesssim 10\%$.
With the increased processing time, the Level 2 trigger system can perform simple tracking calculations and determine basic features of the event by considering, with greater sophistication, the same dedicated calorimetry and muon signals used in Level 1. The topological structure of the event is analyzed: a fast electromagnetic and hadronic transverse-energy clustering is performed, fast tracking is executed inside the CTC with the extrapolation to the CEM deposits and to the stubs in the muon chambers, $\not{E}_T$ is measured to detect the presence of neutrinos in the event.
The fast clustering algorithm looks for towers above some "seed tower" threshold (typically 5 or 8 Ge V) and makes a list of "seed towers". Trigger towers that are above a lower "shoulder tower" threshold (typically 1 GeV less than the seed tower threshold) are kept in a separate list. Starting from the seed tower with the smallest η and ϕ, the algorithm checks which of the four nearest neighbors (the "diagonal" neighbors with different η and ϕ are not considered) are in the "shoulder tower" list and includes them in the cluster. The nearest neighbors of each of the newly included towers are checked and so on, until no more contiguous towers are found. Once a tower is included in a cluster it is not considered for any of the subsequent clusters. The process is repeated until no new seed towers exist. The energies of all the towers in a cluster are summed to form the total transverse energy E_T. Separate sums are kept for electromagnetic and total (electromagnetic plus hadronic) energies. The time needed for the energy clustering process is $\sim$ 200 ns per cluster. Finally the algorithm treats the whole detector as one cluster and calculates the global sum of energies for all towers above threshold, exactly as Level 1 did. This gives a more accurate measurement of missing transverse energy than Level 1, which is used by components of the Level 2 trigger looking for neutrinos.

The track reconstruction at Level 2 is carried out by means of the Central Fast Tracker (CFT), a pattern recognition system which reconstructs tracks with $P_T \gtrsim 2$ GeV/c inside the CTC. CFT provides measurement of the transverse momentum and initial azimuthal angle considering only the hits in the axial superlayers of the CTC, the reconstruction is then only on 2D (transverse plane). The reconstruction begins looking for a signal released in a 90 ns time window since the $p\overline{p}$ interaction and then other two signals, delayed, in the time window $530 - 690$ ns (see figure 2.14). The time drift of the electron

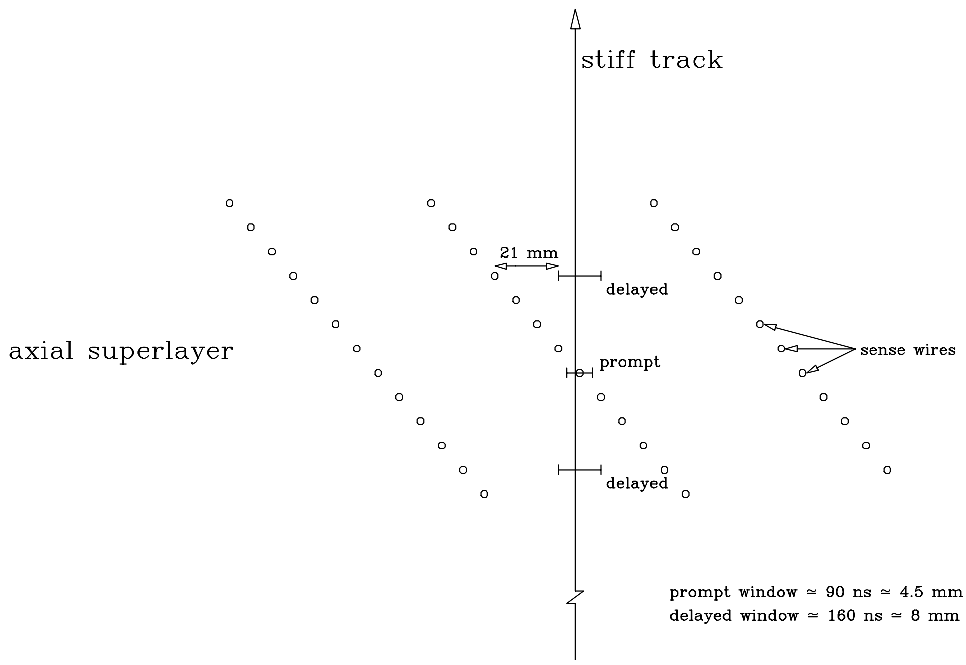

Figure 2.14: *Track crossing an axial superlayer inside the CTC. Only the sense wires are shown. The CFT processor uses prompt and delayed signals to reconstruct the track and measure its momentum.*

toward the wires provides informations about the direction and the curvature (and then the P_T) of the track. Different time windows for the delayed hits allow to select different P_T windows. Once collected all the signals inside the CTC, CFT looks for hits in the outermost superlayer and then tries to associate other hits inside roads which depend on the P_T window; 8 momentum windows between 2.2 and 27 GeV/c are considered (see table 2.7).
Using this procedure the transverse momentum resolution is $\delta P_T/P_T \sim 0.035 \times P_T$, with P_T in GeV/c. The charge identification is not reliable for high momentum tracks, for this reason the opposite sign request is applied only at Level 3, after the complete 3D track reconstruction.
The association between the list of electromagnetic clusters and of μ track segments and CFT tracks is then performed by an algorithm running on commercial Digital processors. Muon track segments reconstructed inside the the CMU, CMX and CMP must match a CFT track within an angle $\Delta\phi \leq 5°$. The electron trigger requires an alignment between the CEM cluster and the track.

At an instantaneous luminosity of $\mathcal{L} = 5 \times 10^{30}\text{cm}^{-2}\text{s}^{-1}$, the Level 2 trigger has an accepted rate of about 12Hz[11], then only $\sim 1.5\%$ of the examined events are sent to Level 3.

Run	Lower extreme of the P_T interval(GeV/c^2)							
IA	3.0	3.7	4.8	6.0	9.2	13.0	16.7	25.0
IB	2.2	2.7	3.4	4.7	7.5	12.0	18.0	27.0

Table 2.7: *Transverse momentum intervals used by CFT. The table has been optimized at the beginning of Run1b.*

Level 3

The Level 3 trigger is implemented as a software code running on a processors farm. When an event has been accepted by the Level 2, the data are digitized in $\sim$ 3 ms and sent by the DAQ to the Level 3. Over the course of the data-taking period, both the Level 3 trigger system and the DAQ system underwent several significant changes, especially during the Run1a-Run1b interval, here the final configuration is presented. The trigger system receives data fragments read out by the DAQ for a given beam crossing and 'built' by the Event-Builder into a contiguous event. The farm consists of 64 Silicon Graphics commercial processors that run a UNIX-IRIX operating system. The event reconstruction algorithms running in these calculators are similar to the ones used in the off-line event reconstruction; however, because three dimensional track reconstruction constitutes most of the Level 3 execution time, only the faster of two tracking algorithms used in the off-line code is engaged in the trigger.

The trigger algorithms for electrons require an $r-\phi$ and $r-z$ match (few centimeters) between the electromagnetic cluster in the CEM and the extrapolation of the track reconstructed inside the CTC; also a compatibility between the track transverse momentum and the cluster E_T is required. Finally, the transverse energy profile measured by the CES chamber must be consistent with an electron or photon generated shower.

The muon trigger algorithms require the stubs reconstructed in the μ chambers in association with a track identified inside the CTC; this match must be satisfied in both $r-\phi$ and $r-z$, considering the possible deflection of the track due to multiple scattering and the loss of energy inside the material.

With an instantaneous luminosity of $\mathcal{L} = 5 \times 10^{30}\mathrm{cm}^{-2}\mathrm{s}^{-1}$, the third level trigger has an accept rate of about 5 Hz.

2.7.2 $J/\psi \to \mu\mu$ triggers

The J/ψ dataset has been collected by means of dedicated triggers designed for the identification of low momentum muons.

Level 1

Two kinds of selections are implemented at Level 1: the single muon trigger, which requires a muon stub with transverse momentum higher than 6.0 GeV/c, and the double muon trigger, which requires two stubs with $P_T \geq 3.3$ GeV/c. The trigger logically divides the detector into trigger towers, each with an azimuthal amplitude $\Delta\phi = 5°$, and considers two stubs as separate entities only if they are reconstructed in two not contiguous towers, otherwise the two segments are processed by the trigger algorithm as a single

one; the two different halves of the CDF detector (east-west) and the CMU and CMX trigger towers are considered separately.
A requirement on the minimum transverse momentum of the muons is then applied by cutting on the slope of the stubs reconstructed in the μ chambers. This can be obtained by measuring the drift times in different cells of a tower (see section 2.6.1). The trigger selection requires a nominal momentum higher than 3.3 GeV/c, value for which the chambers reach the efficiency plateau (see section 3.3.3). Besides the signals in the μ chambers, also a cluster in the corresponding hadron calorimeter towers is required in a time window of 50 ns from the bunch crossing.

Level 2

All the Level 2 dimuon triggers require at least one track reconstructed inside the CTC pointing to one of the stubs, with an azimuthal separation less than 5°. The regions of the calorimeter containing a μ are then labeled as muon clusters. The trigger logic operates on these object and not on the stubs. The muon clusters have an azimuthal extension equal to a wedge and a z extension of three calorimetric trigger towers[9]. The trigger considers muon clusters reconstructed inside adjacent towers as a single 6 tower cluster. Each Level 2 dimuon trigger requires as prerequisite a specific Level 1 dimuon trigger.

Level 3

The Level 3 dimuon trigger exploits the three dimensional CTC track reconstruction. The relevant trigger for this analysis requires a two body invariant mass among 2.7 and 4.1 GeV/c^2 for the two μ candidates, but makes no opposite sign requirement. Besides, the Level 3 trigger performs a matching between the extrapolated track and the stub reconstructed in the muon chambers. This operation takes in account both the multiple scattering and the limited central chamber resolution; the imposed cut corresponds to about a 4σ acceptance window.

[9]A trigger calorimetric tower consists of two central calorimeter towers, then it covers a region $\Delta\eta \times \Delta\phi = 0.22 \times 15°$.

Bibliography

[1] F. Bedeschi *et al.* (CDF collaboration), "Design and construction of the CDF central tracking chamber", *Nucl. Instr. and Meth. A* **268**, 50 (May 1988)

[2] S. Kuhlmann, "Central Preradiator Chamber Tests", **CDF** internal note **1248**, (Jun 1990)

[3] K. Hagiwara *et al.*, "Review of Particle Physics", *Phys. Rev. D* **66**, 010001 (2002)

[4] F. Abe *et al.* (CDF Collaboration), "Measurement of the Antiproton-Proton Total Cross Section at $\sqrt{s} = 546$ and 1800 GeV", *Phys. Rev. D* **50**, 5550 (1994)

[5] F. Abe *et al.* (CDF II Collaboration), "The CDF II Detector Technical Design Report", FERMILAB-PUB-96-390-E, (Oct 1996)

[6] L. Balka *et al.* (CDF Collaboration), "The CDF Central Electromagnetic Calorimeter", *Nucl. Instr. and Meth. A* **267** 272 (1988).

[7] R. Harris, "Measurement of η/π^0 from Isolated Decays into Two Photons", **CDF** internal note **1472**, (May 1991).

[8] CDF Collaboration, "A Time of Flight System for CDF", **CDF** internal note **2573**, (Feb 1994).

[9] H. Frisch *et al.*, "Conceptual Design of a Deadtimeless Trigger for the CDF Trigger Upgrade", **CDF** internal note **2038**, (Dec 1994).

[10] D. Amidei *et al.*, "A Two Level FASTBUS Based Trigger System for CDF", *Nucl. Instr. Meth. A* **269**, 51 (1988)

[11] F. Abe *et al.* (CDF Collaboration), "Evidence of Top Quark Production in $p\bar{p}$ Collisions at $\sqrt{s} = 1.8\ TeV$", *Phys. Rev. D* **50**, 2966 (1994)

[12] J. T. Carroll *et al.*, "The CDF Level 3 Trigger", *Nucl. Instr. Meth. A* **300**, 552 (1991)

Chapter 3

Analysis strategy and simulations

In this chapter the strategy adopted to measure the *branching ratio* of the process $B_s \to J/\psi\eta$ will be described. The estimation of the *branching ratio* can be obtained by means of the direct (absolute) measurement or the relative measurement. We here analyze the major sources of (systematic) uncertainties that the strategies introduce and we justify the choice of the relative measurement.

The simulations used for the estimation of the geometric acceptances and for the study of the reconstruction efficiencies will be described.

3.1 Analysis strategy

The relation between the *branching ratio* and the quantity subject to measurement, i.e. the number of reconstructed candidates, can be in general expressed by the following equations:

$$
\begin{aligned}
&a) N_{B_s}(TOT) = 2\int \mathcal{L}dt \cdot \sigma_b \cdot f_s \\
&b) N_{B_s}(J/\psi\ \eta) = N_{B_s}(TOT) \cdot \mathcal{B}(B_s \to J/\psi\eta) \cdot \mathcal{B}(J/\psi \to \mu\mu) \cdot \mathcal{B}(\eta \to \gamma\gamma) \\
&c) N_{B_s}(REC) = N_{B_s}(J/\psi\ \eta) \cdot \alpha_{\psi\eta} \cdot \epsilon_{\psi\eta}
\end{aligned}
\tag{3.1}
$$

The equation 3.1a provides the total number of B_s mesons generated during the whole CDF data taking, where we indicate with $\mathcal{L}$ the total integrated luminosity of the analyzed dataset, with σ_b the b quark production cross section in $\mathrm{p\overline{p}}$ collisions at an energy of 1.8 TeV in the center of mass, with f_s the fraction of b quarks that hadronize in a B_s meson; finally, the factor 2 takes in account that the B_s reconstruction does not distinguish between B_s and $\overline{B}_s$ mesons. In 3.1b with $N_{B_s}(J/\psi\ \eta)$ we indicate the number of B_s which decay to the channel we want to reconstruct. The number of reconstructed $B_s \to J/\psi\eta$ events is defined in equation 3.1c, where $\alpha_{\psi\eta}$ stands for the detector geometric acceptance and $\epsilon_{\psi\eta}$ for the reconstruction efficiency after all the requests for the particles in acceptance.

Rewriting the 3.1 as

$$
\mathcal{B}\left(B_s \to J/\psi\eta\right) = \frac{N_{B_s}(REC)\left(B_s \to J/\psi\eta\right)}{2 \cdot \int \mathcal{L}dt \cdot \sigma_b \cdot f_s \cdot \mathcal{B}\left(J/\psi \to \mu\mu\right) \cdot \mathcal{B}\left(\eta \to \gamma\gamma\right) \cdot \epsilon_{\psi\eta} \cdot \alpha_{\psi\eta}} \tag{3.2}
$$

Obviously the knowledge of all the terms on the right hand of the equation 3.2 leads to the measurement of $BR(B_s \to J/\psi\eta)$. This method is usually called “direct measurement”.

An alternative procedure, known as "relative measurement", consists in reconstructing in the same dataset a second channel, besides the one subject to search, which *branching ratio* $\mathcal{B}(B_X \to Y)$ is known. For this decay an equation similar to 3.2 can be rewritten; obviously terms like integrated luminosity, b quark production cross section are equal and can be factorized. It's so possible to write down an equation which connects the *branching ratio* of the channel under study and the known one:

$$\mathcal{B}(B_s \to J/\psi\eta) = \frac{N_{B_s}(REC)}{N_{B_X}(REC)} \cdot \frac{f_X}{f_s} \cdot \frac{\mathcal{B}(B_X \to Y)}{\mathcal{B}(J/\psi \to \mu\mu) \cdot \mathcal{B}(\eta \to \gamma\gamma)} \cdot \frac{\alpha_Y}{\alpha_{\psi\eta}} \cdot \frac{\epsilon_Y}{\epsilon_{\psi\eta}} \tag{3.3}$$

The equation 3.3 suggests to use as a reference a decay whose *branching ratio* is not only known with good precision but also is "similar" to $B_s \to J/\psi\eta$, meaning that the efficiencies and acceptances ($\frac{\epsilon_Y}{\epsilon_{\psi\eta}} \frac{\alpha_Y}{\alpha_{\psi\eta}}$) ratio be close to unity. In order to avoid the problems connected to the fragmentation fractions, $\frac{f_X}{f_s}$, a second decay channel of the B_s meson is a natural choice. Unfortunately there are not many decays of the B_s whose *branching ratio* is known with a good (enough) precision. A possible option is given by the $B_s \to J/\psi\phi$; this channel has been reconstructed at CDF, but his *branching ratio* is known with an error of $\sim 35\%$. Besides, and more subtle, the number of events reconstructed with selections similar to that used for $B_s \to J/\psi\eta$ is small and this will provide a substantial adjunctive statistic error. For these reasons we decided for the decay $B_u \to J/\psi K$ ($B^\pm \to J/\psi K^\pm$)[1]. Then the equation 3.3 becomes:

$$\mathcal{B}(B_s \to J/\psi\eta) = \frac{N_{B_s}(REC)}{N_{B_u}(REC)} \cdot \frac{f_u}{f_s} \cdot \frac{\mathcal{B}(B_u \to J/\psi K)}{BR(\eta \to \gamma\gamma)} \cdot \frac{\alpha_{\psi K}}{\alpha_{\psi\eta}} \cdot \frac{\epsilon_{\psi K}}{\epsilon_{\psi\eta}} \tag{3.4}$$

We want now to compare the two strategies for the *branching ratio* estimation, direct measurement (equation 3.2), or relative measurement (equation 3.4) considering the not common error sources present in the two cases.

The common terms $\mathcal{B}(J/\psi \to \mu\mu)$ and $\mathcal{B}(\eta \to \gamma\gamma)$ are present in both the relations 3.2 and 3.4, so are not considered in this list.

Direct Measurement

- The integrated luminosity $\int \mathcal{L}dt$ is known at CDF with a uncertainty of 4.1%;

- The direct measurement requires the knowledge of the B_s meson production cross section, σ_{B_s}; this term has been factorized in the equation 3.2 as $\sigma_b \cdot f_s$.
  The σ_{B_s} has not been measured at CDF, for this reason we adopted this factorization.

  The quantity σ_b cannot be measured directly, it is extrapolated from b-hadron cross section measurements. Considering the CDF measurement of σ_{B_u} [1] for $P_T(B_u) > 6$ GeV/c and $|y| < 1$ and considering f_u [3] to be known, we can express the b quark production cross section with the relation $\sigma_b = \frac{\sigma_{B_u}}{f_u}$. So we can write $\sigma_{B_s} = \frac{\sigma_{B_u}}{f_u} \cdot f_s$. The fragmentation fraction $\frac{f_s}{f_u}$, which is present in the equation 3.4 of the relative measurement, finally appears also in the direct measurement. The method here adopted has made use of the direct measurement of the B_u production cross section in a well defined kinematic range, so not a total cross section. The advantages of this choice will be below clarified. The σ_{B_u} term is known with an uncertainty of 17%.

- The absolute efficiencies and acceptances $\epsilon_{\psi\eta}$ and $\alpha_{\psi\eta}$. The uncertainty on these terms will be compared with the one on the relative efficiencies and acceptances.

Relative measurement

- The number of reconstructed events in the reference channel. In chapter 6 will be shown how the choice of $B^{\pm} \rightarrow J/\psi K^{\pm}$ channel allows a uncertainty on the number of reconstructed events lower than 10%.

- The fragmentation fraction. As previously shown this is a common term present in both strategies.

- $\mathcal{B}(B_u \rightarrow J/\psi K)$. This quantity, measured at CDF too, is known with an error of 5% [4].

- The relative efficiencies and acceptances will be discussed just below.

In calculating the contribution of σ_b to the uncertainty on the absolute measurement we used the experimental measurement of σ_{B_u} evaluated for $P_T(B_u) > 6$ GeV/c and $|y| < 1$. The σ_b so obtained is not the b quark production cross section introduced in 3.2. This problem can be simply solved by formally redefining the terms $\epsilon_{\psi\eta}$ and $\alpha_{\psi\eta}$, also in equation 3.2, as the efficiency and acceptance for events containing b quarks with momentum and rapidity distribution so that they hadronize to B-mesons with $P_T > 6$ GeV/c and $|y| < 1$. In this way the transverse momentum and rapidity selections applied to the B-meson are reabsorbed in these terms.

The alternative option to use the total σ_b measurements has been discarded since these measures are based on extrapolation with theoretical models still evolving. Besides, these models have always shown a remarkable discrepancy with the CDF data and only recently [5] this discrepancy has been reduces, but not canceled.

Another important aspect worthy to evaluate is given by the fragmentation fractions. The world average, including CDF data, is dominated by the LEP results and is equal to $\frac{f_s}{f_u, f_d} = 0.232 \pm 0.031$, showing an error of 13% [2]. These measurement has been obtained imposing $f_u = f_d$, the further error due to this assumption is not easy to evaluate. The CDF measurement has been conducted in the same physical environment of the channel we are studying; this will guarantee that possible differences in fragmentations of B-mesons produced at LEP or at Tevatron will not affect. The choice of the $\frac{f_s}{f_u}$ value is a delicate step of the analysis and will be discussed in chapter 7. However, it has been shown as this factor is present in both the strategies, so it has no influence on the choice of the method to be adopted. There are still to discuss the uncertainties related to the relative and absolute efficiency and acceptance measurements. We can rewrite the efficiency term for the $B_s \rightarrow J/\psi\eta$ channel in a more precise way as:

$$\epsilon_{\psi\eta} = \epsilon_{Trigger} \cdot \epsilon_{\mu\mu} \cdot \epsilon_{\gamma\gamma} \cdot \epsilon_{other} \tag{3.5}$$

where the term $\epsilon_{Trigger}$ stands for the efficiency of the triggers forming the dataset, $\epsilon_{\mu\mu}$ and $\epsilon_{\gamma\gamma}$ stands for the reconstruction efficiencies for muon and photon pairs generates in the decay of the J/ψ and η respectively; finally the ϵ_{other} term resumes the efficiency of eventual further requests on the B_s candidate.

A similar equation can be written for the reference channel $B^{\pm} \to J/\psi K^{\pm}$.
After these definitions the term $\frac{\epsilon_{\psi K}}{\epsilon_{\psi\eta}}$ that appears in the equation 3.4 can be rewritten as:

$$\frac{\epsilon_{\psi K}}{\epsilon_{\psi\eta}} = \frac{\epsilon_{Trigger}(\psi K)}{\epsilon_{Trigger}(\psi\eta)} \cdot \frac{\epsilon_{\mu\mu}(\psi K)}{\epsilon_{\mu\mu}(\psi\eta)} \cdot \frac{\epsilon_K(\psi K)}{\epsilon_{\gamma\gamma}(\psi\eta)} \cdot \frac{\epsilon^{B_u}_{other}}{\epsilon^{B_s}_{other}}. \tag{3.6}$$

The two terms $\frac{\epsilon_{Trigger}(\psi K)}{\epsilon_{Trigger}(\psi\eta)}$ and $\frac{\epsilon_{\mu\mu}(\psi K)}{\epsilon_{\mu\mu}(\psi\eta)}$ are expected to be close to 1 since the kinematics of the two decays is very similar. The displacement from unity will be parametrized in a factor k discussed and evaluated in section 7.2.5. Besides, these fraction suggest that the uncertainties on the $\epsilon_{Trigger}$ and $\epsilon_{\mu\mu}$ will enter only as a second order correction in case of the relative measurement, while they appeared at first order in the absolute measurement.

In table 3.1 we resume the errors for the absolute and relative measurement, assuming the error due to the efficiencies and acceptances to be equal for the two methods. Even with this assumption it is evident that the relative measurement is affected by a lower uncertainty. In order to perform the relative measurement we will reconstruct the $B^{\pm} \to$

	Direct measurement	Relative measurement
cross section	17%	-
integrated luminosity	4.1%	-
# of B_u	-	10%
$\mathcal{B}(B_u \to J/\psi K)$	-	5%
Total	17.5%	11%

Table 3.1: *Uncertainties due to the relative and absolute measurement.*

$J/\psi K^{\pm}$ signal in the same *data set* used for the research of the $B_s \to J/\psi\eta$ decay.

The evaluation of the fractions $\frac{\epsilon_K(\psi K)}{\epsilon_{\gamma\gamma}(\psi\eta)}$ and $\frac{\epsilon^{B_u}_{other}}{\epsilon^{B_s}_{other}}$ is thus the main object of this analysis and will be obtained as much as possible using experimental data, on the other cases we will use the Monte Carlo simulation. Instead the ratio of the acceptance ratio $\frac{\alpha_{\psi K}}{\alpha_{\psi\eta}}$ will be evaluated only from the simulation.

3.2 B meson production and decay

The Monte Carlo dataset is used to determine the ratio of the acceptances of the two decay channels, to calculate some of the efficiencies that cannot be extracted from the data, to have a confirmation on the ones evaluated on data themselves, and to calibrate the signal selection in order to maximize the signal with respect to the noise.

The Monte Carlo data production, can be sketched as follow. The same reconstruction and selection process used on the experimental data has then been applied to these data.

- events generation: it is possible to use both a complete Monte Carlo which simulate the process $p\bar{p} \to b\bar{b}X$ at partonic level with, eventually, emission of initial or final state radiation, or a parametric Monte Carlo which produces only b quarks with kinematic properties defined by a selectable theoretical model. The CPU time necessary to generate a complete dataset with an integrated luminosity comparable to the experimental data is too long (only for the generation, so without the simulation, of 100 pb^{-1} more than 1 year of CPU time is necessary on a 1GHz processor), for this reason we decided to adopt the parametric Monte Carlo BGENERATOR to obtain an high statistics dataset of pure signal. However we generated also a smaller dataset of events with the complete Monte Carlo PYTHIA. The two generators and the datasets will be discussed on the next section.

- fragmentation: the b quarks hadronize to B mesons following the Peterson model described in 1.2.3. We adopted the value $\epsilon_b = 0.0063$. This is part of a wider choice of parameter for the Monte Carlo, optimized to reach a good agreement between data and simulation on the $B \to \nu\ell D^0$ decay, studied at CDF [9].

- decay of unstable particles: since we are interested on B mesons and decided to use the "QQ" [11] Monte Carlo written by the CLEO collaboration. This Monte Carlo contains a database with informations on masses, spins, mean lives, *branching ratio*, etc. of the particles. The particle properties relevant for this analysis have been updated to the values currently accepted in literature [3].

- detector simulation: the QFL software (see 3.3.3) handles the propagation and eventually the decay of the particles generated inside the CDF detector. The various interaction processes between particles and matter are simulated.

- trigger simulation: we used the package DIMUTG which reliably simulates the μ trigger in the CMU chambers (see section 3.3.3).

3.3 Simulations of the decays $B_s \to J/\psi\eta$ and $B_u \to J/\psi K$

3.3.1 BGENERATOR

The Monte Carlo BGENERATOR [6] has been used to generate two datasets of $B_s \to J/\psi\eta,\ J/\psi \to \mu\mu,\ \eta \to \gamma\gamma$ and $B_u \to J/\psi K,\ J/\psi \to \mu\mu$. A single b quark is generated in each event with a transverse momentum spectrum $P_T(b)$ based on a *next-to-leading order* (NLO) QCD calculation known as NDE [7]. We made use of the parton distribution function MRSD0 [8], at a renormalization scale $\mu = \mu_0 \equiv \sqrt{m_b^2 + P_T^2(b)}$ and with a b quark mass $m_b = 4.75$ GeV/c^2. BGENERATOR allows the generation of b quarks with selectable initial spectra; it is possible to choose among different parton distribution functions (MRSD0, MRSD-), b quark masses (4.50, 4.75, 5.00 GeV/c^2) and normalization scales ($\mu_0/4, \mu_0/2, \mu_0, 2\mu_0$) for a total of 9 different configurations. This Monte Carlo allows to generate a consistent dataset in a limited amount of time since the transverse momentum and rapidity distributions are defined by bidimensional histograms and don't need to be generated event-by-event. Furthermore, it is possible to adopt a custom input spectrum by means of a bidimensional histogram containing the $P_T - y$ desired relation.

The dataset has been initially generated without restrictions both in rapidity and minimum transverse momentum. A preliminary analysis of this dataset suggested to apply at generation level a rapidity cut of $|\mathrm{y}_b| < 1.5$ and a minimum quark transverse momentum cut of $P_T(b) > 4\,\mathrm{GeV/c}$; we required also that $P_T(\mu) > 1\,\mathrm{GeV/c}$ and $|\eta(\mu)| < 1.2$ for the two muons of the J/ψ decay; these requests exclude only the 1.8% of the events that would pass the minimum reconstruction kinematic selections or be included in the geometrical acceptance of the detector (see picture, 3.1, 3.2)[1], while the CPU time decreases of a factor $\sim 90\%$.

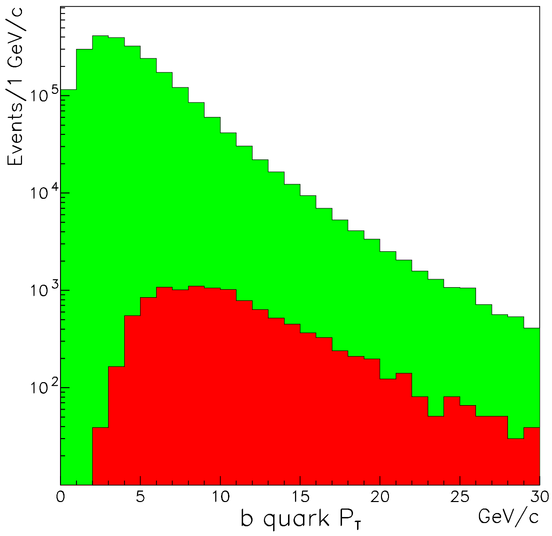

Figure 3.1: *Transverse momentum of the b quark before (light) and after (dark) the dimuon trigger simulation and the $P_T(\mu) > 2$ GeV/c cut.*

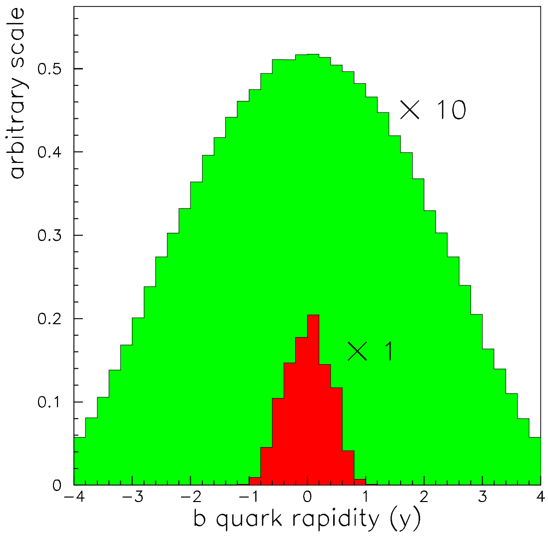

Figure 3.2: *b quark rapidity before (light) and after (dark) the dimuon trigger simulation and the $P_T(\mu) > 2$ GeV/c cut. The light plot has been reduced by a normalization factor equal to 10.*

b quarks then hadronize into B mesons using the Peterson fragmentation fraction; in figure 3.3 we show that with the adopted parameters the B meson carries about 80% of the quark transverse momentum.

3.3.2 PYTHIA generator

This Monte Carlo, developed by the Lund group [10], generates the complete $p\overline{p}$ to $b\bar{b}$ interaction, with the hadronization products, initial and final state radiation emission and the soft interaction between spectator quarks; we adopted the version PYTHIA 5.7/JETSET 7.4. Some of the configurations have been modified on order to obtain a better agreement between Monte Carlo and data; the Peterson parameter, the parton-parton interaction cross section, the description of soft quark interactions. The configuration adopted has been studied [9] in order to better agree with CDF data of $B \to \ell D^0 X$ decays.

In order to generate a statistically significant *data set* we decided to exclude all the B meson decays not containing a J/ψ. The starting point of the analysis is in fact the reconstruction of the pair of μ coming from this particle; for this reason in each event we imposed to one of the generated B meson[2] to decay to a channel containing a J/ψ, by means of the selection only of the channels: $B \to J/\psi_{direct} + X$, $B \to \psi(2S) + X$,

[1] After all the requests no event is reconstructed outside these intervals.

[2] In the case only B barions are present in the event, these are not forced.

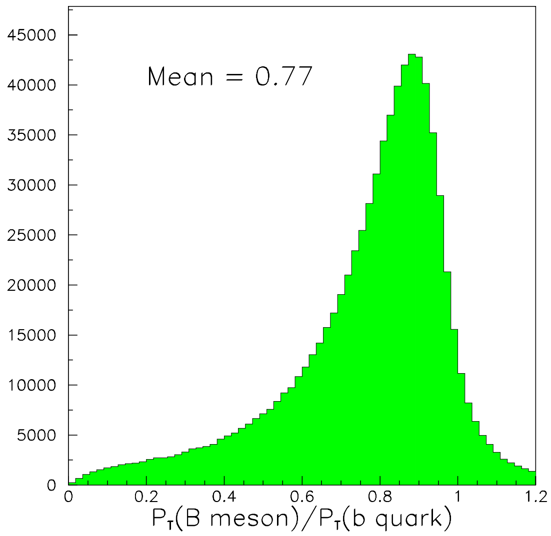

Figure 3.3: *$P_T(B)/P_T(b)$ ratio.*

$B \to \chi_c + X$; furthermore we forced the decay $J/\psi \to \mu\mu$. The channels so excluded from generation would not have entered anyway in the event reconstruction chain since the trigger simulation (see section 3.3.3) discards the events without a J/ψ candidate. These requests allowed to generate a significant dataset of events, ~ 550 pb^{-1} (assuming $\sigma_{b\bar{b}} = 100\mu b$). In this simulation we adopted a $\mathcal{B}(B_s \to J/\psi\eta) = 5 \cdot 10^{-4}$.
The data produced with this Monte Carlo will be used to evaluate the combinatorial effects and verify the capacity of the reconstruction algorithm to show a signal in a dataset of events with a good background simulation (of B hadrons) and with a statistics 6 times higher than the real data.

3.3.3 Detector and trigger simulation

The detector simulator: QFL

The CDF detector simulation is assigned to a Monte Carlo program using a parametric model of the detector answer to passage of particles, model optimized by the comparison with test-beam data or collected at CDF. QFL is a "high level" simulator, meaning that it does not produce the single interactions between particles and the various parts of the detector, on the contrary it creates directly the structures of data that will be used for the analysis.
In the simulation the charged particles crossing the detector undergo energy loss due to ionization and are deflected by multiple Coulomb scattering in crossing material; the energy lost by *bremsstrahlung* has been taken in account in case of incident electrons on matter; finally is also simulated the e^+e^- pair production from incoming photons. All these processes are based on a simplified model of the detector geometry and of the material distribution. The efficiencies of the individual wire layers have been determined from data; also the simulation does not execute a pattern recognition algorithm on the released hits, but generates directly the helix parameters with the typical chamber resolution. For the particle crossing SVX and/or the muon chambers, single hits are generated in order to simulate the detector resolution and take in account the Coulomb scattering effects. Fi-

nally, the calorimetric response has been parametrized from data collected during electron test beams.

The trigger simulation: DIMUTG

The DIMUTG package (DIMUon TriGger) [12] implements the trigger simulation of μ pairs starting from the informations on tracks reconstructed on CTC and on μ chambers. For each μ chamber crossed by a muon track, the program reads the experimental efficiency curve from a database and with a Monte Carlo technique decides which triggers fire in that event. Figure shows 3.4 the level 1 trigger efficiency (see section 2.7.2) averaged over the whole Run1b for the CMU chambers[3], as a function of the μ transverse momentum. The Coulomb multiple scattering limits the precision of the transverse momentum and allows also to μ with a $P_T(\mu) < 3.3$ GeV/c to make the trigger to fire, down to values of $P_T(\mu) \sim 1.4$ GeV/c, under which the muons do not even reach the CMU chambers.

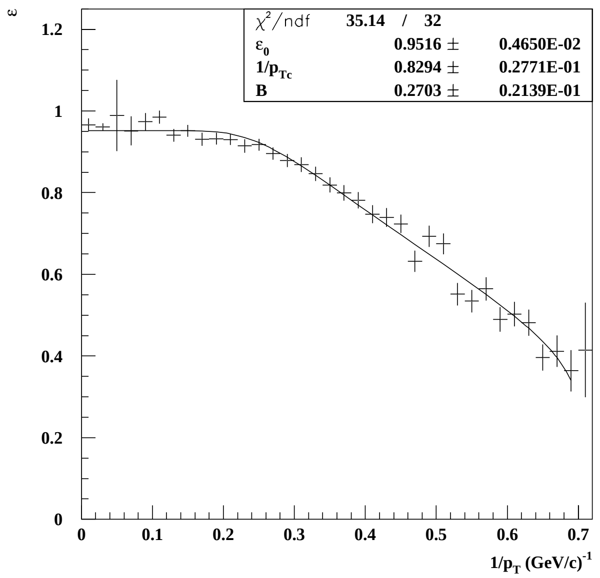

Figure 3.4: *Level 1 efficiency of CMU chambers. The μ dataset used for the measurement is the $J/\psi \to \mu\mu$ dataset, where one of the two muons fired a high P_T single muon trigger.*

The level 2 efficiency (see section 2.7.2) depends not only on the μ transverse momentum, but also on his charge, on the pseudorapidity, on the azimuthal angle and on the *aging* of the central chamber. Figure 3.6 shows the level 2 trigger efficiency as a function of the μ transverse momentum. Figure 3.6 points out the degradation of the plateau efficiency *versus* the integrated luminosity (which means the *aging*) for positive and negative muons.

The level 3 trigger has an overall efficiency equal to 0.97 ± 0.02, not dependent on P_T. For this reason it is not simulated, but it will be considered only in a global efficiency factor.

[3] As will explained in section 4.1, in this analysis we use only data collected by CMU chamber triggers.

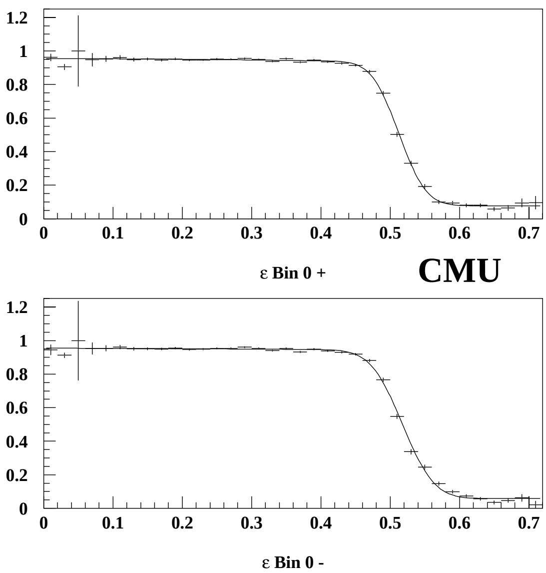

Figure 3.5: *Level 2 trigger in CMU chambers as a function of the variable $1/P_T$ in $(GeV/c)^{-1}$ for μ^+ (upper) and μ^- (lower).*

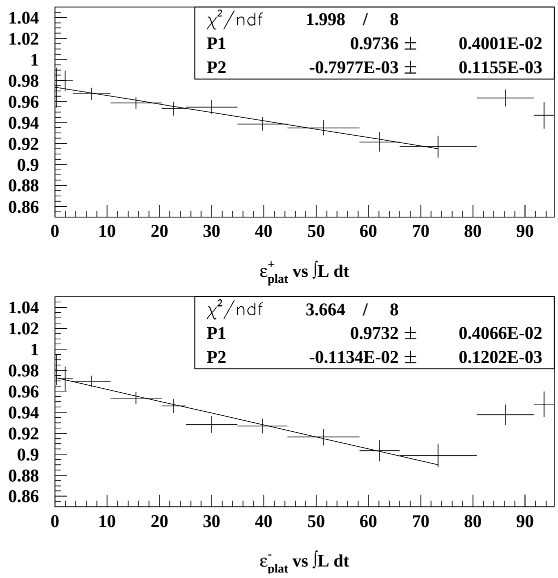

Figure 3.6: *Plateau efficiency degradation on CMU chambers as a function of integrated luminosity for μ^+ (upper) and μ^- (lower). After $\sim 80\ pb^{-1}$ it has been changed the pattern recognition algorithm on CTC.*

Bibliography

[1] D. Acosta *et al.* (CDF Collaboration), "Measurement of the B^+ Total Cross Section and B^+ Differential Cross Section $d\sigma/dp_T$ in $p\overline{p}$ Collisions at $\sqrt{s} = 1.8$ TeV", *Phys. Rev. D* **65**, 052005 (2002)

T. A. Keaffaber, M. W. Bailey, D. Bortoletto, A. F. Garfinkel, A. T. Laasanen, J. D. Lewis, S. Tkaczyk, "Measurement of the B^+ Total Cross Section and B^+ Differential Cross Section $d\sigma/dp_T$ in $p\overline{p}$ Collisions at $\sqrt{s} = 1.8$ TeV", **CDF** internal note **5608**, (Jun 2001)
See also:
CDF internal note **3634**, (Apr 1996)
CDF internal note **2892**, (Nov 1994)
CDF internal note **2516**, (Mar 1994)

[2] "31st International Conference on High Energy Physics, ICHEP02, Amsterdam (The Netherlands)", July 24-31, 2002
see also:
ALEPH, CDF, DELPHI, L3, OPAL, SLD, "Combined results on b-hadron production rates and decay properties", CERN-EP/2001-050, Jun 2001

[3] T. Affolder *et al.* (CDF Collaboration), "Measurement of b-Quark Fragmentation Fractions in $p\overline{p}$ Collisions at $\sqrt{s} = 1.8$ TeV", *Phys. Rev. Lett.* **84**, 1663 (2000)

[4] K. Hagiwara *et al.*, "Review of Particle Physics", *Phys. Rev. D* **66**, 010001 (2002)

[5] P. Nason *hep-ph/0207362*
Pres. at: 6th International Workshop on Heavy Quarks and Leptons, Vietri sul Mare, Salerno, Italy, 27 May - 1 Jun 2002

[6] P. Spichas, "A $b\bar{b}$ Monte Carlo Generator", **CDF** internal note **2655**, (Jun 1994)

[7] P. Nason, S. Dawson and R.K. Ellis, "The one particle inclusive differential cross section for heavy quark production in hadronic collisions", *Nucl. Phys. B* **327**, 49 (1990)

[8] A. D. Martin, W. J. Stirling, R. G. Roberts, "New Information on Parton Distributions", *Phys. Rev. D* **47**, (1993)

[9] F.Abe *et al.* (CDF Collaboration), "Measurement of the $B_d^0 - \overline{B}_d^0$ Flavor Oscillation Frequency and Study of Same Side Flavor Tagging of B mesons in $p\overline{p}$ Collisions", *Phys. Rev. D* **59**, 032001 (1999)
FERMILAB-PUB-98/188-E.

see also:
P. Spichas,D. Vucinic, "On Using Pythia to Model the Underlying Event in B and W Events", **CDF** internal note **4097**, (Mar 1998)

[10] Torbjorn Sjostrand, "PYTHIA 5.7 AND JETSET 7.4: Physics and Manual", LU-TP-95-20, CERN-TH-7112-93-REV, hep-ph/9508391, (Aug 1995)

[11] P. Avery, K. Read, G. Trahern, "QQ: A Monte Carlo Generator", Internal Software Note **CSN-212**, (1985)
J. Lewis, P. Avery, "CLEOMC: The CDF Interface to the CLEO Monte Carlo (QQ)", **CDF** internal note **2724**, (Jul 1994).

[12] S. Pappas, "DIMUTG: A Dimuon Trigger Simulation for Run 1B", **CDF** internal note **3537**, (Feb 1996).

Chapter 4

J/ψ dataset selection

The dataset selection for the search of $B_s \to J/\psi\eta$ candidates is deeply based on the reconstruction of the J/ψ in its double muon decay. This decay provides a signature easy to trigger on, for the peculiarity of the signals released on the detector; besides, it allows detailed studies on the dataset composition and the improving of the signal extraction.

4.1 Experimental dataset

During the years 1992-1995 Tevatron accelerator produced proton-antiproton collision at a central mass energy equal to $\sqrt{s} \sim 1.8$ TeV; this period of data taking, called Run 1, includes two different periods of data acquisition: Run 1a (August 1992 - May 1993) and Run 1b (January 1994 - July 1995). During the Run 1 the detector underwent many upgrades, i.e. the microvertex detector has been substituted, the trigger and the data acquisition systems have been modified. The data collected during Run 1a correspond to a time integrated luminosity equal to $\int \mathcal{L}dt = (19.5 \pm 1.0)\mathrm{pb}^{-1}$, while the Run 1b data correspond to $\int \mathcal{L}dt = (89 \pm 4)\mathrm{pb}^{-1}$.
The various modifications brought to the detector and to the trigger impose that the data collected during the two periods must be treated as two inhomogeneous dataset. For this reason we decided to use for this analysis only the data collected during Run 1b.

Trigger

Among a total of 7 level 1 triggers selecting μ candidates events, only two are relevant for the collection of the J/ψ dataset used in this study. The first one (TWO CMU 3PT3) requires two *stubs* to be reconstructed in the CMU detectors, this trigger fired in the 68% of the collected data. The second one (TWO CMU CMX 3PT3) requires two *stubs*, one on the CMU modules, one on the CMU or CMX; this trigger fired in the 92% of the events.

The total list of level 2 triggers that form the dataset is really longer. In figure 4.1 we present the 7 muons trigger that mostly contribute.

It is useful here to remind that the adopted analysis strategy for the calculation of the *branching ratio* is based on the comparison with the $B^\pm \to J/\psi K^\pm$ channel studied by Keaffaber *et al.*[2]. In that study the authors restricted the analyzed Run 1b dataset to

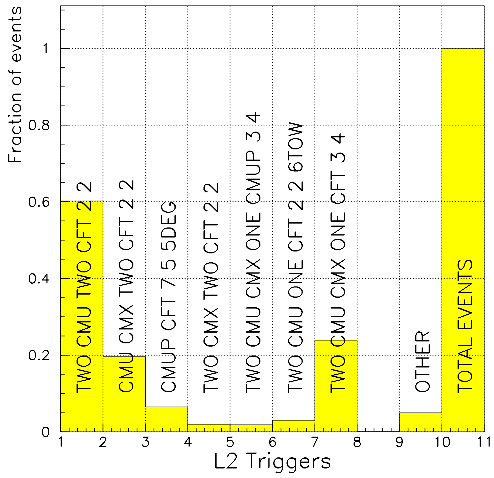

Figure 4.1: *Level 2 muon trigger. Six of them are 2 μ triggers; one, CMUP CFT 7 5 5DEG, is a single μ trigger.*

only three triggers: TWO CMU TWO CFT 2 2, TWO CMU CMX ONE CFT 3 4 e TWO CMU ONE CFT 6TOW. This choice finds its motivation on the two-muon trigger simulation, which is sufficiently reliable only for pairs of muons hitting the CMU chambers; triggers accepting also signals in other chambers have then been discarded[1]. So the same requests have been applied to the muons reconstructed in this analysis; the uniformity of these requests in both channels will guarantee an easier comparison in extracting the *branching ratio*. This choice reduces of 28% the selected dataset.
The first of the two triggers requires one *stub* in the CMU chambers and a second one in the CMU or CMX; for the events collected with this trigger we impose the two muons to be both in CMU chambers. This is a prescaled trigger[2].
The third level still requires two clusters in the CMU and that the highest P_T muon to have released signal at least in 6 calorimetric trigger towers (see section 2.7.2). This trigger is aimed at recovering the loss of efficiency of dimuon triggers when the azimuthal separation of the two μ is small and the clusters are merged in one.

At level 3 the events are saved to disk mainly by the PSIB DIMUON JPSI trigger, described in section 2.7.2, which fired in 99.7% of the collected data.

4.2 Muons identification

The muon search begins looking for track segments, *stubs*, reconstructed on the μ chambers. These segments are associated to tracks reconstructed on the CTC. The association procedure compares, during the data production (offline), the track segment positions of the muons in the chambers with the positions expected there as calculated by extrapolating each track reconstructed on CTC. In order to decide the goodness of an association

[1]The trigger CMU CMX TWO CFT 2 2 requires one of the two muons to be in the CMX chambers, while the single muon trigger CMUP CFT 7 5 5DEG requires the detection also in the CMP chamber, as the TWO CMU CMX ONE CMUP 3 4 does; finally the trigger TWO CMX TWO CFT requires both muons on CMX.

[2]In order to reduce the acquisition frequency, only to one event every N (prescaling factor) is sent to the level 3 trigger.

between a track and a *stub* we calculate a χ^2 defined as the square of the distance between the extrapolated track and the segment on the μ chambers, divided by the square of the position error, evaluated considering the material distribution between the CTC and the chambers. These requests are applied for (CMU, CMX, CMP) chambers both in $r-\phi$ and z views. The applied requests, $\chi^2_{r-\phi} < 9$ and $\chi^2_z < 12$, corresponds approximatively to cut at 3 standard deviations in $r-\phi$ view and $\sim 3.5\sigma$ in z view.
These requests want to reduce the background on the μ signal, background constituted mainly by two components. The first one is formed by $K^\pm$ or $\pi^\pm$ decaying to muons revealed in the μ chambers; the second one is given by hadronic particles passing through the calorimeters and entering the μ detection system (*punch-through*).

On the muons so reconstructed, and more generally on all the tracks, we apply quality cuts consisting in requiring the track to be reconstructed at least in 2 *superlayers* of the CTC (see section 2.3.3) per view, with at least 4 hits per *superlayer* in $r-\phi$ view and 4 hits per *superlayer* in z view; besides, the reconstructed helicoidal tracks are extrapolated to the SVX detector and a *road* algorithm associates the hits recorded on silicon. If a sufficient number of quality SVX hits has been identified and associated, the track undergoes a further interpolation making use of all the informations available from the CTC, VTX, SVX detectors. The recalculated helix parameters are the track parameters.

At this level we advance no requests on the minimum muons P_T, even if a minimum transverse momentum of 1.4 GeV/c is necessary for the muons in order to reach (at pseudorapidity $\eta \sim 0$) the CMU chambers and the trigger to fire. Figure 4.2 shows this threshold effect on the μ identified by the criteria just described which invariant mass satisfies $|M_{\mu\mu} - M_{J/\psi}| < 30$ MeV/c^2. This last request has the only aim to select a dataset enriched on muons and will not be used for the rest of the analysis.

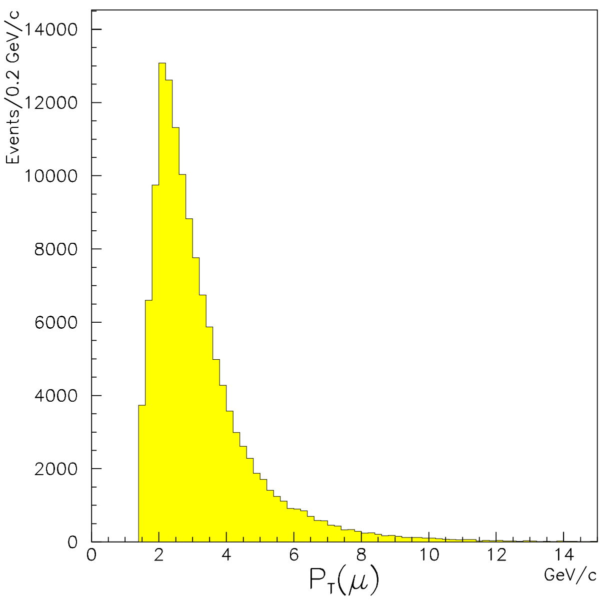

Figure 4.2: *P_T muon spectrum after the χ^2 selections and the quality cuts on tracks and for $|M_{\mu\mu} - M_{J/\psi}(PDG)| < 30$ MeV/c^2.*

4.3 J/ψ reconstruction

After the identification of the muons in the event we consider all the pairs of opposite charge for which $|z_0(\mu_1) - z_0(\mu_2)| = |\Delta z_0| < 5$ cm, where with z_0 we indicate the z coordinate of the point of closest approach of the track to the z axis of the detector. This request want to exclude the muon pairs not originated on a common vertex. Figure 4.3 shows the distribution of the variable Δz_0 for muon pairs satisfying $|M_{\mu\mu} - M_{J/\psi}(PDG)| < 30$ MeV/c^2. On the pairs selected we apply a vertex constrained fit algorithm[3]. Forcing the

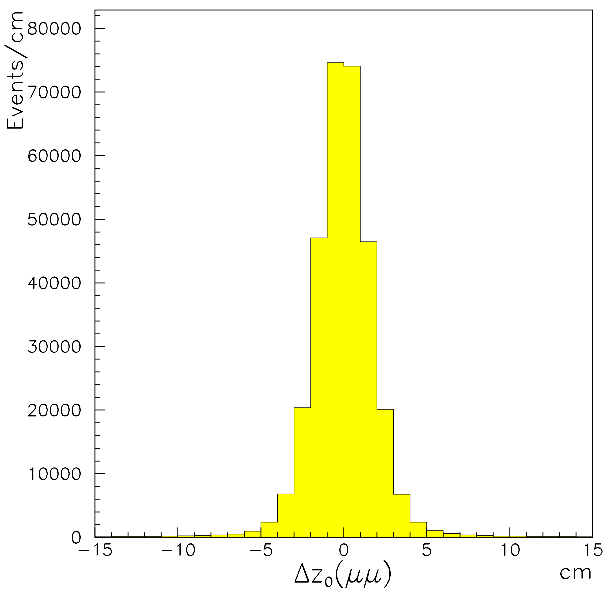

Figure 4.3: Δz_0 *for muon pairs satisfying also* $|M_{\mu\mu} - M_{J/\psi}(PDG)| < 30$ MeV/c^2.

two muons to have a common originating vertex provide a supplementary information not present in the single track extrapolations; imposing such a constraint improves of a factor 1.6 the $M_{\mu\mu}$ invariant mass distribution width. Furthermore the fit calculates the covariance matrix for the new variables which describe this system, X_V, Y_V, Z_V, $p_x^{\mu 1}, p_y^{\mu 1}, p_z^{\mu 1}$, $p_x^{\mu 2}, p_y^{\mu 2}, p_z^{\mu 2}$, variables that will be reconsidered in chapter 6. This procedure allows also to define the *secondary vertex* position for the event. The mean life of the J/ψ ($\Gamma = 87KeV$) in fact is so small that we can neglect the flight distance and then, in the case it is coming from a B decay, assume the double μ vertex as coincident with the B decay vertex itself.

Figure 4.4 shows the invariant mass distribution for all muon pairs after the χ^2 and Δz_0 cuts before and after the *vertex constrained* fit. The mass resolution depends on the momentum resolution of the tracks, which in his turn depends on the momentum itself; besides, this distribution is calculated using track parameters evaluated with or without SVX informations, so with potentially different errors. The distribution can then be thought as a superposition of gaussians over a linear background; we decided to fit the J/ψ signal with two gaussians which means are forced to be equals. The total width is

[3]The packaged used (`CTVMFT`) is a CDF standard code where various kinematic fit algorithms are implemented; in the prosecution of this analysis we will further make use of it.

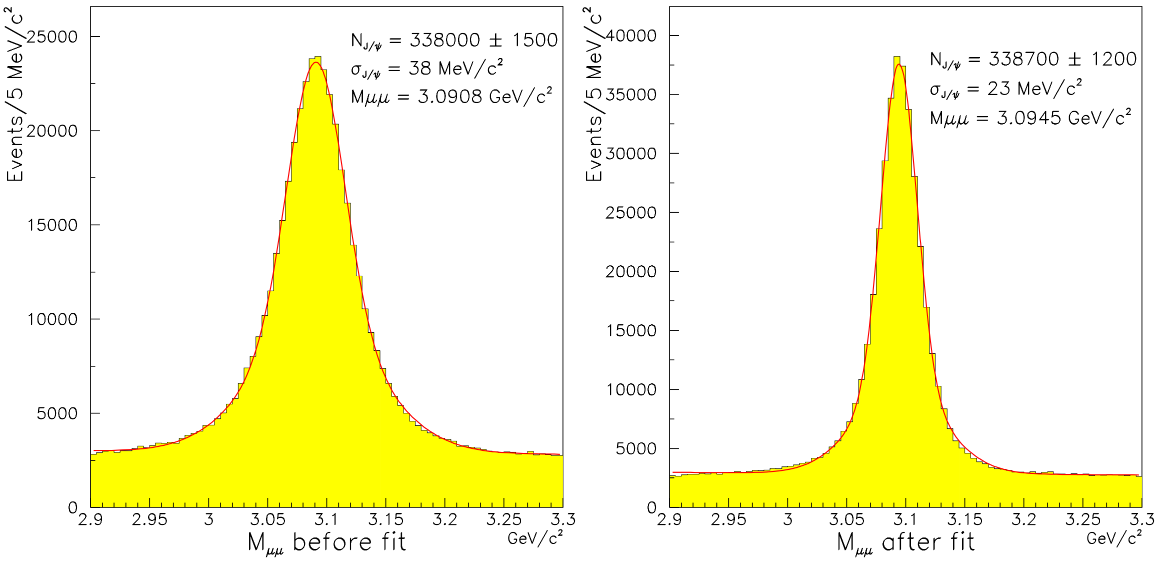

Figure 4.4: *Invariant mass distribution for all the pairs $\mu\mu$ of opposite charge. The plots show the invariant mass calculated with the two tracks before (left) and after (right) the* vertex constrained *fit. The interpolating function used is a double gaussian for the signal and a linear function for the background. The quoted width is the weighted average sigma.*

calculated as the weighted average of the two distribution width. Events with at least one pair of μ and invariant mass included between 2.9 and 3.3 GeV/c^2 are selected for the further steps of the analysis.

4.3.1 Background estimation and *sidebands*

Figure 4.4 suggests to discuss a background estimation technique and then define a useful tool for the rest of the analysis. The estimates on the number of J/ψ candidates shown in figure 4.4 imply the hypothesis that the background behavior can be correctly described by a fit (in this case a linear fit) so that we can reliably distinguish the two contributions coming from the non resonant continuum and from the signal. In these situations, when the background is supposed to be under control, it's useful to define regions of the mass spectrum known as *sidebands*. In figure 4.5 we show again the invariant mass plot after the fit and we highlight two regions: the central one is the signal and in this case is selected by $|M_{\mu\mu} - M_{J/\psi}| < 2\sigma_{M_{\mu\mu}}$, the lateral regions are at a "distance" of $5\sigma_{M_{\mu\mu}}$ from the nominal J/ψ mass (which we have seen to be almost coincident with the one here measured) and have an amplitude of $2\sigma_{M_{\mu\mu}}$ too, so are selected by $5\sigma_{M_{\mu\mu}} < |M_{\mu\mu} - M_{J/\psi}| < 7\sigma_{M_{\mu\mu}}$. After these requests we selected two sub-datasets which are supposed to contain the same number of background events. The usefulness of this situation is immediately evident. Let's suppose for example we want to study the behavior of a variable, i.e. the transverse momentum of J/ψ. A plot obtained from the events on the signal region contains contributions from two populations, the signal and the background. Generally speaking, the presence of background deforms the spectrum shape we are studying. Having a dataset of "pure background", obtained with the same selections of the signal and with the same statistics of the expected background allow to decouple the background contribution by means of a simple histogram operation. The first histogram is filled with "signal" events,

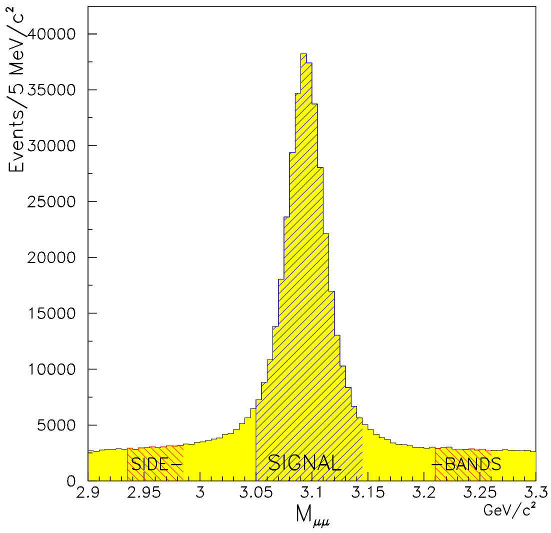

Figure 4.5: *Invariant mass spectrum $M_{\mu\mu}$, selection of the signal and* sidebands *regions.*

a second one with "sidebands" events, the third one with the difference between the two. The spectrum deformation of the first histogram due to background contamination is statistically canceled in this operation and the final spectrum is closer to the pure signal one. This method is know as *sidebands subtraction* procedure. Figure 4.6 shows an example of this procedure.

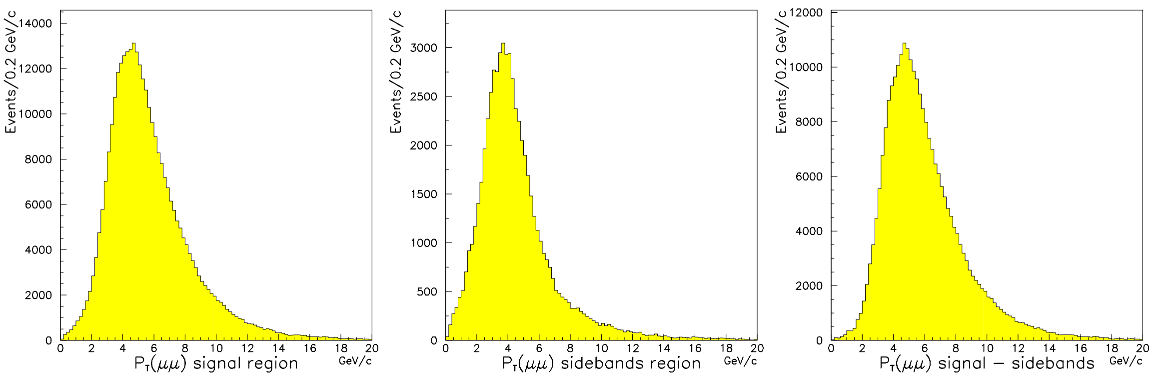

Figure 4.6: *J/ψ transverse momentum. The plot at left contains the events in the central region of the $M_{\mu\mu}$ distribution, the central plot contains the events on the sidebands, the third one the difference between the two.*

μ in SVX

We have pointed out before that the μ identification and reconstruction algorithms are based on the data collected in VTX, CTC, μ chambers and SVX when available. This allow us to reconstruct a J/ψ signal with an average resolution of ~ 23 MeV/c^2 (figure 4.4). The sensibility on the measurement of the transverse momentum depends on the radial amplitude of the detector used for the measurement; the variance on the curvature scales with $1/nL^4$, where n is the number of measured points and L is the length of the reconstructed helix arc.[4] Among the tracks reconstructed as muons there is a subset for which also the informations coming from the microvertex detector have been used; the introduction of these further points on tracks increase the μ transverse momentum resolution and as a consequence also the invariant mass $M_{\mu\mu}$ resolution. We decided to label as SVX muons the tracks with at least three silicon hits associated to the track itself. Moving from this definition we defined a dimuon subset with both the tracks on SVX. The invariant mass spectrum for this set (figure 4.7) shows an evident increase of resolution ($\sim$ 30%). This notable result involves a reduction of the dataset to $\sim$ 55%; reduction

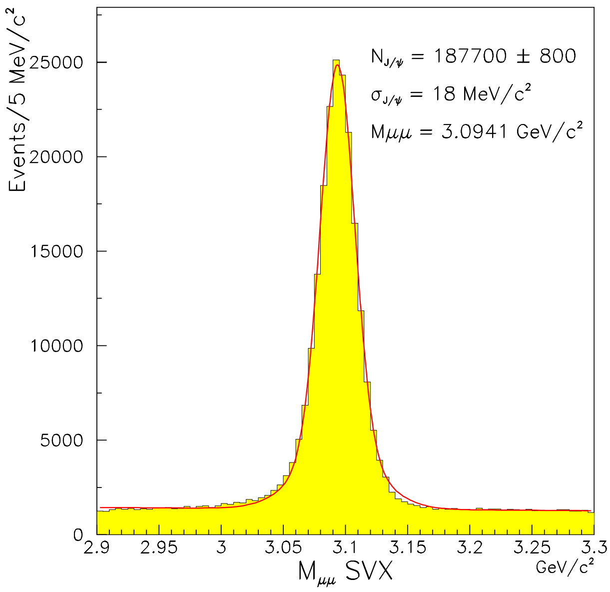

Figure 4.7: *Invariant mass spectrum $M_{\mu\mu}$ for μ in SVX.*

dues mainly to the limited geometric acceptance in z of the microvertex detector. In fact the CTC covers the region -160 cm $<$ z $<$ 160 cm, the VTX -132 cm $<$ z $<$ 132 cm, while the SVX detector limits to -25 cm $<$ z $<$ 25 cm.[5]

The reasons to use the microvertex detector in B physics are of course others and are related to the long mean lives of "beauty" hadrons ($\gtrsim$ 1 ps). This fundamental aspect will be discussed in the following section.

4.4 J/ψ decay length

The peculiarity of the decays involving B mesons is to present secondary vertexes displaced with respect to the primary vertex; the exact knowledge of the position of these vertexes allows to discriminate between particles produced by primary interaction or as a consequence of B meson decays.

[4]This is true when the points are equally spaced along a distance L and in absence of multiple scattering effects.

[5]It is worthwhile to remind that the interaction region at CDF is quite extended in z direction and can be described by a gaussian probability density function $P(z)$ with a $\sigma \sim 30$ cm.

4.4.1 Primary vertex

z position of primary vertex

During the Run Ib data acquisition the average instantaneous luminosity was $\mathcal{L} = 8.0 \times 10^{30}$ cm^{-2}s^{-1}, with peak values of $\mathcal{L} = 2.6 \times 10^{31}$ cm^{-2}s^{-1}. In these situations the multiple interactions per bunch crossing causes to have an average of ~ 2.9 high quality vertexes[6] and in $\sim 5\%$ of the events at least 8 of such vertices. In order to select the J/ψ originating vertex we select, among them, the one whose z coordinate is the closer to the average $(z_0(\mu_1) + z_0(\mu_2))/2$ of z_0 of the two muons; the uncertainty on this determination comes out to be in average equal to $\sigma_z = 2$ mm, as written in [2]. In order to calculate the vertex global position we assume as z coordinate the one of the vertex just identified and then we make use of the informations on the beam line position present in a database, filled run by run, for the calculation of the remaining two coordinate: the database provides the functions $x(z) = x_0 + a_x \cdot z$ and $y(z) = y_0 + a_y \cdot z$ for each run.

Beam line

For this reason the knowledge of the beam line position is important in order to be able to reconstruct the global coordinates of the primary vertex. This reckoning is carried out for each run and allows to evaluate also the small beam position variations in a single run. Nevertheless these variations do not limit the precision in the vertex position reconstruction. In fact it is useful to remind that the beam section is approximatively circular and that the particles are distributed with a gaussian probability density in the two directions x e y and with a width $\sim 25\mu$m. These dimensions set the limit to the resolution in the transverse plane for the primary vertex.

4.4.2 Decay length L_{xy}

Once the positions of the J/ψ primary and secondary vertexes are known[7] we can proceed with the calculus of the distance between these two points $\vec{L} = \vec{X}_{SecVertex} - \vec{X}_{PrimVertex}$. The presence of the microvertex detector allows to reconstruct accurately the transverse components of these quantities; since it cannot give any contribution to the resolution in z direction, we considered only the projection of the decay length in the transverse plane, L_{xy}.

In figure 4.8 we show the distributions of this quantity in the dimuon dataset reconstructed on data and on the Monte Carlo generated with BGENERATOR ($B_s \rightarrow J/\psi\eta$). Since in a collider experiment as CDF around 80% of the detected J/ψs originate from primary interactions (J/ψ *prompt*), the measure of L_{xy} or related quantities provides an efficient tool to reject background.

[6] We define as *low* quality vertexes the ones showing a limited number of reconstructed segments pointing to the vertex itself.

[7] See section 4.3.

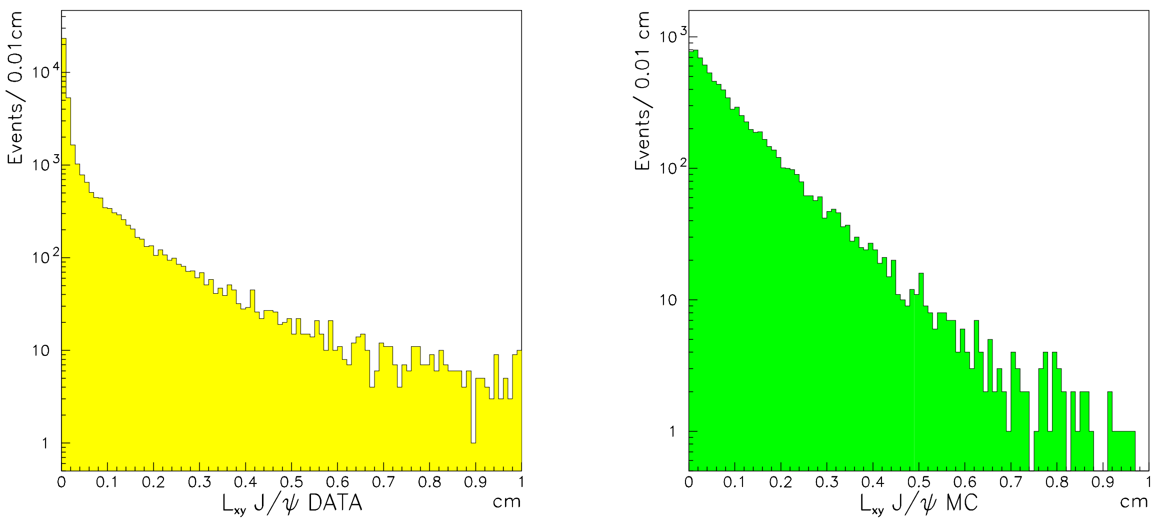

Figure 4.8: *L_{xy} distribution for data and Monte Carlo. This variable, or related quantities, appears to be an efficient tool to discriminate between* prompt *J/ψ and signal.*

Bibliography

[1] D. Acosta *et al.* (CDF Collaboration), "Measurement of the B^+ Total Cross Section and B^+ Differential Cross Section $d\sigma/dp_T$ in $\mathrm{p\overline{p}}$ Collisions at $\sqrt{s} = 1.8$ TeV", *Phys. Rev. D* **65**, 052005 (2002)
T. A. Keaffaber, M. W. Bailey, D. Bortoletto, A. F. Garfinkel, A. T. Laasanen, J. D. Lewis, S. Tkaczyk, "Measurement of the B^+ Total Cross Section and B^+ Differential Cross Section $d\sigma/dp_T$ in $\mathrm{p\overline{p}}$ Collisions at $\sqrt{s} = 1.8$ TeV",
CDF internal note **5608**, (Jun 2001)
See also:
CDF internal note **3634**, (Apr 1996)
CDF internal note **2892**, (Nov 1994)
CDF internal note **2516**, (Mar 1994)

[2] M. Paulini, "B lifetimes, mixing and CP violation at CDF". *Int. J. Mod. Phys. A*, **10**, 1990 (1999) hep-ex/9903002.

[3] H. Wenzel, "Fitting the beam position with the SVX", **CDF** internal note **1924**, (Jan 1993)

Chapter 5

η reconstruction

In order to reconstruct the $B_s \to J/\psi\eta$ decays we still have to detect the ηs by means of their two photons decays. The CDF detector is equipped with a calorimeter designed to detect high energy ($E \gtrsim 10$ GeV) photons and electrons, as can be the electrons originating from the vector bosons decays, or for the measurement of the energy of the electromagnetic component of the jets.

Since we want to use photons signatures for low P_T B physics we cannot avoid to extend the identification and energy measurement to lower impulse ranges. This will involve as a consequence a reduction in energy resolution ($\approx 13.5\%/\sqrt{E_T}$, see section 2.5) due to the reduced development of the electromagnetic shower. For the low energy photons and electrons characterization the CES proportional chambers are fundamental (see section 2.5.1), placed inside the calorimetric towers at a depth of 5.9 X_0 from the beam line. These detectors allow to precisely measure the position of the shower inside the tower at the point of maximum energy release. Using the test beam data CDF collaboration have developed algorithms able to characterize the transverse profile of electrons and photons in order to have a tool to distinguish these particles from other interaction products. Nevertheless we have to point out that these studies have been carried out on electrons of energies higher than 5 GeV [1] and it is not obvious to extend these algorithms to study to the photons we want to reconstruct, whose spectrum energy shows a peak at a value $\lesssim 1$ GeV, as presented in figure 5.1 (Monte Carlo BGENERATOR).

For this reason we decided not to use these algorithms based on the transverse profile comparison and we lowered the thresholds for the requests on the CES chambers. The photon identification and the subsequent η reconstruction then represents the more delicate aspect of the B_s meson search.

5.1 Photon identification

Energy release

The simulation of the $B_s \to J/\psi\eta$ event carried out with the Monte Carlo BGENERATOR shows that the 4 reconstructed bodies are included in the J/ψ hemisphere almost in the totality of the events ($\sim$ 99.9%). The figure 5.2 shows the opening angle between the flight direction of the J/ψ and the one of the photons. This plot has been obtained after a complete detector and trigger simulation and after the application of the reconstruction

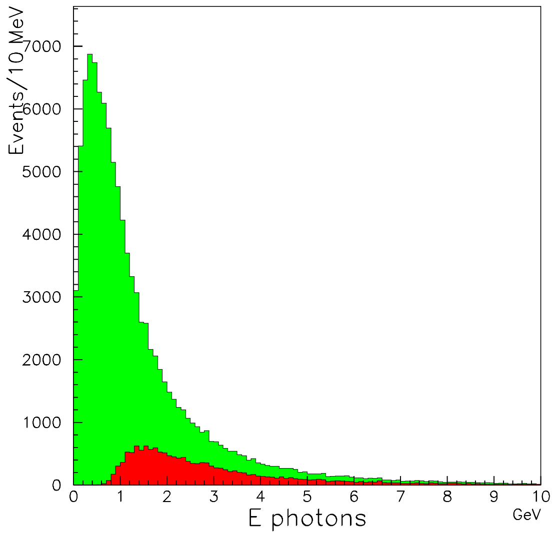

Figure 5.1: *Photon energy as read on OBSP bank, which means before the simulation and reconstruction. The light (green) distribution include all the photons, while the dark (red) distribution shows only the photons that will be able to pass an energy cut at 1 GeV. All the reconstruction requests have been applied on the μs.*

algorithm to the pair of generated muons (see previous chapter). The informations on the photon directions have been collected directly from the generator banks. The search of a photon signal is so restricted to the hemisphere containing the J/ψ. For the towers that record a $E > E_{thr} = 0.5$ GeV we require that no track reconstructed on CTC points to the towers themselves: if this request is not satisfied the tower is discarded. This request is unavoidable and is applied to reduce the hadron background (i.e. due to the process of *charge exchange* or to overlapped $\pi^{\pm}\pi^{0}$); the price to pay is a limitation on the geometrical acceptance to the pseudorapidity range $|\eta| < 1$, that corresponds to the region of full tracking efficiency. Besides, we decided to discard the last tower ring of the central calorimeter since it has shown an energy resolution really lower than the rest of the central calorimeter. This behavior is due mainly to its limited longitudinal hermeticity due to the presence of the hadronic calorimeter EWH (see figure 2.2).

CES chambers

On the selected towers we then readout the informations on the CES chambers; we look for wires of the *half-wedge* (see section 2.5.1) and strips of the tower with a signal higher than 0.2 GeV (*seed*) and on both sides of these channels we build clusters of variable width up to a maximum of 11 channels (5 on the right, 5 on the left) keeping only the ones exceeding a 0.1 GeV threshold. The position of the cluster is given by the centroid position evaluated for the channels over threshold. The sum of the measured energies on the wires (or strips) just selected defines the total cluster energy E_w (E_s). If at least one cluster in $r - \phi$ view and one in z view are recorded, the two clusters are associated to form a photon candidate. This procedure defines a photon candidate and measures its energy; the following step is to calculate the direction and so the momentum of this particle. It is a natural choice to keep the J/ψ decay vertex as originating vertex, i.e. the one which has been reconstructed by means of the fit on the two muon tracks. We finally

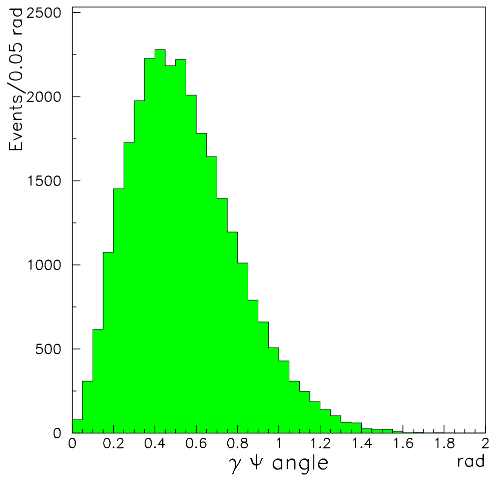

Figure 5.2: *Angular opening between J/ψ and photons in $B_s \to J/\psi\eta$ events generated with* BGENERATOR. *The detector and trigger simulation, the reconstruction described in chapters 2 and 4 have been applied to the muons of this dataset. The informations on the photons have been read on the generation banks. On these photons we applied a detection efficiency function that will be described in 5.4.2 and that substantially selects photons with energy higher than 1 GeV.*

have all the ingredients to completely reconstruct a photon candidate:

$$\overrightarrow{P}_\gamma = E_{Tower} \cdot \widehat{V}_{J/\psi \to cluster}$$

where E_{Tower} is the energy of the calorimetric tower and $\widehat{V}_{J/\psi \to cluster}$ defines the direction of the line connecting the secondary vertex with the centroid built in the CES. When more than one J/ψ is reconstructed, a photon candidate is defined for each J/ψ.

Fiducial requests and corrections

In reconstructing photons we decided to consider only the two more energetic clusters in the CES chambers, so there is no attempt to find multiple candidates per single calorimetric tower, making use for instance of all the clusters present in a tower. Keeping all the candidates, assigning for example as energy of a photon the fraction of energy of the tower calculated on the relative energy values of the clusters, is useless since the energy resolution of the chambers is very limited (see figure 5.3).

A peculiarity of these energy measurements with the central calorimeter has been pointed out in test beam and cosmic rays studies [2]. These studies show that the measured energy presents a saddle dependence on the position where the photon hits the tower, the saddle point is on the center of the tower, the increase is in $r - \phi$ direction (the local X) and decrease in the z direction (figure 5.4).

This behavior is connected to the geometry of the detector. The *wave-length-shifters* that collect the light are placed on the $r - \phi$ (X) border of the towers and not on the Z one (see section 2.5), therefore efficiency in collecting signal is higher for photons hitting the proximities of the X tower borders[1] and lower close to the Z tower borders, due to

[1] The $r - \phi$ section of the plot shows the typical behavior $\cosh(\frac{x}{\omega}) = \frac{e^{x/\omega} + e^{-x/\omega}}{2}$, where $e^{\pm x/\omega}$ parametrizes the attenuation of light intensity due to propagation [2].

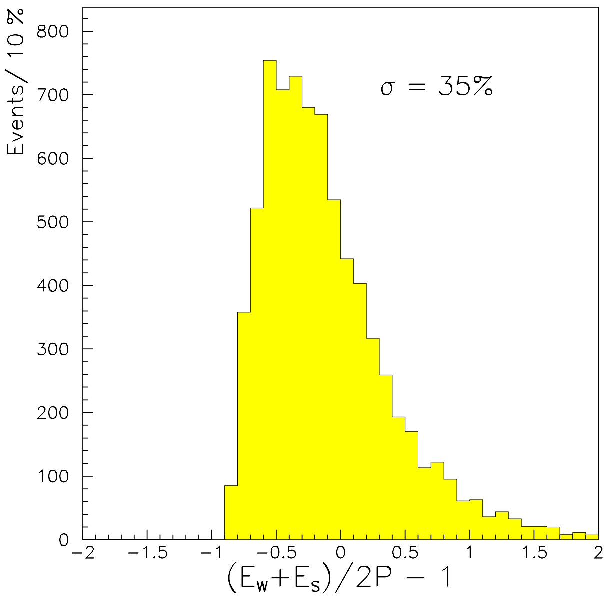

Figure 5.3: *CES relative energy resolution for a low E electron dataset (see 5.2.1). The histogram describes the variable* $\frac{E_w+E_s}{2P}-1$*, where* P *is the total momentum of the electron as measured by the tracking system. The width of the central part of the curve,* $\sim 35\%$*, is assumed ad a row extimation of the energy resolution of the proportional chambers.*

the not total shower inclusion in the tower. A correction algorithm, set up during the test-beam and cosmic rays studies, allows to correct these non linear energy response, nevertheless a conservative choice suggests to limit the fiducial region to the central area of the calorimetric towers. The containment of the photon inside the tower actually is a prerequisite in order to maintain a good energy resolution.
Besides this there is a further reason that lead to reduce the fiducial region on the calorimeter. The clustering algorithm on the CES is "linear" if the distance of the cluster center from the tower border is bigger than its half-width. This guarantees that the electromagnetic shower, during its developing, hits only the active area of the wire and strip chambers. Analyzing the photon dataset originated from the π^0 decay (see section 5.5) reconstructed on the same J/ψ dataset we observe that the cluster widths for photons of energy around 1 GeV are on average of 2.5 channels and that less than 4% of them are formed by more than 5. This suggests to exclude from the fiducial region for the reconstruction the areas of the towers at less than 2 strips (or wires) from the borders. The figure 5.5 shows the average profile of the cluster width as a function of the local X coordinate in the CES. The distribution is substantially flat in the interval [-20,20] cm. Thus we decided to accept only photons reconstructed at less than 20 cm from the center of the chamber (in the $r-\phi$ view), which means at least at 3 cm from the border; analogous request is applied on the Z view, at least 3 cm from the border.

5.2 Photon energy measurement

We yet pointed out that the calorimeter has been designed for energy measurement of particles or jets with momenta higher than the ones involved in this analysis; the test-beam

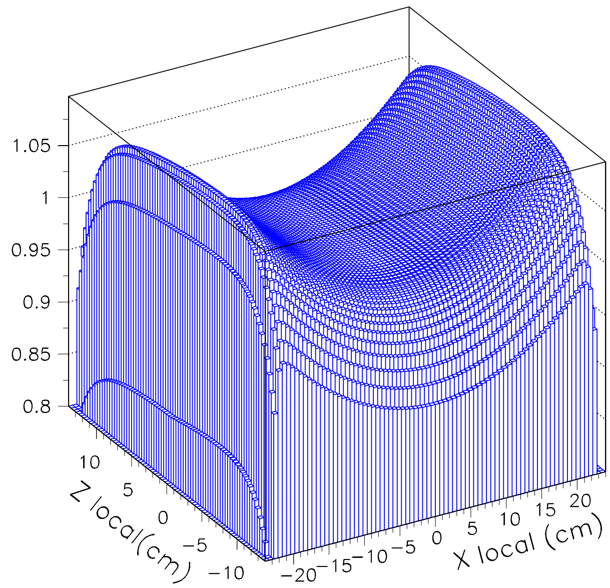

Figure 5.4: *Energetic response of a calorimetric tower as a function of the local coordinates. The value at the center of the tower has been normalized to 1.*

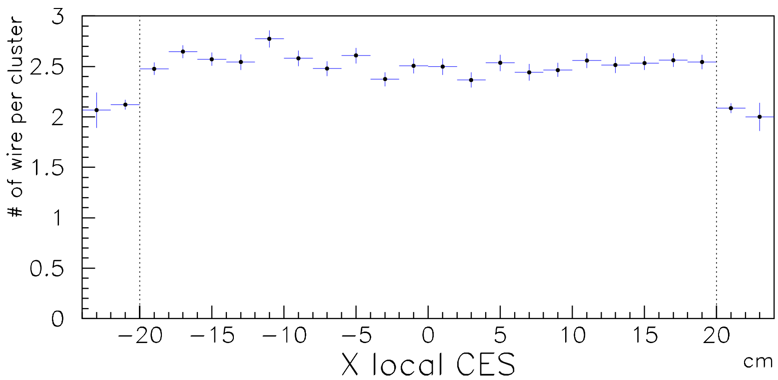

Figure 5.5: *Average width profile for the cluster in the CES strip chambers as a function of the X local position. The distribution is almost flat inside the fiducial region.*

studies indicate that at low energies the resolution is limited and that the calibration is not correct (see figure 5.6 and [1],[3]). Besides the difficulty to detect low energy photons in an hadronic environment with a not optimized calorimeter, there is another complication: there is no pure low energy photon dataset which can be used for calibration and algorithm optimization studies. A possible way to follow to go around this problem is to use the copious pion production in an hadronic environment and to reconstruct a π^0 dataset in the J/ψ dataset, selected with the same requests applied to reconstruct the photon candidates from the $\eta \to \gamma\gamma$ decay. Still, the kinematics of the pion decay and the energy cut on the photons force a large part of them to hit the same tower; this peculiarity makes this photon dataset useless to the calorimeter calibration. In section 5.5 we fully discuss this issue.

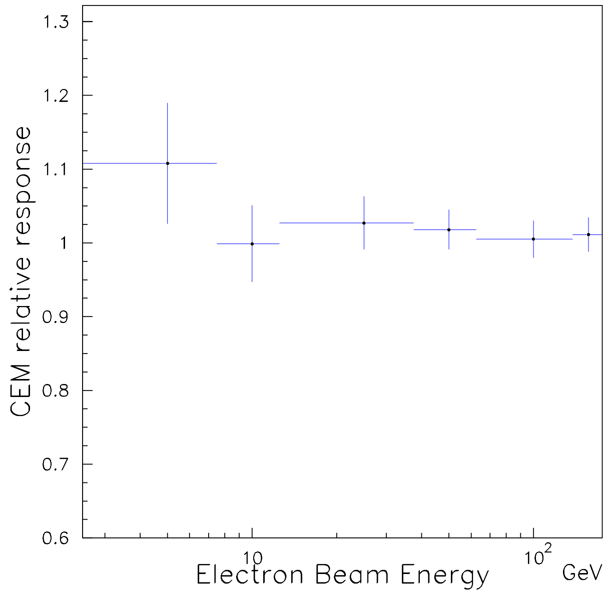

Figure 5.6: *Energy relative response $E_{Tower}/P_{electron}$ of the central electromagnetic calorimeter for electrons of 5, 10, 25, 50, 100, 150 GeV.*

5.2.1 Calorimeter calibration

In order to solve this problem we used an electron dataset originated from photon conversions $\gamma \to e^+e^-$ both for the calorimeter calibration and for the subsequent detection efficiency calculation. The adopted procedure substantially follows the one used in [4], [5] and we will describe it in details. The measurement of the electron momentum in the CTC is subject to a negligible error when compared to the measurement in the calorimeter[2], therefore we can assume this procedure to be similar to a real test beam. Three objections can be opposed to this sentence. Firstly we have to bear in mind the different energy loss of a photon and of an electron in crossing matter. Secondly, the possibility of multiple interaction in the same event, the quark hadronization, the presence of the *underlying event* are all phenomena which release energy inside the detector and so also in the calorimeter tower where the photon has been reconstructed and thus to modify the calibration. Finally, a uncertainty on the particle identification still holds. We will now show how these objections can be overcome.

Conversion electron dataset selection

The strategy adopted considers a photon dataset converting in e^+e^- pairs and try to identify one of the two "legs" of the conversion using all the detectors, while for the second one we use only the tracking system and not the calorimeter. This method provides a pure set of electrons whose momentum is measured with high precision and without any calorimetric request. The e^+e^- pairs identification substantially follows the one adopted in [6]. The search for conversion $\gamma \to e^+e^-$ begins in an inclusive electron dataset, formed by events with one track of $P_T \gtrsim 6$ GeV/c and one EM cluster of total energy greater

[2]The error on the quantity P_{Track} is around $\Delta P_{Track}/P_{Track} \approx 0.1\% \times P_{Track}(GeV/c)$.

than 8 GeV[3].
The conversion search algorithm looks for a second track, besides the trigger one, with opposite charge and transverse momentum greater than 0.5 GeV/c, to this pair we apply the request presented in table 5.1. To the two selected tracks we apply a kinematic fit algorithm (`CTVMFT`) which handles the pair as originating from a conversion $\gamma \rightarrow e^+e^-$ and not simply as from a common vertex[4] consequently we apply a cut on the fit χ^2 probability. We then require the conversion vertex just reconstructed to be distant at least 30 cm from the beam line (see figure 5.7). In order to limit the extra activity in the region the soft electron is pointing to, we impose that no other track points to that *half-wedge* (see section 2.5.1) and that the released energy in the other 4 towers of the *half-wedge* to be lower than 0.5 GeV. These requests guarantees the pair of clusters reconstructed in the CES to be associated without ambiguity to the electron track and that the activity in that region due to extra tracks or energy release is negligible.

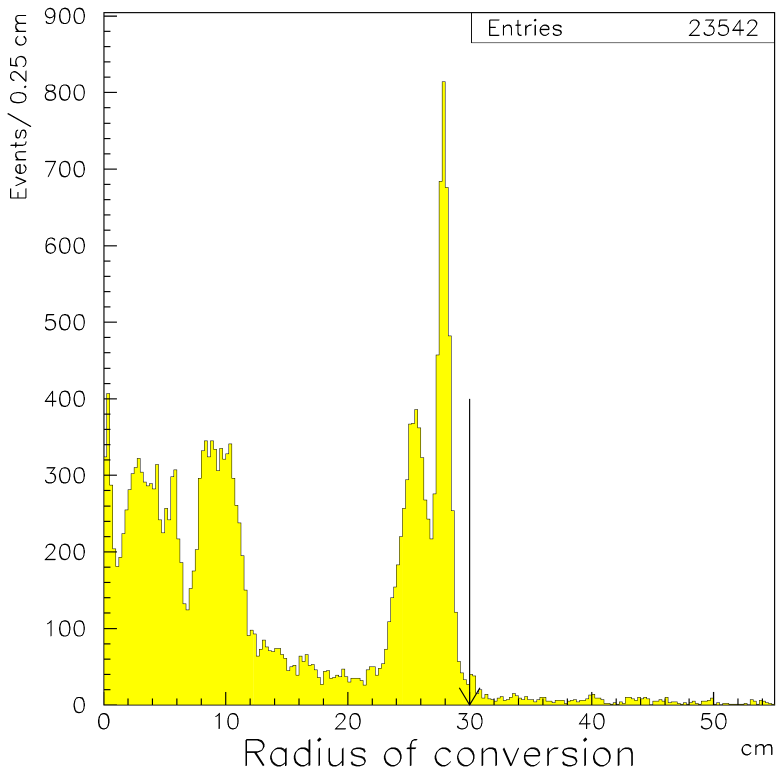

Figure 5.7: *Conversion vertex distance from the beam line. The peaks due to the presence of material are clearly visible; the beam-pipe, the SVX microvertex detector, the VTX and the CTC inner wall. The arrow indicates the maximum accepted conversion radius.*

[3]The dataset has been selected by the level 2 trigger CEM_8_CFT_7_5_XCES and the level 3 trigger ELEB_CEM_8_6. The first one requires the presence of a CES cluster matching (in the X view) a CEM cluster of at least 8 GeV of transverse energy and of a track with minimum P_T of 7.5 GeV/c. The second one requires a CEM cluster of at least 8 GeV of transverse energy and a track with $P_T > 6$ GeV/c, plus other identification requests.

[4]The fitting code has been designed in order to handle also pairs of tracks with a very small relative opening angle, where a standard *vertex constrained* fit becomes instable. A *conversion constrained* fit imposes further conditions; the opening angles in the two views $r - \phi$ and z are set equal to zero.

Dataset	L2 CEM_8_CFT_7_5_XCES L3 ELEB_CEM_8_6
Trigger electron	$\lvert\eta_d\rvert \leq 1.1$ $E_T \geq 8$ GeV $P_T \geq 6\,\mathrm{GeV/c}$ $\lvert\Delta z\rvert \leq 4$ cm $\lvert\Delta x\rvert \leq 3$ cm $\chi^2_{strip} \leq 10$ $\chi^2_{wire} \leq 10$ $E_{Had}/E_{Em} < 0.1$
Track (CTC)	3D track ≥ 2 axial superlayers in CTC with ≥ 4 hit ≥ 2 stereo superlayers in CTC with ≥ 2 hit scale factor in covariance matrix = 2.4
Track (SVX)	Re-tracking with SVX informations Number of hits ≥ 3
$\gamma \to e^+e^-$	Electron + opposite charge track $P_T > 0.5$ GeV/c for the second track *conversion constrained* fit with `CTVMFT` χ^2 probability $> 0.1\%$ The two tracks must point to two different *half-wedges* The sum of the energy released on the other 4 towers of the *half-wedge* must be < 0.5 GeV Conversion radius $R < 30$ cm

Table 5.1: *Selection cuts for the trigger and "soft" electrons.*

Data-Monte Carlo compatibility checks with electrons

Once the electrons dataset has been identified and the their impulses measured, we proceed, event by event, to the read-out of the energies on the electromagnetic calorimeter towers and we evaluate the variable E_{Tower}/P_{Track}. Ideally this quantity is expected to be distributed around the value 1, with the width dominated by the energy resolution of the calorimeter; the figure 5.8 shows the variable for low impulse electrons ($P_{electron} \lesssim 10$ GeV/c). So the raw readout of the calorimeter on average underestimates the electron energy of 7%. The reasons of this behavior can be related either to effects of radiating materials in front of the calorimeter or to the a real not correct calorimeter calibration at low energy; still this confirms the necessity to proceed to a recalibration. The next step is

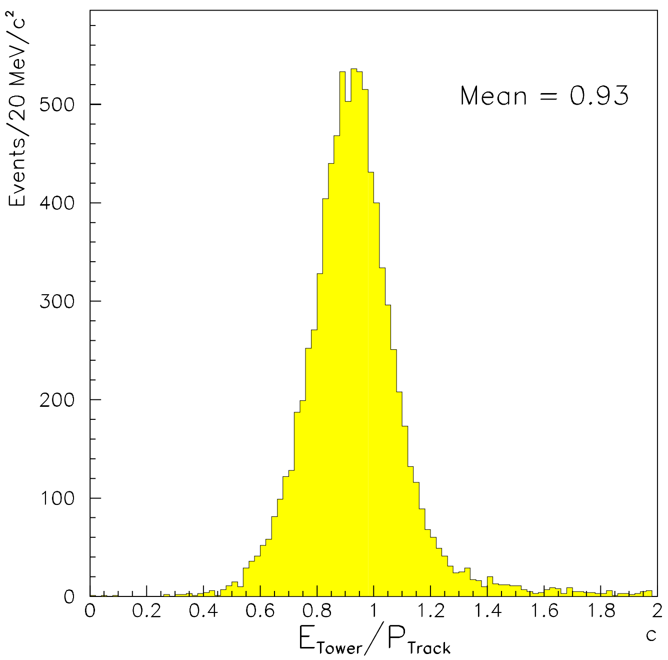

Figure 5.8: *Inclusive distribution for the variable* E_{Tower}/P_{Track}.

to verify the effective matching between the raw calorimeter readout and the calorimeter response as simulated with the Monte Carlo. We have in fact to keep in mind that this procedure aim to recalibrate the calorimeter as regards the photon energy measurement, and the only way to parametrize the photon behavior inside the detector is to refer to the simulation (QFL). A good agreement between conversion electron and Monte Carlo electron would allow us to deem the behavior of the photons inside the detector to be correctly simulated. Here rises the need to validate the detector simulation by the comparison with the data. The figure 5.9 shows that the simulation well describes the E/P variable as a function of P, even at low momenta and then we can conclude that it correctly takes into account the material present in front of the calorimeter towers. A second check is presented in figures 5.10 that show the goodness of the simulation in parameterizing the non linear behavior of the calorimeter as a function of the electron position inside the tower, with a sensible disagreement only close to the internal border of the 0 ring.

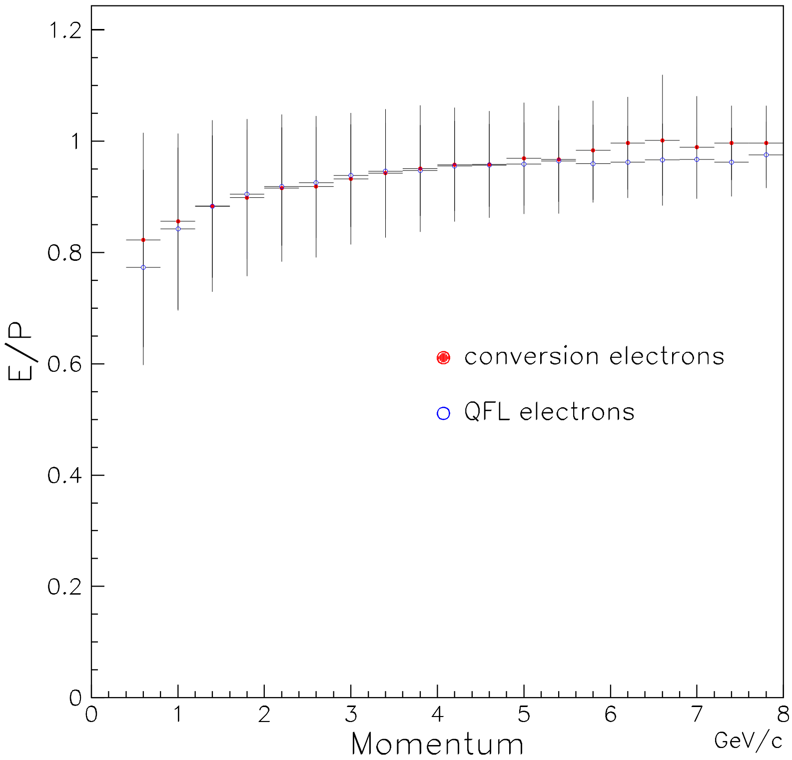

Figure 5.9: *E/P profile as a function of the P momentum for conversion and* QFL *electrons. The points and the bars are respectively the means and the sigmas of the interpolating gaussians to the E/P distributions.*

Electron-photon differences

We can now consider the last of the three questions still opened regarding the validity of this calibration method. For photons and electrons of energies greater than one GeV the phenomena of interaction with matter, important for the calorimeter calibration, are the pair production for the photons and the breaking radiation, *bremsstrahlung*, for the electrons. The converting photons can be detected only if the conversion occurs immediately before the calorimeter towers, the energy loss in not instrumented regions (as the solenoid joke) is then limited. The electron instead are subject to an energy loss due to *bremsstrahlung* all along the detector. On the average the photon detected in the calorimeter lost less energy than an electron with the same initial energy did, this explains the behavior shown in figure 5.11 that underlines the difference between the two particles, difference which is relevant at low momenta, region where the released energy fraction before the calorimeter becomes important.

A further difference between electron and photon regards the development of the calorimetric shower. The longitudinal development can be parametrized by means (see [7]) of:

$$\frac{dE}{dt} = E_0 b \frac{(bt)^{a-1} e^{-bt}}{\Gamma(a)}$$

with $a - 1 = b(\ln(\mathrm{E_0}/\mathrm{E_c}) + \mathrm{C_i})$, where E_c is the critical energy (for the lead, which composes the calorimeter, is $E_c \approx 7.3\mathrm{MeV}$ and $b = 0.45$), with $t = x/X_0$ (penetration depth in the material in radiation length unit) and with $C_\gamma = +0.5$ and $C_{electron} = -0.5$.

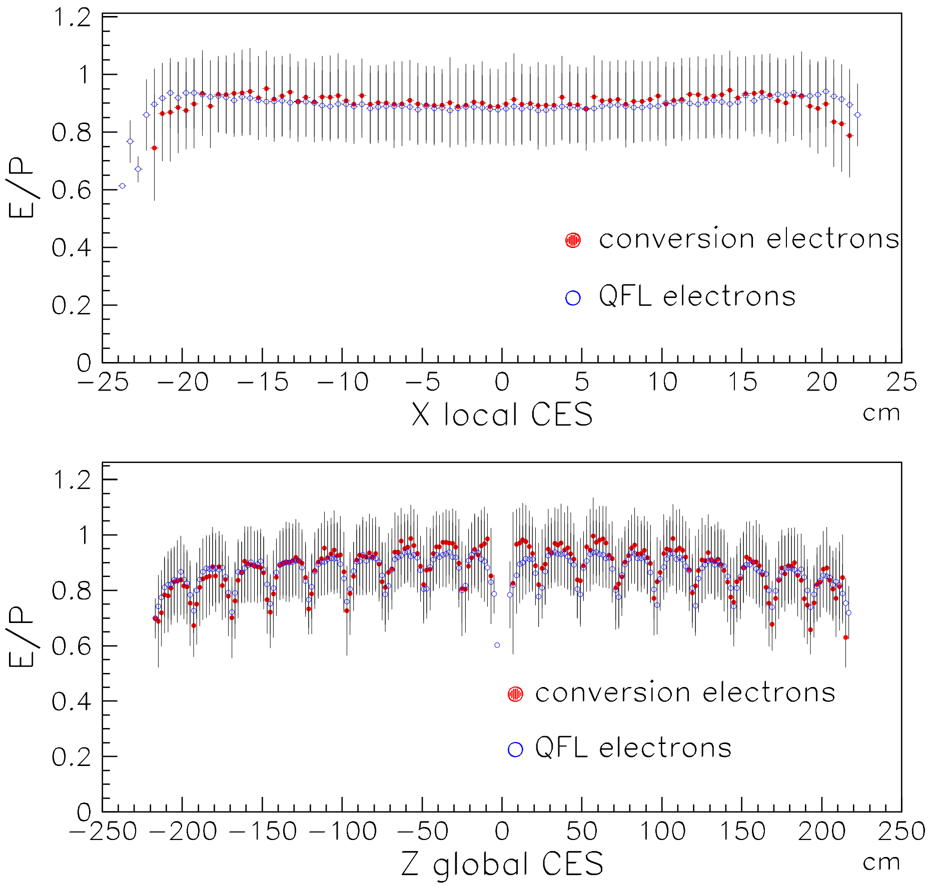

Figure 5.10: *E/P profiles comparison between conversion and* QFL *electrons as functions of the local X in the CES and of the global Z position of the intersection between the electron track and the chamber plane. The error bars show the sigma of the distribution in each channel.*

The picture 5.12 shows the *stopping power* as a function of penetration depth for particles of 1, 2, 6, 20 GeV. The hermeticity of a tower of 18 radiation lengths is almost total for photons of energy of the order of 1 GeV. Incidentally it is worthwhile to notice that at this energy the release rate for electrons and photons at a depth of $\sim 6X_0$ is analogous; this suggests that the energy release, and then the chamber response, is very similar in the two situations.

Calibration parameters for photons

The final step to perform, once checked the goodness of the detector simulation as regards the material and the calorimeter response, is to calculate the correction function. This procedure is based exclusively on the Monte Carlo. The detector simulation program, QFL, allows to generate and simulate single particles with any energy spectrum, angular distribution or generation vertex. We then generated a single photon set with a exponentially decreasing energy spectrum, as suggested on figure 5.1, and with the same distribution of the primary vertex Z coordinate observed in the J/ψ dataset. It is funda-

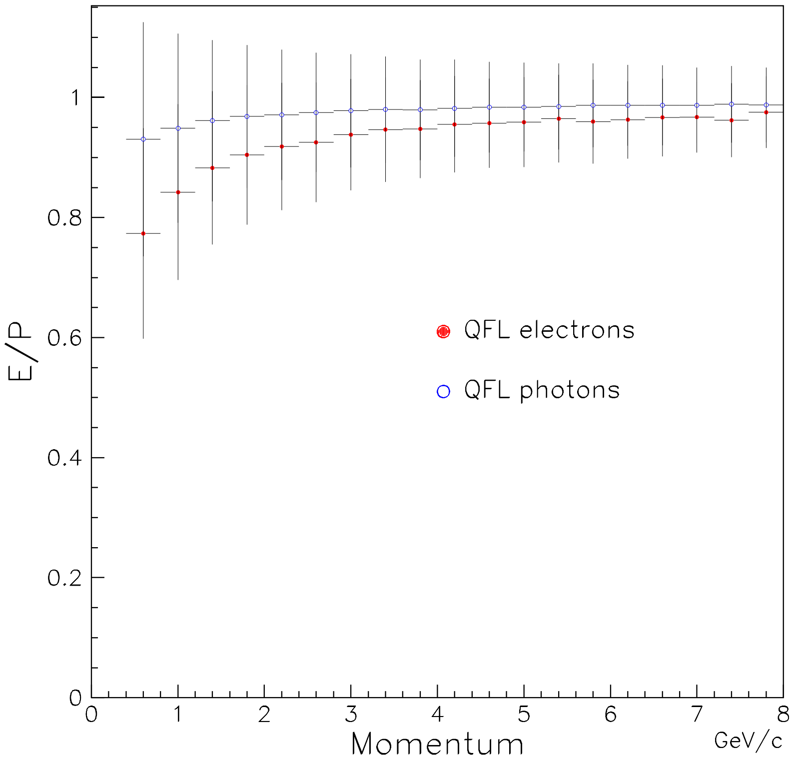

Figure 5.11: *E/P profile as a function of the momentum P for electrons and photons generated with* QFL. *The points and the bars are respectively the means and the sigmas of the gaussians interpolating the E/P distributions.*

mental to pay attention to this aspect of the simulation since this distribution affects the average quantity of material crossed by photons before to reach the calorimeter tower. The calorimetric response is compared to the exact value read on the generator banks. The figure 5.13 shows the variable E/P ($=E_{Calorimeter}/E_{Generator}$) as a function of the exact energy P ($= E_{Generator}$) for the various tower rings.

5.3 η signal reconstruction

Once identified the photons in the event and applied the correction algorithms we select the ones with energy higher than 1 GeV and we look for the η candidates among the pairs with invariant mass $M_{\gamma\gamma} < 1.1\text{GeV/c}^2$. As we have done for the J/ψ multiple candidates (see 4.3) also in this case we keep all the photon pairs satisfying the requests. The number of combinations per event is shown in figure 5.14. The reconstruction of η candidates is now completed. In figure 5.15 we present the invariant mass spectrum of all the combinations; the π^0 peak is evident, while no η signal is visible. The absence of an η signal after the calorimeter calibration is problematic since we cannot check the correctness of the procedure, but especially in the perspective of defining a mass window for the continuation of the analysis. For these reasons we introduced further cuts in order to reject background and highlight an η signal; we used especially isolation cuts which "clean" the signal but, due to their nature, difficult to evaluate in term of efficiency. For

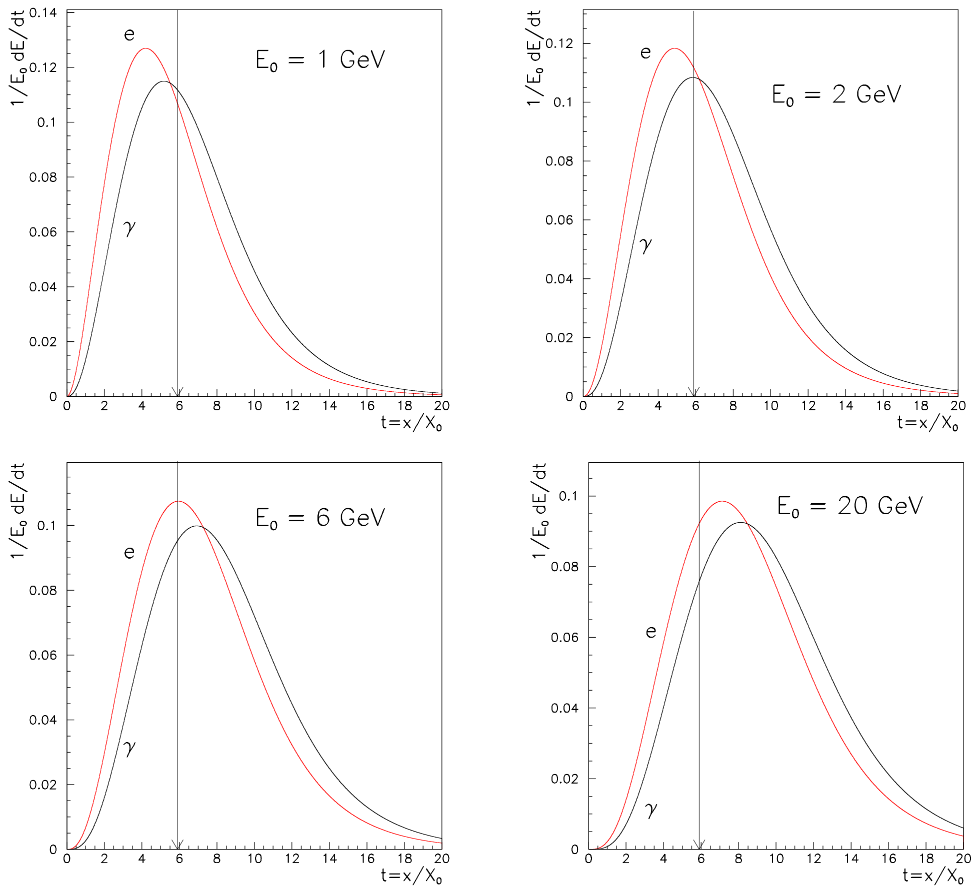

Figure 5.12: *Stopping power normalized to the initial energy as a function of the penetration depth in radiation length units for the CDF electromagnetic calorimeter. The arrows indicate the CES position. For initial energies close to 1 GeV the shower generated by photons and electrons is analogous at this depth.*

this reason these selections are applied only on this particular circumstance and not in the rest of the analysis.
In order to increase the statistics we removed the limitation to only 3 triggers and the request for the two μ to be detected in the SVX. These requests, necessary for the analysis, do not influence the calorimeter calibration. We then decided to apply a cut on the Z coordinate of the secondary reconstructed vertex at $|Z_{SecVertex}| < 30$ cm since imposing the detection of the two muons in the SVX bounds the vertex to be reconstructed inside this region and then influences the range allowed for the polar angle θ of the photons and consequently also the quantity of material that can be crossed.[5]
Besides these criteria concerning efficiency and acceptance we used three isolation cuts. The first request uses informations collected in the hadronic calorimeter and imposes a limitation on the ratio $E_{had}/E_{em} < 0.05$, where the energies are read in the corresponding sections of the calorimeter (E_{em} is then simply the photon energy). The second request discards all the photon candidates with other reconstructed clusters on the two CES strip and wire chambers (besides the two yet associated to form the γ candidate). The last

[5]The quantity of inert material before the calorimeter scales proportionally to $\frac{1}{sin(\theta)}$.

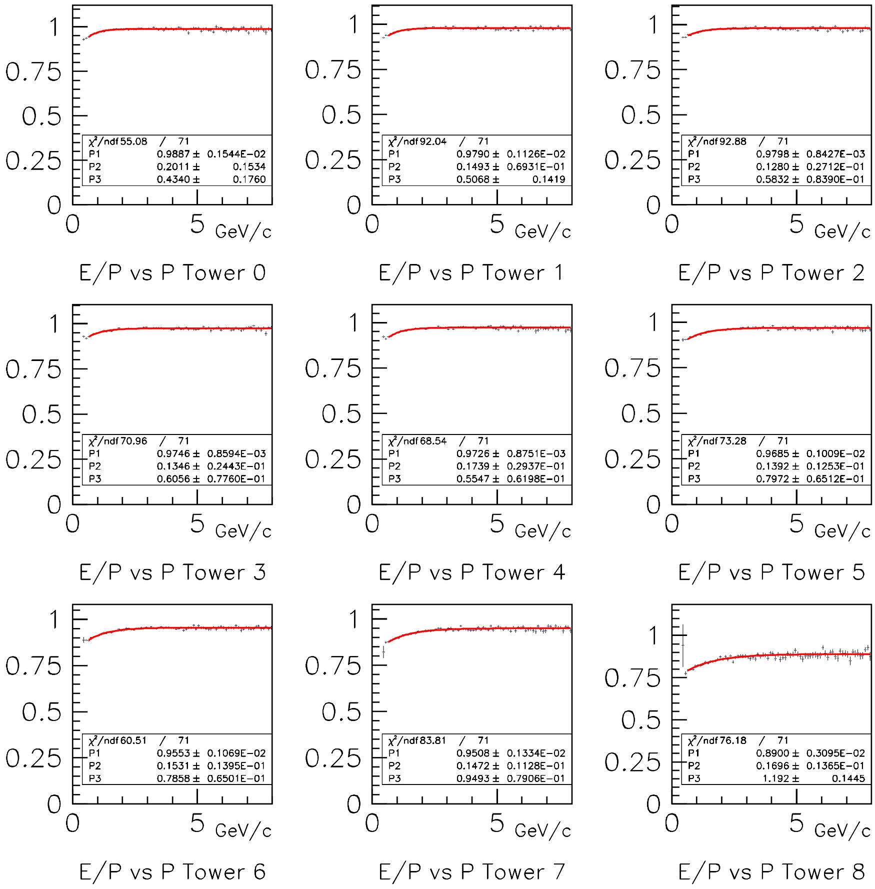

Figure 5.13: *E/P profiles as function of momentum P for photons generated and simulated with* QFL *in the 9 towers. The interpolations provide the parameters for the correction functions.*

requirement introduces the isolation variable

$$I_E = \frac{E_\gamma}{E_\gamma + \Sigma_8 E}$$

where E_γ indicates the photon energy, which means the energy of one calorimetric tower, and $\Sigma_8 E$ indicates the sum of the energies of the 8 adjacent towers (exclude the ones where other photons have been reconstructed). We then impose $I_E > 0.5$. The table 5.2 resumes the applied selections. After applying these cuts, an evident η signal appears in the invariant mass spectrum $\gamma\gamma$ as shown in figure 5.16. The signal is centered at 550 ± 14 MeV/c^2 and has a width of 56 ± 14 MeV/c^2, confirming the validity of the recalibration applied and providing an estimate of the signal width.

MC

The same reconstruction algorithm used to process the data has been applied to the Monte Carlo dataset generated with BGENERATOR and PYTHIA. In figure 5.17 we show the invariance mass spectra $M_{\gamma\gamma}$. The PYTHIA generated dataset shows an evident π^0

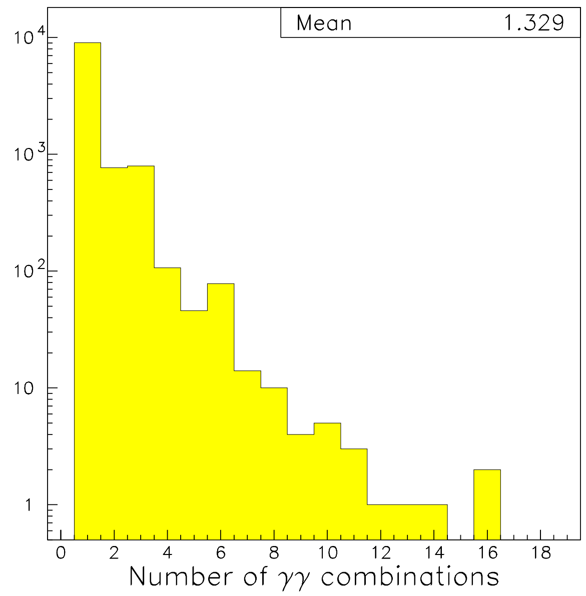

Figure 5.14: *Number of $\gamma\gamma$ combinations per event.*

Modified cuts	
Triggers	all
μ in SVX	-
$\lvert Z_{SecVertex}\rvert$	< 30 cm
E_{had}/E_{em}	< 0.05
# of clusters in CES	$\leq 2+1$
I_E	> 0.5

Table 5.2: *Selections on photons used to show the $\eta \rightarrow \gamma\gamma$ signal.*

signal and just an hint of η signal. The BGENERATOR dataset (where B_s has been forced to $B_s \rightarrow J/\psi\eta$) shows an η signal reconstructed with a resolution around 50 MeV/c^2. This value is in good agreement with the one previously estimated on data; this resolution can better be understood looking separately to the two main contributions to the invariant mass. The relation $M_{\gamma\gamma} = \sqrt{2E_{\gamma_1}E_{\gamma_2}(1-cos(\Theta_{\gamma\gamma}))}$ suggests that the two variables to study are the photon energy and their reciprocal direction, i.e. their separation angle. The error on this last variable depends on the error on the cluster positions reconstructed in the CES[6], the error on the energy is obviously related to the resolution of the calorimeter towers.

Figure 5.18 shows these two contributions. The worsening of the mass invariant resolution due to the limited spatial resolution on the CES appears to be negligible with respect to the energy resolution ($\sim 10\%$ when combined in quadrature).
In order to evaluate the position error on reconstructing the clusters in the CES we consider the electron tracks selected in the conversion dataset and we extrapolate their trajectories to the CES. The residuals between the reconstructed position and the position

[6]The position of the vertex influences the opening angle between the photons only to higher orders.

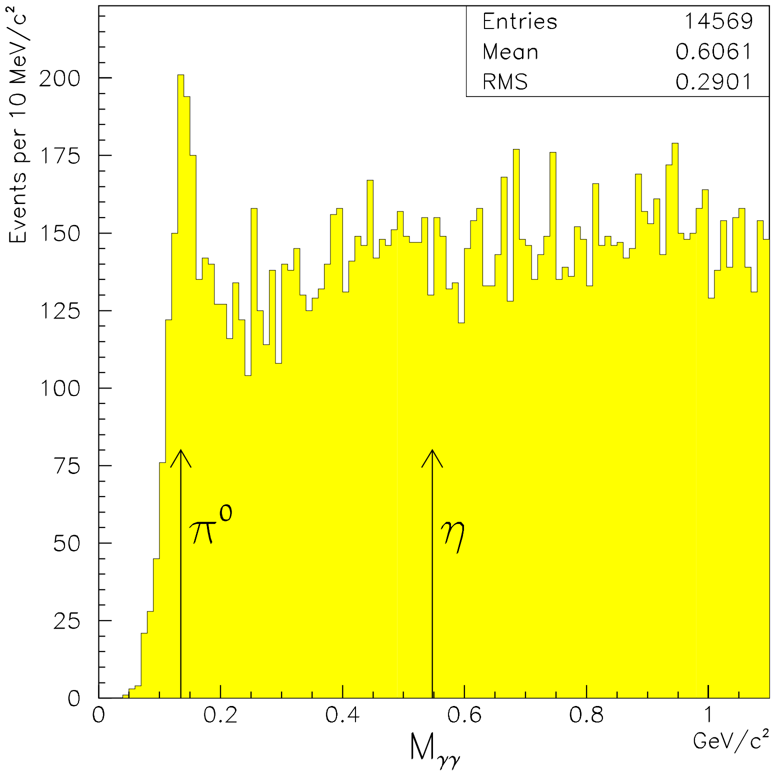

Figure 5.15: *Invariant mass $M_{\gamma\gamma}$ after the calorimeter calibration.*

of the extrapolated point on the CES plane provide an estimate of the resolution of the proportional chambers (after deconvolving the position error due to the track extrapolation).

This exercise becomes interesting when applied with to the Monte Carlo dataset of photon pairs hitting the same tower, and so photons discarded by our reconstruction algorithm. The relative energy resolution has been estimated to be around 35% (see figure 5.3); applying this (gaussian) error to the photon pairs on the same tower we obtain an invariant mass spectrum of width equal to 77 MeV/c^2, value exceeding of about 50% the one obtained assuming the energy resolution of the towers. This decreasing of resolution justify our choice in not using the η candidates with both photons in the same tower.

5.4 Reconstruction efficiency

5.4.1 Geometric acceptance

In the previous sections we have shown that the choice of considering as fiducial only the central portions of the tower has been imposed by the necessity to maintain a good resolution of the calorimeter (the linearity of the energetic response and the recalibration applied need a good hermeticity). Besides these requests, applied tower by tower, we removed also the photons reconstructed in the region $|Z_{global}| < 10$ cm, where the calorimeter response is badly simulated and then where the energy correction described in 5.2.1 is not reliable. If these cuts to the sensitive region allow to reliably reconstruct

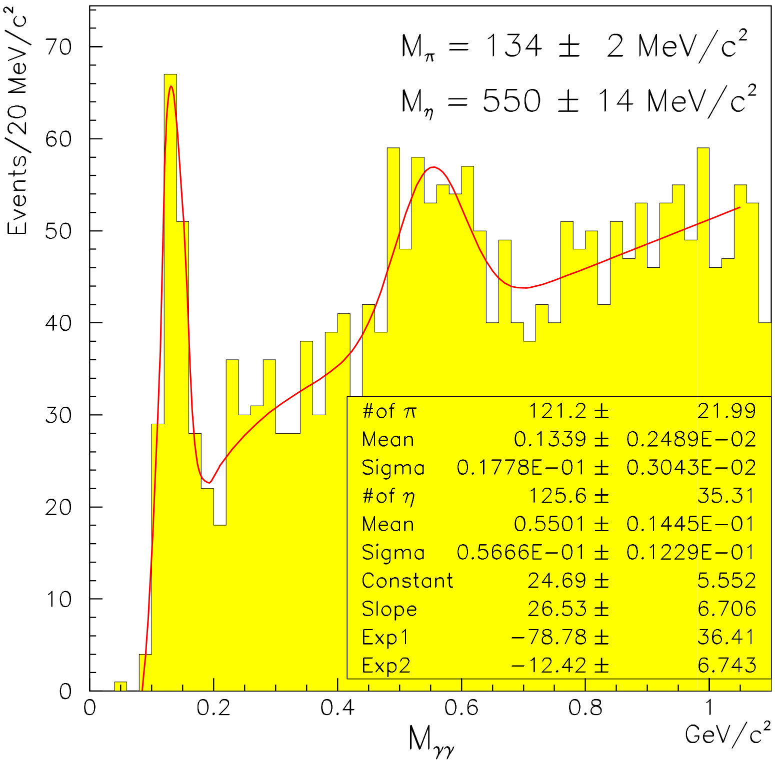

Figure 5.16: $\gamma\gamma$ *mass spectrum after the isolation selections. The two signal peaks have been fit with gaussians. The last four variables of the interpolation parametrize the background shape for which we choose the function* $Constant + E \times Slope + Exp1 \times e^{Exp2 \times E}$.

a photon, the price to pay is a reduced detection efficiency. To evaluate this efficiency we use again the Monte Carlo simulation of $B_s \to J/\psi\eta$ events generated by BGENERATOR. The generated dataset is simulated with QFL and then partially reconstructed in its dimuon section, which undergoes also the trigger simulation. The photons in the events instead does not undergo the simulation, they propagates straightly inside the detector to the calorimeter chambers, where we simulate a gaussian error on the position reconstruction, as estimated on the conversion electrons: we can so evaluate if both the photons originating from the the η hit the fiducial region. This procedure provide a overall geometric acceptance equal to $\epsilon = 19.0 \pm 0.1\%$, where the error is just statistical. In order to evaluate the systematics we varied the gaussian position errors on the CES in the range $[\sigma/2, 2\sigma]$ (see figure 5.18).

5.4.2 $E_\gamma > 1$ GeV request and CEM-CES efficiency

In order to evaluate the efficiency of the energy cut on photons $E_\gamma > 1$ GeV and the reconstruction efficiency of these photons in the CEM-CES detection system we followed the procedure adopted in [4]. The leading idea is to use again the conversion electron dataset described in 5.2.1. The comparison between the number of tracks identified as soft electrons with the number of photons that the reconstruction algorithm has detected in the towers hit by these tracks; all this when the energy read in the corresponding tower is higher than 1 GeV. The application of such a procedure is straightforward, but requires

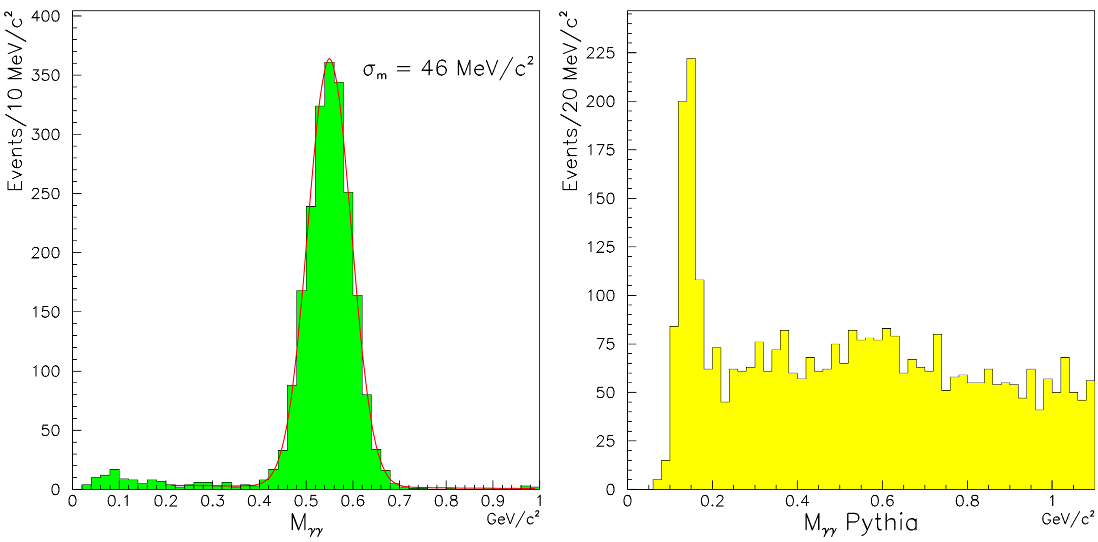

Figure 5.17: *Invariant mass spectrum $\gamma\gamma$ in the two Monte Carlo dataset. The first figure shows the dataset generated with* BGENERATOR. *The second one the dataset generated with* PYTHIA.

a bit of good sense. When crossing the material in front of the calorimeter towers the electron reduces its energy more than a photon of equal energy does. The relative energy difference between photon and electron can be written as $\Delta = (E/p)^{photon} - (E/p)^{electron}$: regarding this effect, for the calculation of the efficiency curve for photons, a photon of momentum p behaves as an electron with corrected momentum $p(1-\Delta)$. This function has been evaluated using QFL comparing the two single photon and electron simulated datasets. The calculation of the reconstruction efficiency at this point consists only in the creation of two histograms, the first one containing the corrected momentum of the incident electrons, the second one containing only the fraction reconstructed on the CES by the clustering algorithm described on 5.1 and passing the 1 GeV cut on the tower energy. The curve shown in figure 5.19 is obtained simply dividing the two histograms bin by bin. It is important to underline that this curve provides the efficiency of the detection+energy cut as a function of the track momentum and not of the calorimetric response; since the track momentum is measured with negligible error with respect to the calorimetric measurement we can calculate the total efficiency of photon detection in the $B_s \to J/\psi\eta$ channel simply applying that curve to the photon spectrum before the detector simulation. Operatively, we interpolated the points obtained with an exponential function and this curve has been used as efficiency curve for each photon. The total efficiency calculated on the $B_s \to J/\psi\eta$ dataset generated with BGENERATOR is $19.7 \pm 0.3\%$, where the error is only statistical. To estimate the systematics we used various functional forms for the interpolation and we obtained an error equal to 0.8%.

To this efficiency value we have to add a corrective term due to the fact that photons that convert to an electron pairs before to cross the solenoid do not reach the calorimeter. The electrons used for the efficiency evaluation of the CES in fact originate from a photon conversion; what we want to evaluate here is the conversion probability for a photon before to exit the CTC. In doing this we make use again of the BGENERATOR Monte Carlo and of the simulation QFL. On the generator banks we selected the photons with energy higher than 3 GeV whose direction of propagation lead them to hit the central region of

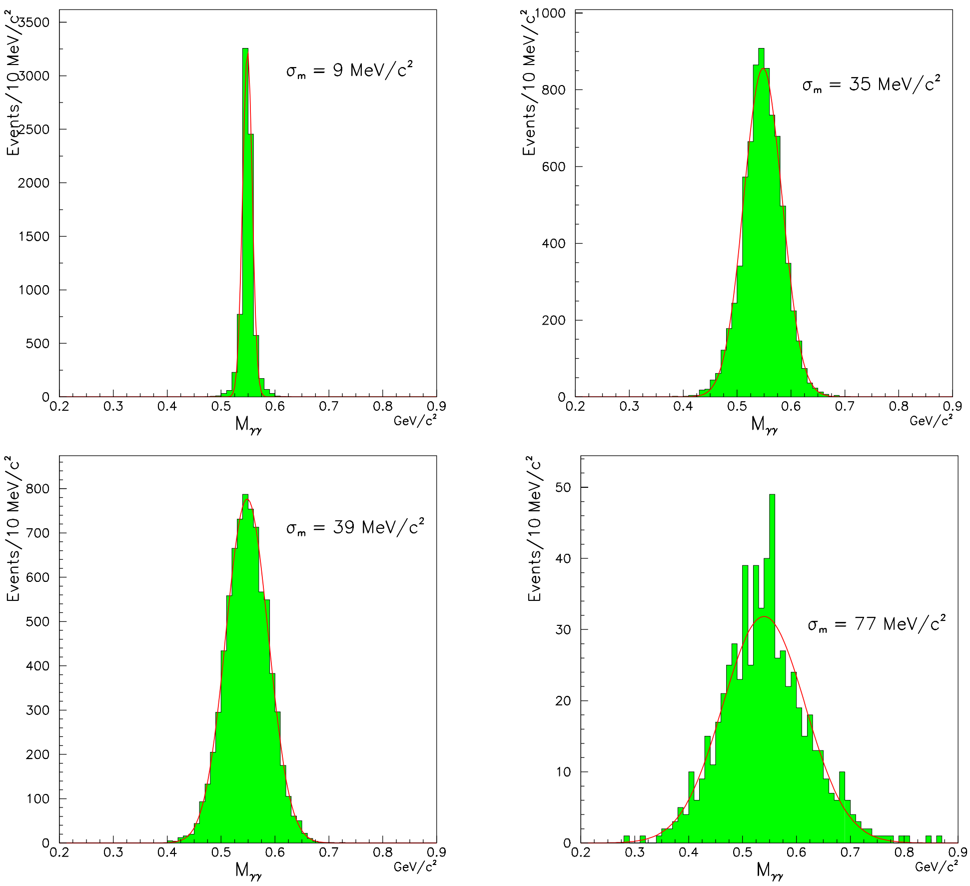

Figure 5.18: *Invariant mass distribution width $M_{\gamma\gamma}$ as a function of the various error contributions. The first figure considers only the position error of the photons in the CES chambers. We assigned the values $\sigma_X(CES) = 0.4cm$ and $\sigma_Z(CES) = 0.7cm$ as position errors, values obtained from the study of the conversion electrons. The second picture considers only the limited energy resolution of the calorimeter towers ($\sigma_E = 13.5\%\sqrt{E}$). The third one merges both the contributions.*
The last figure shows the invariant mass spectrum for photons on the same tower. The resolution adopted for the CES position is still $\sigma_X(CES) = 0.4cm$ and $\sigma_Z(CES) = 0.7cm$, the energy resolution has been assumed to be $\sigma_E/E = 35\%$ as shown in figure 5.3.

a calorimeter tower (at least 6 cm from the border) and then we applied the efficiency curve previously described. For these events we obviously obtain a detection efficiency close to 100%; on the same events we then applied the simulation of the detector[7] and we counted the number of events in which both the photons has been detected in the CES. The ratio of the two numbers provides an estimate of the probability for the two photons *not* to convert before to exit the CTC because QFL parametrizes the presence of material and the conversion are simulated. The request of $E_\gamma > 3$ GeV is applied only to decouple from the two different efficiency curves. The final value is equal to 0.907 ± 0.017.
Also a purely analytic calculation is possible since the total amount of material before the CTC is well known [8] and is equal to $0.0991 \pm 0.0039 X_0$[8]. After these considerations the

[7]The efficiency curve implemented in QFL shows a plateau after 3 GeV too.
[8]This value is obtained considering also the average of the term $1/sin(\theta)$ and considering as radiating

non conversion probability for a pair of photon is equal to 0.857 ± 0.005. The difference between the two estimates is taken as systematic on this efficiency.

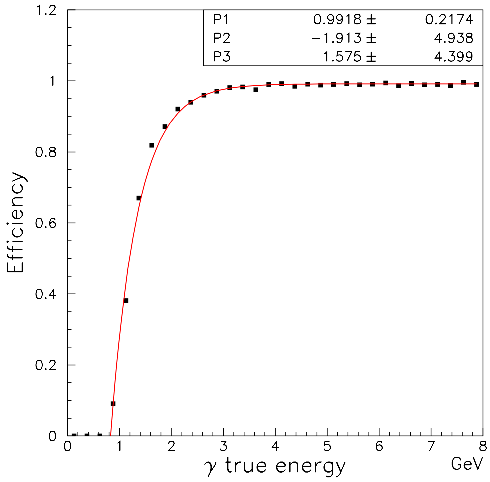

Figure 5.19: *Reconstruction efficiency curve after the request $E_\gamma > 1$ GeV on the photon energy. The fitting curve has a functional form $p_1 - e^{p_2 x + p_3}$.*

5.4.3 No pointing track request

The photon reconstruction algorithm requires that no track is pointing to the towers containing photon candidates. The Monte Carlo simulation is not able to fully simulate the event in its completeness and in particular the multiplicity of tracks inside the detector; for this reason we decided to estimate the efficiency of this request using the data themselves. The procedure follows the one adopted in [5] and is based on the assumption that the multiplicity of tracks in an event is related to the *underlying event*, and then that it is analogous both in the J/ψ inclusive dataset both in the $B_s \to J/\psi\eta$ events. The procedure can be sketched as follows, and the scheme is then applied event by event.
In real J/ψ events we consider ΔR[9] rings in the calorimeter defined by $n \times 0.2 < \Delta R < (n+1) \times 0.2$ and centered on the reconstructed J/ψ direction. Then we measure the percentage of towers hit by at least one track in each interval, this provides the $\epsilon(R_n)$ in each ring. Using the Monte Carlo simulation of $B_s \to J/\psi\eta$ events we generate a normalized histogram with the ΔR distribution of one of the two photons[10], this provides the weight to apply to each of the efficiencies previously evaluated on data. The weighted average is the required total efficiency. The whole calculation has been carried out using the method of J/ψ *sidebands* subtraction.
In table 5.3 we report the partial and total results. The obtained value for $\epsilon_{NoTrack}$ is in good agreement with the one estimated in [5] (0.94 ± 0.02). To obtain the efficiency on both the photons we simply took the square of this quantity and is equal to 0.850 ± 0.006. An alternative method to evaluate the efficiency of this fiducial request, still based on an analysis of the J/ψ data, uses the reconstructed π^0 signal. We reconstruct this

material all the CTC.

[9] $\Delta R = \sqrt{\Delta\eta^2 + \Delta\phi^2} = \sqrt{(\eta - \eta_{J/\psi})^2 + (\phi - \phi_{J/\psi})^2}$.

[10] The two photons obviously show in average the same angular distribution with respect to the J/ψ flight direction.

ΔR	Inefficiency	MC weight
0.0-0.2	0.103	0.04
0.2-0.4	0.106	0.15
0.4-0.6	0.091	0.24
0.6-0.8	0.072	0.20
0.8-1.0	0.062	0.15
1.0-1.2	0.056	0.13
1.2-1.4	0.053	0.04
1.4-1.6	0.052	0.03
1.6-1.8	0.051	0.02
Average inefficiency = 0.08		
Efficiency = 0.922 ± 0.003		

Table 5.3: *Partial and total efficiencies (1-efficiencies) for the request of no pointing track in the calorimeter towers where the photon are reconstructed. The first column indicates the ΔR interval considered, the second one the fraction of towers hit by at least one track, the third one the relative weight as obtained by the Monte Carlo.*

$\gamma\gamma$ efficiencies			
	Eff	Stat	Sys
Geometrical acceptance	0.190	0.001	0.006
CEM-CES efficiency	0.197	0.003	0.008
Non conversion	0.907	0.017	0.050
NO track	0.850	0.006	0.023
	Eff = 0.0288 ± 0.0025		

Table 5.4: *Summary of $\gamma\gamma$ efficiencies.*

signal before and after to remove the towers with pointing tracks: the ratio of the two reconstructed π^0 signals provides an estimate of the efficiency. This ratio is 0.873 ± 0.011, the error is due to the uncertainties on the peak interpolations.
The difference between the two methods is taken as an estimation of the systematic on this efficiency.
In table 5.4 we summarize all the efficiencies concerning the photon detection.

5.5 The π^0 signal

The presence of a π^0 signal in the di-photon dataset revealed to be useful in a pair of situations. In order to study the efficiency of the no pointing track request we have not modified the photon selections; instead for the study of the cluster dimension in the CES we needed to increase the S/N ratio for the π^0. This has been obtained applying again a cut on the isolation variable, $I_E > 0.6$; this value guarantees a good S/N increase without loosing too much statistics. Meanwhile we removed the requests on the minimum muon transverse momentum and we accepted events collected by *any* trigger. The invariance mass spectrum obtained is shown in figure 5.20. The selected dataset contains around

2100 π^0 with a $S/N \approx 2.3$.
We have now to point out a peculiarity of this set of photons. The mass of neutral pion, $m_{\pi^0} = 135\,\mathrm{MeV/c^2}$, is approximatively 1/4 of the η mass, this implies that also the opening angle between the two photons of the decay will be reduced of the same factor. In fact the opening angle is given by the formula $\Theta^2_{\gamma\gamma} \approx M^2/E_{\gamma_1}E_{\gamma_2}$; for photon of energy $E_\gamma > 1$ GeV we find a maximum opening angle of ~ 0.14 radiants, which at a distance of 184 cm (distance of the CES from the beam line) is equal to a total distance of 26 cm, corresponding to about one half of the width tower in X direction and about the width in Z direction. For this reason pairs of photons reconstructed in two different towers hit mostly the $r-\phi$ borders of the towers themselves, as shown in figure 5.21, which shows the local X distribution of the π^0 photons in the CES chambers. This phenomenon, besides to limit the statistics of the reconstructed dataset, modifies the invariance mass spectrum, promoting bigger opening angles, and then bigger masses; for this reason π^0 photons cannot be used for calibration of the calorimeter.

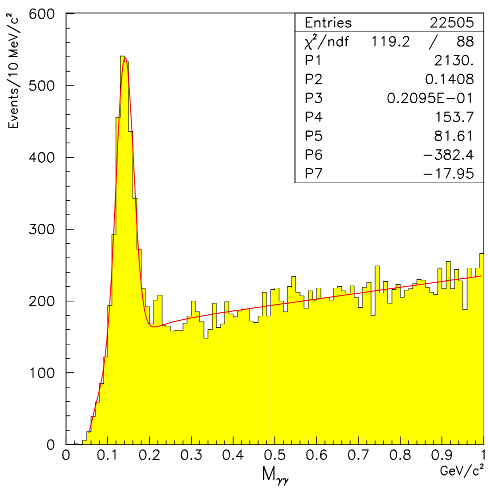

Figure 5.20: *$M_{\gamma\gamma}$ invariant mass after the optimized selections for π^0 signal. The interpolating function is a gaussian for the peak (p_1=♯ of events, p_2=mean, p_3=sigma), for the background is the 4 parameter function $p_4 + p_5 \cdot x + p_6 \cdot e^{p_7 \cdot x}$.*

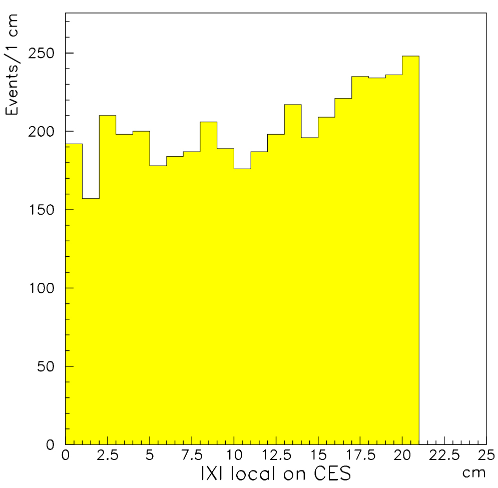

Figure 5.21: *Absolute value of the local position $|X_{loc}|$ in the CES for photons under the π^0 peak. The accumulation in the proximity of the borders is evident. This figure has been obtained with the* sidebands *subtraction method; in this particular situation the background used for the subtraction has been selected only on the right side of the π^0 peak.*

Bibliography

[1] R. M. Harris, R. Blair, S. Kuhlmann, "Ces Response and Chisquared for 1990 Testbeam Electrons" **CDF** internal note **1432**, (Apr 1991)
R. M. Harris, "Definition of CES χ^2" **CDF** internal note **1329**, (Jan 1991)

[2] K. Yasuoka, S. Mikamo, T. Kamon, A. Yamashita, CDF NW Wedge Group, "Response Maps of the CDF Central Electromagnetic Calorimeter with Electrons", *FERMILAB-PUB* **87/175**, (Aug 1987)
Nucl.Instrum.Meth A **267**, 315-329 (1988)

[3] N. Solomey, A. Wicklund, "Study of Electromagnetic Showers In the CDF Central Electromagnetic Calorimeter" **CDF** internal note **247**, (Jun 1987)
S. Hahn *et al.*, "Calibration of the CDF Central Electromagnetic Calorimeter", **CDF** internal note **281**, (Jun 1987)
Nucl.Instrum.Meth A **267**, 351 (1988)

[4] D. Benjamin, V. Papadimitriou, A. Sansoni, M. Shapiro, A. Yagil, "Production of J/Ψ from χ_c decays at CDF", **CDF** internal note **3123**, (Apr 1995)
F. Abe *et al.* (CDF Collaboration), "Production of J/Ψ Mesons from χ_c Meson Decays in $p\overline{p}$ Collisions at $\sqrt{s} = 1.8$ TeV, *Phys.Rev.Lett.* **79**, 578 (1997)

[5] D. Benjamin, W. Hao, V. Papadimitriou, A. Sansoni, S. Tkaczyk, "Production of $\Upsilon(1P)$ from χ_b decay", **CDF** internal note **4392**, (Nov 1997)

[6] M. Tanaka, R. Oishi, Y. Seiya, "Search for $B_d \to K^{*0}\gamma$ and $B_s \to \phi\gamma$ Using γ Conversions", **CDF** internal note **4804**, (Feb 2000)

[7] K. Hagiwara *et al.*, "Review of Particle Physics", *Phys. Rev. D* **66**, 010001 (2002)

[8] A. B. Wicklund, "Determination of CDF Inner Detector Material Using Conversion Electrons", **CDF** internal note **2899**, (Dec 1994).

Chapter 6

B_s and B_u signal reconstruction

6.1 Introduction

After the reconstruction of the 4 body candidates to form the $B_s \to J/\psi\eta \to \mu\mu\gamma\gamma$ event we have to reconstruct the B_s particle. The method to follow obviously consists in calculating the 4 body invariant mass and look to the spectrum for an excess in the proximity of the mass value 5.369 GeV/c^2. In figure 6.1 we present this invariant mass $\mu\mu\gamma\gamma$.

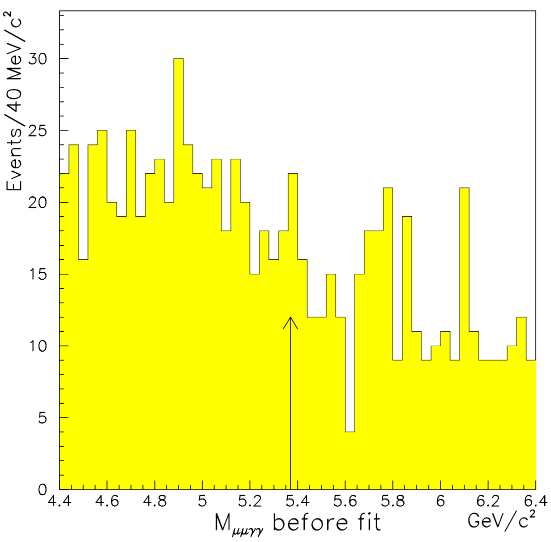

Figure 6.1: *Invariant mass $M_{\mu\mu\gamma\gamma}$ before the kinematic fit.*

This way of evaluating the invariant mass does not consider further informations provided by the physics of the decay. The two muon system, besides having two tracks originated from a common vertex, must also have an invariant mass equal to the J/ψ mass; the two photons too must have an invariant mass equal to the η one. These informations can be integrated in a 4 body invariant mass calculation by means of a *kinematic fit* procedure.
In section 4.3 we saw an example of kinematic fit with the tracks forced to origin from a common vertex, a *vertex-constrained* fit. This procedure showed a notable increasing in the invariant mass resolution and then in the S/N ratio.

Depending on the situation, the algorithms implementing a kinematic fit can be very different; nevertheless the leading idea is common to all of them and in principle it is quite simple. In general a least squares fit algorithm searches the minimum of a function, the χ^2, by varying a series of m parameters in a m-dimensional space. A kinematic fit follows the same procedure, but this time the χ^2 is minimized in a sub-manifold of the parameter space, with the manifold defined by the constraints. The r constraints reduce the parameter space to the $(m-r)$-dimensional manifold, where the kinematic requests (i.e. a common vertex, a definite invariant mass, etc.) are satisfied by construction. So, finding the χ^2 minimum inside the manifold, provides the desired result. After the kinematic fit the parameters assume values satisfying the constraints exactly. The limited resolution of the physical quantities are taken into account in the χ^2 calculated, which parametrizes the verisimilitude of the result.

6.2 Kinematic fit to the process $J/\psi\eta$

The code usually adopted at CDF for a wide set of kinematic fits involving charged tracks is the code called `CTVMFT` (see also sections 4.3, 5.2.1). Nevertheless this code does not allow to introduce neutral particles in the fit procedure; thus we had to introduce a new fit algorithm written to handle two charged tracks and two photons.
The code is based on the algorithm described in [1]; this algorithm is a least squares fit where the search of the (constrained) minimum of the χ^2 is performed by linearizing the equations $\partial\chi^2/\partial\alpha_i = 0$ in the space of parameters α_i. So it is not an iterative fit. An accurate description of the whole procedure is presented in the appendix.

The code has been tested on the Monte Carlo datasets in order to check its correct behavior; figure 6.2 shows that in the Monte Carlo of pure signal, generated with BGENERATOR, the resolution improves considerably, of a factor 2.1.
The same fit procedure has been then applied to the Monte Carlo dataset generated with PYTHIA, figure 6.3 shows that the improvement in resolution put in evidence a signal otherwise not visible.

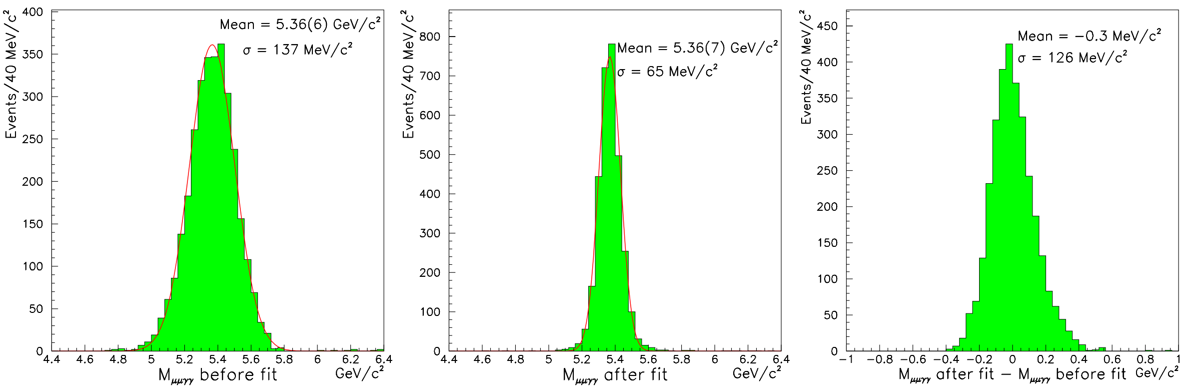

Figure 6.2: *Invariant mass $M_{\mu\mu\gamma\gamma}$ before and after the kinematic fit and difference of mass on the Monte Carlo dataset generated with* BGENERATOR.

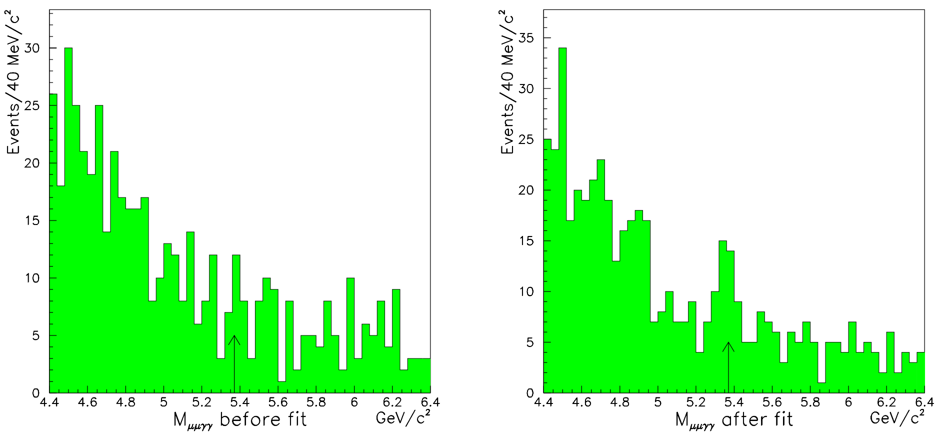

Figure 6.3: *Invariant mass $M_{\mu\mu\gamma\gamma}$ before and after the kinematic fit on Monte Carlo dataset generated with* PYTHIA.

6.3 $J/\psi K^{\pm}$ signal reconstruction

After the selection of the J/ψ dataset we search for a charged kaon in order to reconstruct the $B^{\pm}$ candidate. The CDF detector has no particle identification apparatus able to discriminate between charged πs and Ks and then for the $B^{\pm} \to J/\psi K^{\pm}$ decay search we decided to consider all the reconstructed tracks (passing few quality criteria) as K candidates. The selection procedure follows the one applied in [2] and will be briefly presented.

6.3.1 Quality criteria on tracks

The quality requests usually applied at CDF aim to reduce the background originated by a faulty tracking and to select tracks whose parameters are precisely measured.
The first request, yet applied to the μ tracks, asks the interpolation to use at least 2 *superlayers* with at least 4 *hits* in the $r - \phi$ view and in the z view again 2 *superlayers* with at least 2 *hits*.[1]
Even if it is possible to reconstruct tracks with transverse momenta as low as ~ 250 MeV/c^2, for this study there is no necessity to reach these values of P_T, so we decided to consider only tracks with $P_T > 800$ MeV/c. This choice has operated also [2] since over this value the tracking efficiency is constant.

A further request on the track quality is connected to the (absolute) value of the pseudorapidity of the tracks themselves. For high values the track exits the CTC before crossing all *layers* and then has a lower probability to leave the minimum number of *hits* required for the reconstruction, with a consequent lower efficiency and track quality. For this reason we decided to reduce the acceptance pseudorapidity applying a cut on the exit radius of track; to apply the request we calculate the position of the intersection of the track with the z end walls of the CTC ($Z_{end-plates} = \pm 160$ cm) and we impose the distance from the beam line to satisfy $R^{CTC}_{Exit} > 110$ cm. This request is equivalent to

[1] This reflects the CTC structure which presents 12 *layers* per *superlayer* in the $r - \phi$ view and 6 *layers* per *superlayer* in the z view.

[2] For $P_T < 250$ MeV/c the reconstruction of the tracks is difficult since the curvature radius is so small that they form *loops* inside the detector and they release a great number of *hits* in the CTC inner *layers*.

ask the track to cross at least the first 6 *superlayers* (the most external one, the ninth, has outer radius of 132 cm); this request selects a set of track with enough points in the CTC to guarantee the homogeneity in term of momentum resolution, without a drastic decrease of the geometric acceptance.

With the tracks just selected we form the $B^{\pm}$ candidates; the combinatorial background is then quite high, due to the absence of a particle identification procedure. This background can be reduced since the charged particles produced in a $p\overline{p}$ primary interaction have a P_T spectrum decreasing much faster than the one of the kaons produced in the $B^{\pm} \to J/\psi K^{\pm}$ decay (figure 6.4). Imposing a P_T cut is then useful to increment the S/N ratio; in analogy with [2] we require $P_T(K) > 1.25$ GeV/c.
The reconstruction efficiency for the K candidate so selected has been evaluated by means of the BGENERATOR Monte Carlo and using the informations in [3]; the calculated value is equal to $\epsilon_K = 0.452 \pm 0.016$.

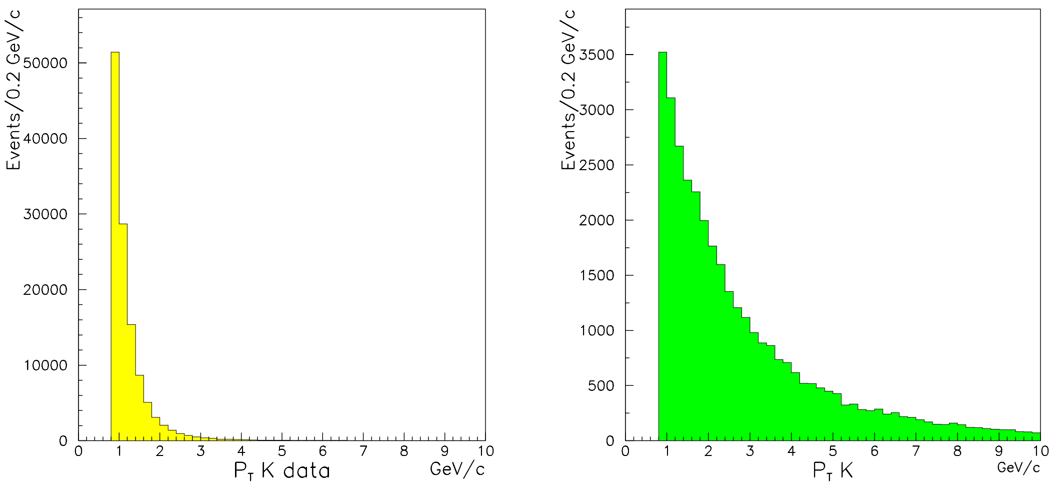

Figure 6.4: *P_T spectrum for the tracks reconstructed after the requests $R^{CTC}_{Exit} > 110$ cm and $P_T > 0.8$ GeV/c. The graph at left shows the spectrum of the charged particles reconstructed on data (background); the right figure shows the same distribution for tracks reconstructed in the $B^{\pm} \to J/\psi K^{\pm}$ dataset generated with* BGENERATOR *and completely simulated and reconstructed.*

6.3.2 $\mu\mu K$ kinematic fit

In order to reconstruct the $B^{\pm} \to J/\psi K^{\pm}$ decay we combine the muons forming the J/ψ candidate and the K candidate using a 3 tracks kinematic fit (`CTVMFT`). This algorithm, applied to the Monte Carlo dataset, guarantees a resolution improvement of a factor 2.5, as shown in figure 6.5.

The same improvement is evident in the data, before the fit no $B^{\pm}$ signal is visible, while a clear peak in correspondence of the expected mass value appears after the fit (figure 6.6).

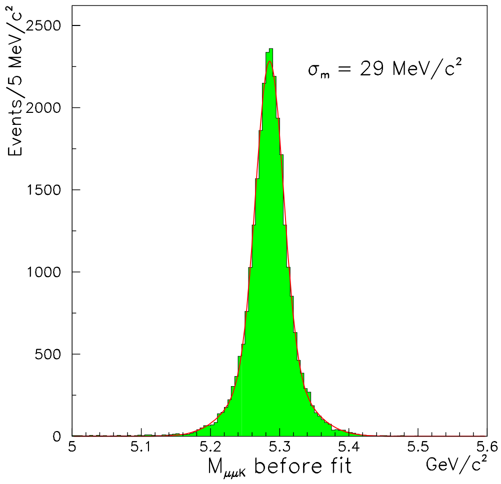

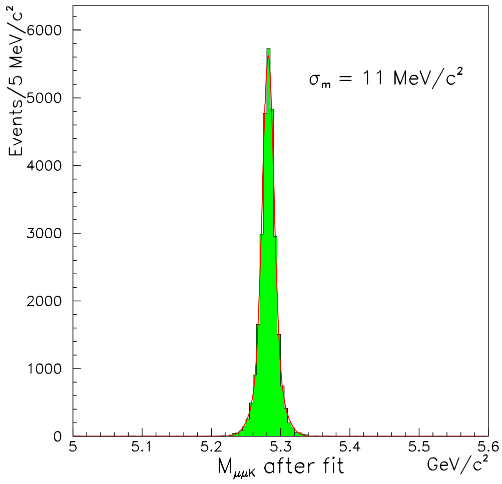

Figure 6.5: $M_{\mu\mu K}$ *invariant mass before and after the kinematic fit on the* BGENERATOR *Monte Carlo dataset. The interpolating curve is a double gaussian, the width is evaluated as the weighted average of the two sigmas.*

6.4 Decay length calculation

The reconstruction procedure of the channel $B_s \to J/\psi\eta$ and $B^\pm \to J/\psi K^\pm$ have not taken into account a peculiarity of the B meson decays which can be exploited by the CDF detector in order to reject background and then to increase the S/N ratio.
The B mesons has an average life τ higher than 1 ps ($\tau(B_s) = 1.461 \pm 0.057$ps, $\tau(B_u) = 1.674 \pm 0.018$ps [3]); this corresponds to a $c\tau \sim 500\mu$m. The B mesons reconstructed have a transverse momentum $\gtrsim 5$ GeV/c and then we expect they present a decay vertex displaced of $c\tau \sim 500\mu$m with respect to the primary vertex. Figure 6.7 shows the projection in the xy plane of this flight distance for the B_s meson.
Since the J/ψ mean life is around 8 orders of magnitude lower than the B one, its decay length can be neglected and then we can consider (as it has been done yet in the kinematic fit) the decay vertex of the B meson to be the one from which the two μ tracks originate.
The quantity usually considered is not the B meson decay length (projected in the xy plane), but the proper lifetime measured in the particle frame of reference multiplied by its speed. This quantity is known as *proper decay length* and a useful definition is[3]:

$$c\tau(B) = \frac{\vec{L}_{xy} \cdot \vec{P}_T(B) M_B}{P_T^2(B)}$$

where $\vec{L}_{xy} = \vec{R}_{Transverse}(SecVertex) - \vec{R}_{Transverse}(PrimVertex)$ is the projection in the xy plane of the vector connecting primary and secondary vertex. This definition has the advantage not to require informations on the z components of the impulse and, more

[3]It is helpful for the rest of the discussion to briefly derive this formula. Lets τ be the mean life in the particle frame of reference, in the laboratory frame of reference the observed mean life is $\gamma\tau$, the decay length is then $L = v\gamma\tau = \beta\gamma c\tau$, then $c\tau = \frac{L}{\beta\gamma} = L_{xy} \cdot \frac{1}{(\beta\gamma)_T} = L_{xy} \cdot \frac{M}{P_T}$. Rewriting this last equation as $c\tau = \frac{\vec{L}_{xy} \cdot \vec{P}_T M}{P_T^2}$ the formula gains an higher capability in rejecting background, while it keeps the same efficiency for the signal, because it requires the coincidence between the two direction $\vec{L}_{xy}$ and $\vec{P}_T$ in order to be positive.

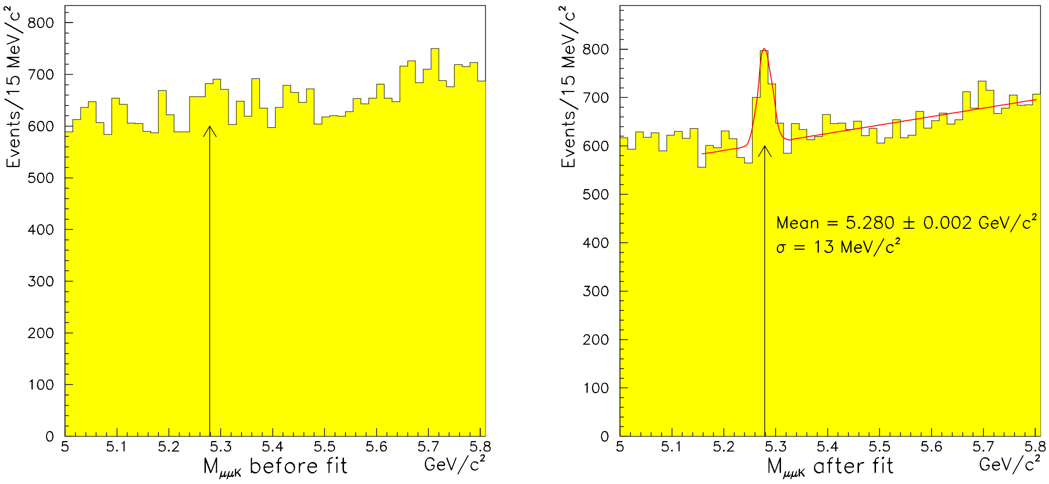

Figure 6.6: *$M_{\mu\mu K}$ invariant mass before and after the kinematic fit on data. The resolution improvement highlights a signal barely visible before the fit.*

important, on the z coordinates of the primary and secondary vertexes; in fact we remind that the SVX vertex microstrip detector carries out measurements only in the transverse plane.

6.4.1 $c\tau$ factorization

After all this it is important to keep in mind the strategy we adopted for the analysis; the comparison between two channels $B_s \to J/\psi\eta$ and $B^\pm \to J/\psi K^\pm$ in order to extract the *branching ratio* $\mathcal{B}(J/\psi \to \mu\mu)$. For this reason it is helpful to consider again the equation $c\tau = \frac{L_{xy}}{(\beta\gamma)_T}$. This formula highlights two potential contributions to the error on the flight distance measurement. The first one is connected to the resolution on the position in the primary vertex, reconstructed by means of the position of the beam line, and on the secondary vertex, reconstructed by means of the kinematic fit to the J/ψ muons. The second source of error derive from the P_T of the reconstructed B meson.
The resolution on the L_{xy} is expected to be the same in the two channels since the reconstruction algorithms of the primary and secondary vertexes are identical. The Monte Carlo simulation in fact provides a resolution of about 1 μm for both channels.
The situation for the second quantity, the P_T, is totally different. In the case of the $B_s \to J/\psi\eta$ channel the meson is reconstructed by means of the 4 particles $\mu\mu\gamma\gamma$, two of them (the photons) with a limited momentum resolution ($\sigma(E)/E \simeq 13.5\%/\sqrt{E_T}$); instead in the channel $B^\pm \to J/\psi K^\pm$ the meson is reconstructed by 3 charged tracks detected in the CTC which provide an accurate measurement of the $B^\pm$ mass and momentum. The presence of the two contributions is highlighted by the equation [5]:

$$\frac{\sigma_\tau}{\tau_B} = \sqrt{\left(\frac{\Delta L^B_{xy}}{L^0_{xy}}\right)^2 + \left(\frac{\tau}{\tau_B}\frac{\Delta P_T}{P_T}\right)^2} \qquad \text{where} \qquad L^0_{xy} = P_T/m_B \cdot c\tau_B$$

Figure 6.8 shows the absolute P_T resolutions for the two channels.

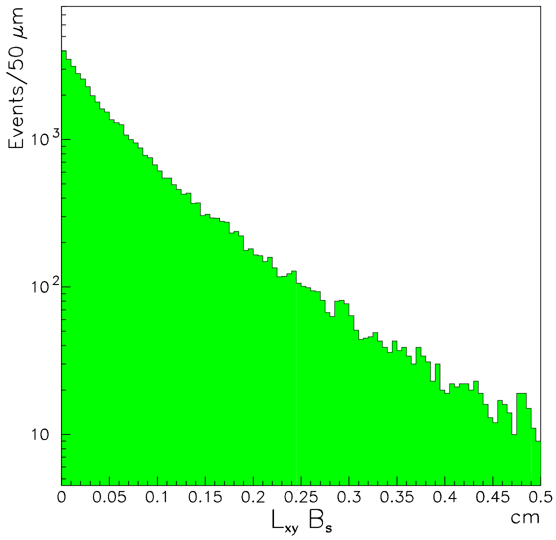

Figure 6.7: *L_{xy} distribution for the $B_s \to J/\psi\eta$ channel evaluated as the projection in the xy plane of the distance between the primary and secondary vertexes. The Monte Carlo dataset used is the one obtained with the* BGENERATOR *Monte Carlo.*

We nevertheless have to underline that the Monte Carlo simulation which showed the analogies and the differences in resolution for the variables L_{xy} and P_T in the two channels provides an expected resolution for the variable $c\tau$ that is substantially equal for the B_s and the $B^{\pm}$. This is because the contribution to the error on the $c\tau$ due to the L_{xy} estimate is dominant.
For the prosecution we have conservatively chosen to adopt a variable not potentially prone to problems of different resolution and that meanwhile maintains the $c\tau$ structure defined below.

6.4.2 $c\tau^*(J/\psi)$

In the previous section we highlighted the characteristics of the $c\tau(B)$ variable that could present difficulties when we apply a cut on this quantity and we evaluate the relative efficiency for the two channels $B_s \to J/\psi\eta$ and $B^{\pm} \to J/\psi K^{\pm}$.
The solution we adopted to avoid this problem is to define a new variable, which will be indicated with $c\tau^*(J/\psi)$ or simply with $c\tau^*$, in this way:

$$c\tau^*(J/\psi) = \frac{\vec{L}_{xy} \cdot \vec{P}_T(J/\psi) M_{J/\psi}}{P_T^2(J/\psi)}$$

It is evident that this quantity uses informations provided exclusively by the J/ψ reconstruction, so it keeps the same behavior in the two channels. Figure 6.9 shows the distribution for this variable for the data and for the $B_s \to J/\psi\eta$ BGENERATOR Monte Carlo.

An objection can be raised to the given definition of the $c\tau^*$ variable; the two formulas $c\tau^*(J/\psi) = \frac{\vec{L}_{xy} \cdot \vec{P}_T(J/\psi) M_{J/\psi}}{P_T^2(J/\psi)}$ and $c\tau'(J/\psi) = \frac{L_{xy} M_{J/\psi}}{P_T(J/\psi)}$ does not have the same behavior on

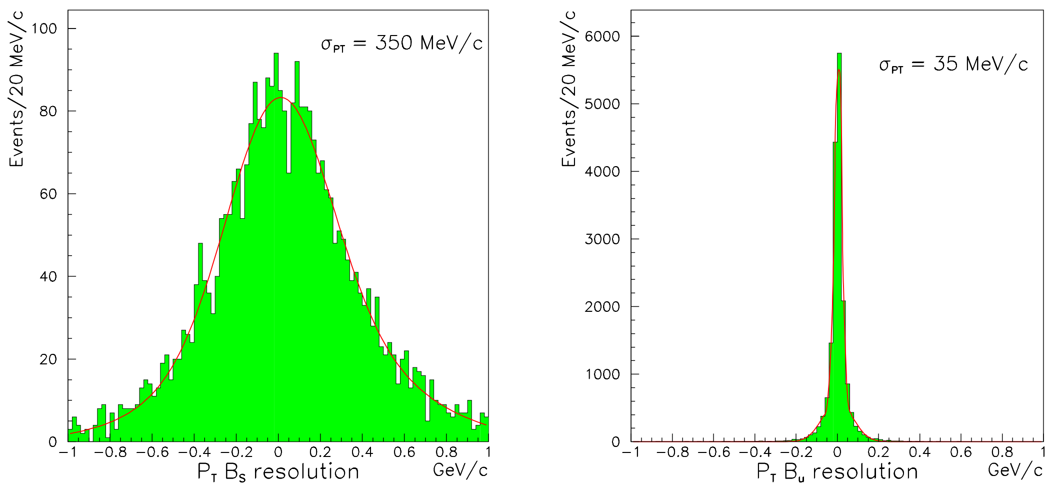

Figure 6.8: *Absolute resolutions for the $P_T(B)$. The resolution has been evaluated comparing the P_T variable before (generator banks) and after the simulation and reconstruction in the Monte Carlo datasets generated by* BGENERATOR. *The resolution of the $\mu\mu\gamma\gamma$ system (left) is one order of magnitude lower than the $\mu\mu K$ one (right).*

the signal, since the term $\vec{L}_{xy}$ keeps the direction of the B meson, while $\vec{P}_T(J/\psi)$ keeps the J/ψ direction, and then differs from the first one. Comparing these two quantities in the BGENERATOR Monte Carlo dataset for the $B_s \to J/\psi\eta$ channel (looking at the generator banks) we see that the relative difference is on average close to 1% and almost always lower than 5% (figure 6.10); since the measurement errors on L_{xy} are one order of magnitude larger with respect to the average, this systematic underestimate can be neglected[4]. After having defined the variable we still have to decide the value where to cut, the study for the optimization will be described in the next chapter. Figure 6.11 shows the relation between $c\tau^*(J/\psi)$ and $c\tau(B)$ for the $B_s \to J/\psi\eta$ Monte Carlo dataset and suggests to choose a cut at 90 μm in analogy with the cut at 100 μm on the variable $c\tau(B)$. The same request has been applied to the reference channel $B^\pm \to J/\psi K^\pm$.

6.4.3 Other kinematic requests

Cut on J/ψ P_T

The comparison between the two graphs in figure 6.9 highlights how the $c\tau$ (or $c\tau^*$) variable is helpful to discriminate the decay process of the B meson with respect to the $p\overline{p}$ background events.

A second variable that can lead to a considerable gain in terms of S/N ratio is the transverse momentum of the B candidate. This is confirmed by comparing the P_T spectra for the B_s meson candidates; the signal presents an average transverse momentum higher than the combinatorial background (figure 6.12).

Nevertheless the discussion developed in 6.4.1 and the figure 6.8 suggest that cutting on this variable in both the channels $B_s \to J/\psi\eta$ and $B^\pm \to J/\psi K^\pm$ can lead to troubles

[4]For the channel $B^\pm \to J/\psi K^\pm$ the relative difference is even lower.

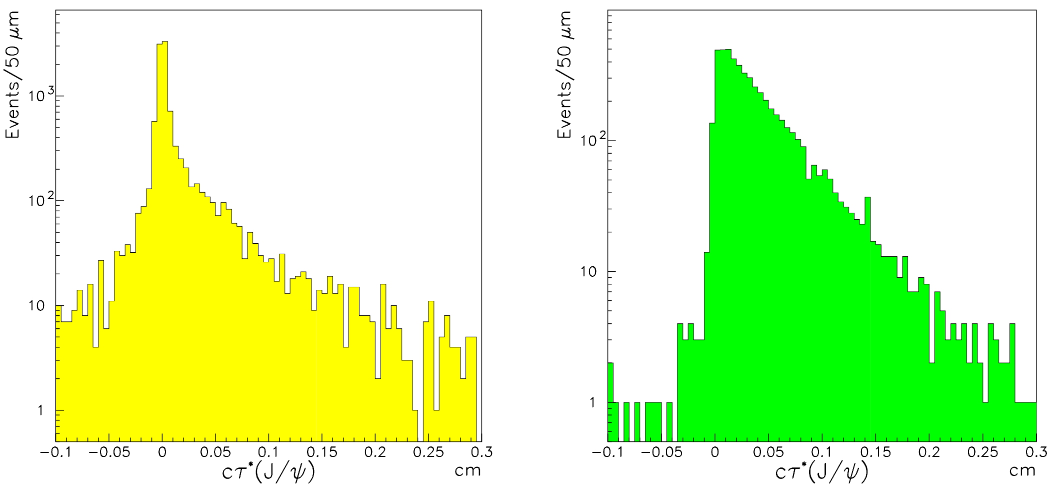

Figure 6.9: *$c\tau^*(J/\psi)$ distributions for data and* BGENERATOR *Monte Carlo. In data there is an consistent set of* prompt *J/ψs. The $c\tau^*$ variable is then a helpful tool to reject background.*

in evaluating the relative efficiencies due to the consistent difference in resolution in the two cases. The natural candidate to substitute the $P_T(B_s)$ variable is obviously the J/ψ transverse momentum, which, being reconstructed from the muon pairs, is exempt from this problem.

The optimization of the cut on this quantity is presented in the next chapter; meanwhile we applied a preliminary cut at $P_T(J/\psi) > 5.0$ GeV/c which correspond approximatively to require $P_T(B) > 6.0$ GeV/c, as it has been done for the reference channel in [2].

After having applied the cuts $c\tau^*(J/\psi) > 90$ μm and $P_T(J/\psi) > 5.0$ GeV/c the invariant mass distributions appear to be depleted in statistics. We observe an evident increase in terms of S/N ratio for the reference channel $B^\pm \to J/\psi K^\pm$, while there is no evidence of signal for the B_s. Figure 6.13 presents these two distributions after the kinematic fit. Figure 6.14 shows the mass distribution for the $B_s \to J/\psi\eta$ dataset generated with BGENERATOR.

B meson isolation

One of the characteristic of the B meson fragmentation is to keep a large fraction of the initial momentum of the parent b quark. This lead to a lack of relevant momentum particles inside a cone centered in the J/ψ direction. This peculiarity allows to introduce variables able to discriminate b particles with respect to background due to fragmentation products, multiple interaction, and the *underlying event*. These variables have been studied at CDF [6] in various channels involving B mesons. One of these is our reference channel $B^\pm \to J/\psi K^\pm$.

The quantity we want to consider can be defined as "B P_T isolation". In order to define this variable we consider a cone with opening equal to $\Delta R = \sqrt{\Delta\eta^2 + \Delta\phi^2} = 1.0$ and centered on the B meson propagation direction, we then select all the tracks contained in

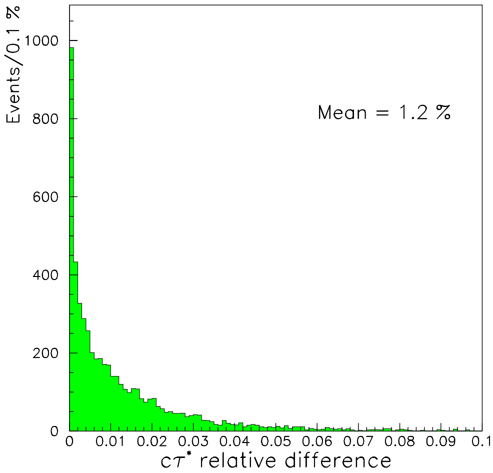

Figure 6.10: *Relative difference* $\frac{c\tau' - c\tau^*}{c\tau'}$ *for the* J/ψ *decay length in the* $B_s \to J/\psi\eta$ *channel.*

this cone, not produced in the B decay and originated from the same primary interaction[5]. If $P_T(B)$ and $P_T(i)$ are the momenta of the B meson and of the i-th track respectively and $\sum_i^{cone} P_T(i)$ is the scalar sum of transverse momenta of the particle contained in the cone, then

$$I_{P_T}(B) = \frac{P_T(B)}{P_T(B) + \sum_i^{cone} P_T(i)}$$

provides a measurement of the presence of extra tracks in proximity of the B. Figure 6.15 presents the $\mu\mu K$ invariant mass spectrum after the kinematic fit and after applying an additional cut $I_{P_T}(B) > 0.7$ in the $B^{\pm} \to J/\psi K^{\pm}$ channel. The efficiency of this request is then around 74%, in good agreement with the study in in [6] ($72.9 \pm 4.6\%$), while the background is suppressed almost by a factor 3.

The effectiveness of this cut in increasing the S/N ratio for the reference channel is the substantial.

As regards the $B_s \to J/\psi\eta$ channel the situation is more complicated. In the mass spectrum there is no evidence of signal and there are no isolation studies on this meson. Even if there are no theoretical reasons to consider the two fragmentation processes as different, still the estimate of the efficiency for this cut on the B_s cannot be simply taken from the $B^{\pm}$ one. Besides, we cannot rely on the Monte Carlo to simulate the tracks not coming from the B meson decay. A way to solve this problem is to fully reconstruct a B_s channel as, for instance, $B_s \to J/\psi\phi$ with $\phi \to K^+K^-$ and then study on this channel the isolation cut. Following this idea we have been able to reconstruct a B_s signal to be used for the study, even without optimizing the selections. In table 6.1 we present the selections applied.

The four track present in the final state have been fitted with a *vertex constrained* kinematic fit (`CTVMFT`) with the additional request that the two μ have the invariant mass equal to $M_{J/\psi}$. No other request has been applied to the invariant mass of the K

[5]This is guaranteed by the request that for the track $|z_0 - z_B| < 5$ cm, where z_0 and z_B stand for the z coordinate of the point of minimum approach of the detector track respectively for the track and for the B meson.

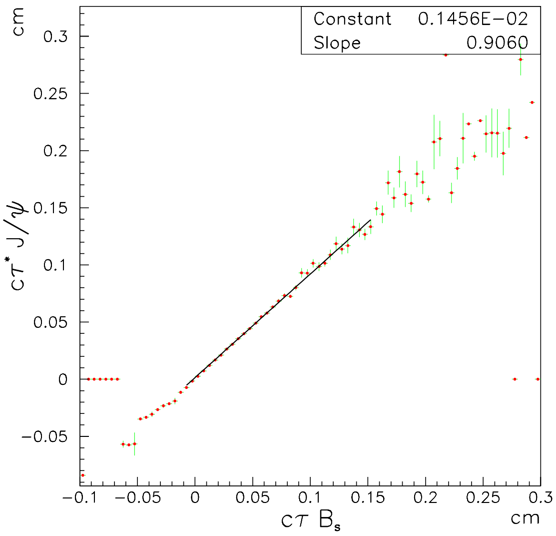

Figure 6.11: *Relation between $c\tau(B)$ and $c\tau^*(J/\psi)$; this distribution suggest to apply a preliminary cut at 90 μm in analogy with a cut at 100 μm on the variable $c\tau(B)$.*

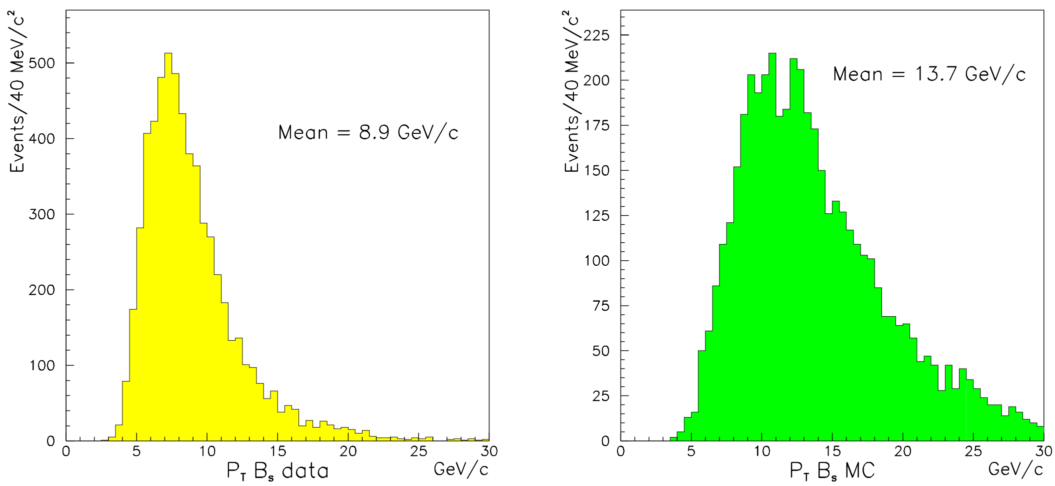

Figure 6.12: *$P_T(B_s)$ distributions for data and Monte Carlo.*

candidates. We then applied an isolation cut $I_{P_T}(B_s) > 0.7$, in analogy with the one applied on $B^\pm \to J/\psi K^\pm$ and we evaluated the efficiency to be equal to 0.57 ± 0.09 (see figure 6.16).
This estimate appears to be significantly lower than the one obtained on the reference channel. This discrepancy could be related to the poor statistics available on the $B_s \to J/\psi\phi$ channel, nevertheless in absence of other checks we decided not to use this cut.

6.4.4 Definition of mass windows for J/ψ, η, and B_s

In general, in order to optimize the search of a gaussian signal in a invariant mass spectrum with the presence of background processes, we can show that the most effective cut for a counting experiment, i.e. the one which maximizes the ratio $S/\sqrt{N}$, is given by the

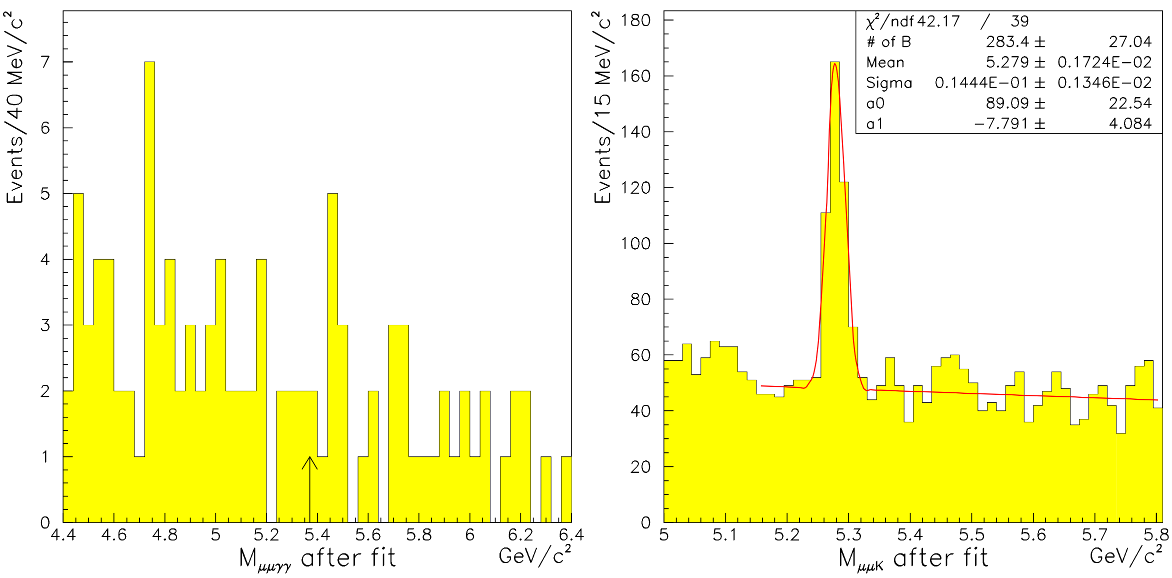

Figure 6.13: *Invariant mass distribution for the two channels, $B_s \to J/\psi\eta$ on the left and $B^{\pm} \to J/\psi K^{\pm}$ on the right after the cuts $c\tau^*(J/\psi) > 90\mu m$ and $P_T(J/\psi) > 5.0$* GeV/c. *The curve interpolating the signal is a gaussian, while the background has been fitted with a linear shape; the interpolation region has been limited to values higher than 5.15* GeV/c^2, *as suggested in [2], in order to avoid the overestimate of the combinatorial background.*

Selection cuts on $B_s \to J/\psi\phi$	
muons	both in SVX
$P_T(K)$	$> 0.6\,$GeV/c
Prob($\chi^2(J/\psi)$)	$> 0.1\%$
$P_T(\phi)$	$> 1.5\,$GeV/c
$P_T(B_s)$	$> 6.0\,$GeV/c
c$\tau(B_s)$	$> 50\mu m$
Prob($\chi^2(B_s)$)	$> 0.1\%$

Table 6.1: *Selections applied to highlight the $B_s \to J/\psi\phi$ signal for the B_s isolation study.*

request $|M_{meas} - \overline{M}| < 1.4\ \sigma_{meas}$, where M_{meas} and σ_{meas} we indicate the reconstructed value for the particle mass and the experimental resolution on M_{meas}, and with $\overline{M}$ the mean value of M_{meas}; this is true if the background shows a smooth distribution. In fact, the not perfect calibration of the detectors and the presence of systematic effects can make $\overline{M}$ not to be exactly coincident with the true value of the mass resonance; we than will consider an optimized cut that take into account these possible shifts.

The mass resolution for the reconstructed J/ψ mesons in the data is equal to about 20 MeV/c^2, as shown in figure 4.7. Since there are no significant systematic effects (the correct mass value is $M_{J/\psi} = 3097$ MeV/c^2[3] and $\overline{M} = 3094.1 \pm 0.1\,$MeV/c^2) in this case the mass window $|M_{mis} - 3.097| < 30$ MeV/c^2 seems to be appropriate for our goals. The efficiency of this cut can in first approximation be considered equal to the J/ψ mesons produced from the B_s and $B^{\pm}$ decays; residual effects will be absorbed in a k factor, discussed in section 7.2.5.

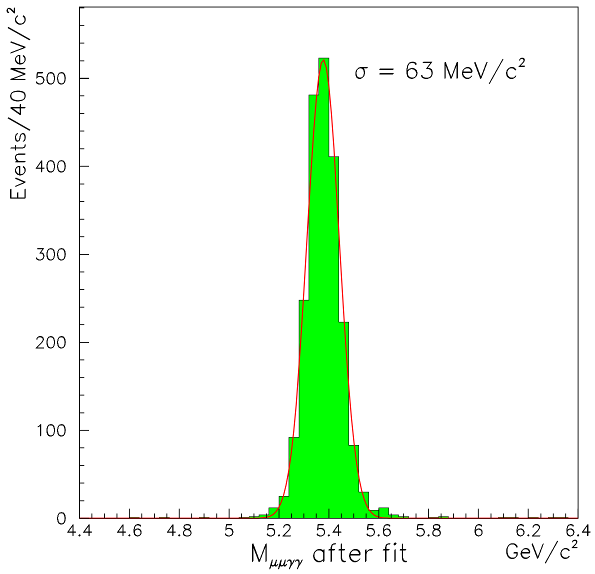

Figure 6.14: *Invariant mass distribution for the $B_s \to J/\psi\eta$ Monte Carlo after the cuts $c\tau^*(J/\psi) > 90\mu m$ and $P_T(J/\psi) > 5.0$ GeV/c.*

Regarding the η meson, we cannot measure directly the experimental mass resolution, since there is no signal evidence in the two photon invariant mass spectrum after the analysis selections. Nevertheless figure 5.16 showed, with different selections, the presence of an evident signal; the width and position of the peak are respectively equal to 57 ± 12 MeV/c^2 and to 550 ± 14 MeV/c^2: the absence of a significant scale error in the photon energy measurement is suggested both by the agreement between the reconstructed mass and the nominal value of M_η, both by the agreement, again observed in figure 5.16, between the π^0 reconstructed mass and the nominal one. The use of the mean value and the width obtained in the data is not a straightforward ad safe procedure, since in principle the different selections applied (in particular the isolation cut on photons) can modify the observed signal. However we are reassured by the good compatibility of the measured values with the ones predicted by the simulation, which provides for the signal a gaussian distribution of 46 MeV/c^2 width, well centered on the nominal value of $M_\eta = 547$ MeV/c^2 (see figure 5.17). In this conditions we chose as mass window for the η signal search the interval $|M_{\gamma\gamma} - 547| < 80$ MeV/c^2. The efficiency of this request corresponds to an efficiency of $\epsilon_{M_\eta} = 0.860 \pm 0.007$ as evaluated by the simulation. To this value we assign a systematic error equal to the difference between the efficiency obtained using the experimental values of mass and width observed in figure 5.16: $\epsilon_{M_\eta} = 0.860 \pm 0.007 \pm 0.051$.

As regards the B_s meson there is no direct measurement of the experimental width and of the invariant mass M_{B_s} obtained by muon momentum measurements and photon reconstruction in the CDF detector, then we have to resort to the simulation. It's worthwhile to notice how a (possible) error on the measured energy scale of the photons is strongly reduced by the kinematic fit, which constrains their invariant mass to the correct nominal value. Figure 6.14 shows a reconstructed width on the Monte Carlo, after the kinematic fit, equal to 63 MeV/c^2; it is then reasonable to accept as B_s candidates those with $|M_{B_s} - 5.37| < 0.09$ GeV/c^2. This request has an efficiency of $\epsilon_{M_{B_s}} = 0.820 \pm 0.009$.

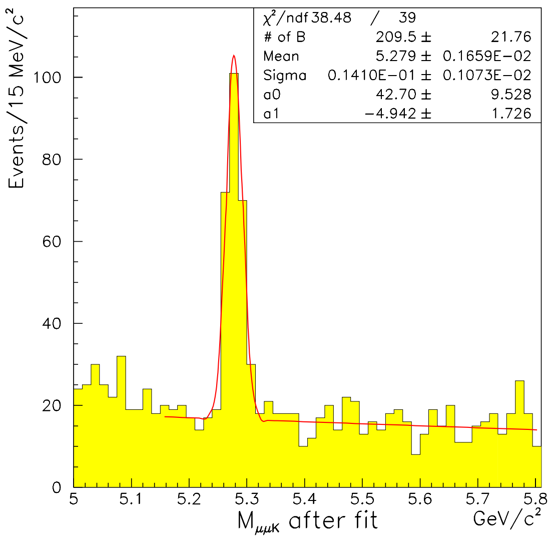

Figure 6.15: *Invariant mass distribution for the reference channel after the additional isolation cut $I(B) > 0.7$.*

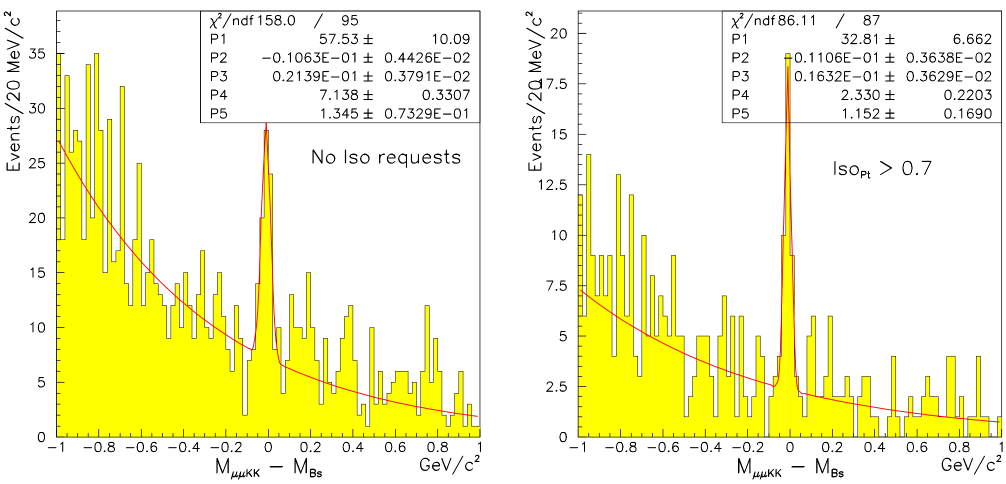

Figure 6.16: *B_s invariant mass in the $B_s \to J/\psi\phi$ channel after P_T isolation. The function interpolating the background is an exponential, for the signal we use a gaussian. Since the signal is concentrated in just 4 bins we used the fit only for the background estimation, while the signal has been evaluated counting the events over background in the four bins around the B_s mass. The parameter p_4 gives the background per bin.*

Bibliography

[1] P. Avery, "Applied Fitting Theory I, General Least Squares Theory", *CBX 91 - 72*, (Oct 1991)

[2] D. Acosta *et al.* (CDF Collaboration), "Measurement of the B^+ Total Cross Section and B^+ Differential Cross Section $d\sigma/dp_T$ in p$\overline{\text{p}}$ Collisions at $\sqrt{s} = 1.8$ TeV", *Phys. Rev. D* **65**, 052005 (2002)
T. A. Keaffaber, M. W. Bailey, D. Bortoletto, A. F. Garfinkel, A. T. Laasanen, J. D. Lewis, S. Tkaczyk, "Measurement of the B^+ Total Cross Section and B^+ Differential Cross Section $d\sigma/dp_T$ in p$\overline{\text{p}}$ Collisions at $\sqrt{s} = 1.8$ TeV",
CDF internal note **5608**, (Jun 2001)
See also:
CDF internal note **3634**, (Apr 1996)
CDF internal note **2892**, (Nov 1994)
CDF internal note **2516**, (Mar 1994)

[3] A. Warburton, "Run 1A and 1B Low-p_T Single- and Double-track CTC Pattern Recognition Efficiencies", **CDF** internal note **4139**, (Jun 1997)

[4] K. Hagiwara *et al.*, "Review of Particle Physics", *Phys. Rev. D* **66**, 010001 (2002)

[5] M. Paulini, "B lifetimes, mixing and CP violation at CDF". *Int. J. Mod. Phys. A*, **10**, 1990 (1999) hep-ex/9903002.

[6] G. Bauer, J. Friedman, K. Kelly, B. Mattingly, T. Shah, P. Sphicas, "A Study of the Isolation of B-Mesons", **CDF** internal note **2765**, (Oct 1994) **CDF** internal note **3684**, (May 1996)

Chapter 7

BR measurement

7.1 Introduction

As seen in the previous chapter, there is no evidence of a B_s signal in the invariant mass spectrum of the selected events after the kinematic fit. Thus we will use the obtained results to extract a limit on the *branching ratio* for the $B_s \to J/\psi\eta$ decay. However the absence of a signal was expected since the theoretical predictions on the *branching ratio* for the searched decay ($\mathcal{B} \sim 9 \times 10^{-4}$[4]) indicate the presence, in the J/ψ dataset, of some hundreds signal events, at the trigger level. *A priori*, the signal absence in the mass spectrum for the available data was expected especially considering the inefficiency of the identification algorithms for low energy photons originating from the η meson decay. This observation is important since it allows to use the negative result on the search for the extraction of an upper limit on the number of $B_s \to J/\psi\eta$ events: it means that the limit extraction procedure is free from the methodological problem of deciding *a posteriori* how to use the experimental result, i.e. if to measure a cross section in case of observation of a significant signal or, to extract a limit.

The ingredients for the limit extractions have been discussed in the previous chapters. What we still have to do now is the optimization of the kinematic variables $c\tau^*$ and P_T of the J/ψ meson, that we showed to be helpful in discriminating the B_s signal from the background processes. In calculating the limit to the *branching ratio* we will make use, as much as possible, of the cancellation of many sources of systematic errors, writing its expression as follows:

$$\mathcal{B}(B_s \to J/\psi\eta) \leq k \frac{f_u}{f_s} \frac{N^{90\%}}{N_{J/\psi K}} \frac{\mathcal{B}(B_u \to J/\psi K)}{\mathcal{B}(\eta \to \gamma\gamma)} \frac{\epsilon_K}{\epsilon_{\gamma\gamma}}$$

where f_u and f_s are the fractions of b quarks hadronizing to $B^\pm$ and B_s mesons, $N^{90\%}$ is the limit at 90% of C.L. on the number of $B_s \to J/\psi\eta$ events in the dataset, $N_{J/\psi K}$ is the number of $B_u \to J/\psi K$ observed decays, ϵ_K is the detection efficiency for the K meson associated to the J/ψ on the search for the $B^\pm$ signal, $\epsilon_{\gamma\gamma}$ the efficiency on detecting the two photons of the B_s decay chain, $\mathcal{B}(B_u \to J/\psi K)$ is the *branching ratio* of the reference process, and $\mathcal{B}(\eta \to \gamma\gamma)$ the fraction of η mesons decaying in two photons; finally with k we summarize the effects of non complete cancellation between the efficiencies for the J/ψ originated from the B_s and the $B^\pm$ decays and to other differences in handling the two signals.

Between the quantities just described, the yet known values are:

- The fragmentation ratio to B_s and $B^{\pm}$ of the b quark is assumed to be $f_u/f_s = 2.34 \pm 0.38$, as measured by CDF [1] (but we consider also the possibility to use the value $f_u/f_s = 4.31 \pm 0.54$ which is the result of the LEP WG analysis [2]);
- for the quantity $\mathcal{B}(B_u \to J/\psi K)$ we adopt the world average [3], equal to $(1.01 \pm 0.05) \times 10^{-3}$;
- $\mathcal{B}(\eta \to \gamma\gamma) = 0.3943 \pm 0.0026$[3].

The quantities described and measured in chapters 5 and 6 are the following:

- $\epsilon_K = 0.452 \pm 0.016$;
- $\epsilon_{\gamma\gamma} = 0.0288 \pm 0.0025$;
- $N_{B_u} = 288.5 \pm 28.5$;

The factor k will be discussed in 7.2.5 and takes the value:

- $k = 0.914 \pm 0.077$.

Finally we have to consider also the efficiencies of the cuts on the mass windows of the η and B_s mesons described in section 6.4.4:

- the cut $|M_{\gamma\gamma} - 547| < 80$ MeV/c^2 has an efficiency equal to $\epsilon_\eta = 0.860 \pm 0.051$;
- the cut $|M_{B_s} - 5.37| < 0.09$ GeV/c^2 has an estimated efficiency equal to $\epsilon_{M_{B_s}} = 0.820 \pm 0.009$.

Now we have only to determine the upper limit on the number of decays $B_s \to J/\psi\eta$ on the dataset, $N^{90\%}$, after all the kinematic cuts. Finally the k factor will be calculated after the cut optimization on the J/ψ meson.

7.2 Extracting an upper limit on the *branching ratio*

7.2.1 Introduction

The invariant mass spectrum of the B_s candidates, reconstructed by means of the kinematic fit discussed in 6.2, has been shown in figure 6.13 after reasonable, but not optimized, cuts on the reconstructed $c\tau^*$ ($c\tau^* > 90\mu m$) and on the P_T of the J/ψ meson ($P_T > 5$ GeV/c). This spectrum does not present any indication of an excess of events that can be attributed to the $B_s \to J/\psi\eta$ decay in correspondence to the known value of the B_s meson mass $M_{B_s} = 5.37$ GeV/c^2 [3].

The extraction of the upper limit on the number of events for a searched process can be based on various methods. The main differences between them are on the statistical approach (Bayesian or frequentistic) and on the choice on how to handle the background. Although the problem of extracting a limit is quite general, since it is strictly connected to the idea of confidence interval –which is the quantity normally used to assign an error

to the experimental measurements–, there is a wide range of views on what recipe gives the most appropriate solution. At first the problem has been faced by Neyman[5], who provided a general structure still used in the simplest situations. Recently some disputes raised about the correctness of the Neyman procedure, especially in the cases of extraction of upper limits when the probability of obtaining an experimental result with parameters out of physical boundaries is not negligible.
The different views on how to handle coherently these situations are related mainly to the Bayesian or frequentistic approach, which are based on different assumptions for the formulation of a method which unambiguously defines the confidence interval, and which lead to different results, mainly in case of Poisson's processes with background, as the one we are studying.

The Bayesian approach to probability is not based on relative frequency, and is suitable to be used on experiments that cannot be repeated. Moreover it easily allows to incorporate further informations on the field of existence of the parameters: in fact it requires the *a priori* distributions of the variables on evaluation, distributions that contain all the known informations before the experiment. The main limitation on the Bayesian method is just on the fact that cannot provide a result without some *a priori* assumption. For reproducible experiments that want to estimate, without using preceding informations, quantities that are far from a non physical region –or that have all the real numbers as field of existence– the frequentist approach is probably the most adequate.

7.2.2 POILIM: the method used at CDF

CDF collaboration published several results on new particle searches or on rare decays, providing upper limits to the cross sections of these processes, using a frequentistic technique which includes the estimation of the uncertainty on the number of background events and on the signal acceptance on the calculation of the *confidence level*. The literature presents several proposals on how to treat each of these effects on the limit calculations [6, 7, 8, 9], but nobody rigorously treated both of them together.

The technique adopted at CDF, implemented in an algorithm called POILIM [10], is frequentistic but uses the Bayesian notion of probability density for the unknown value of the expected background and of the acceptance.

Given the number of observed events n_0, the probability of observing n_0 depends on the average number μ of events expected from the Poisson distribution:

$$P(n_0; \mu) = \frac{\mu^{n_0} e^{-\mu}}{n_0!}.$$

The determination of the μ, given a n_0 consistent with zero, becomes the problem of extracting an upper limit N on the number of expected events for which there is a probability equal to ϵ to observe n_0 or less events. The *confidence level* (C.L.) of the upper limit is then $1 - \epsilon$. Operatively, in order to calculate N given ϵ (usually chosen equal to 0.1, and then the limit is at 90% of C.L.) we vary μ until we find the searched value for ϵ, i.e. $N = \mu|_\epsilon = 0.1$.

In case we expect the presence of μ_B events due to background processes in the final set of events , this can be taken into account by calculating N as the value of μ_S (events due to the searched signal) for which there is a 90% probability that an experiment similar to the one really performed collects more than n_0 events, and among them there are not more than n_0 background events. N can be then calculated with the same procedure described for the case $\mu_B = 0$. Nevertheless in practice the value μ_B is not known with absolute precision and, moreover, the uncertainty on the acceptance for the searched process complicates the extraction of the limit on the *branching ratio* from the observed N value. Both the uncertainties can be included in the limit by calculating the N value such that:

$$\epsilon = \frac{\sum_{n=0}^{n_0} \frac{1}{\sqrt{2\pi\sigma_N^2}} \int_0^\infty \int_0^\infty P(n;\mu'_B+\mu'_S) e^{-\frac{(\mu_B-\mu'_B)^2}{2\sigma_B^2}} e^{-\frac{(N-\mu'_S)^2}{2\sigma_N^2}} d\mu'_B d\mu'_S}{\sum_{n=0}^{n_0} \int_0^\infty P(n;\mu_B) e^{-\frac{(\mu_B-\mu'_B)^2}{2\sigma_B^2}} d\mu'_B}$$

where $\sigma_N = N\sigma_A/A$, while A and σ_A are the acceptance and its error. This is true if we assume an *a priori* gaussian distribution for μ_S and μ_B around values found in other studies, with the width given by their uncertainties. Since we are using *a priori* distributions, the method is based on Bayesian techniques. Nevertheless the method is an hybrid since the determination of the solution to the complex equation just written is performed by means of a large number of pseudo-experiments: in each pseudo-experiment we vary the true value of the number of signal and background events relying on the probability density assumed, and the value of N is evaluated in a frequentistic way as the fraction of experiment for which the signal plus background exceed the observed number n_0.

7.2.3 Optimization of the cuts on J/ψ meson

In order to obtain the best limit on the *branching ratio* $\mathcal{B}(B_s \to J/\psi\eta)$ we can search the combination of cuts on the kinematic variables producing the best expectation value on the ratio $N_{B_s}^{90\%}/\epsilon_{\gamma\gamma}$, where $\epsilon_{\gamma\gamma}$ represents the efficiency of specific cuts to select the meson η and $N_{B_s}^{90\%}$ is the upper limit on the number of events for the process $B_s \to J/\psi\eta$. This come out from the analysis of the following formula

$$\mathcal{B}(B_s \to J/\psi\eta) \leq k \, \frac{N_{B_s}^{90\%}}{N_{B_u\to J/\psi K}} \times \frac{f_u}{f_s} \times \frac{\mathcal{B}(J/\psi K)}{\mathcal{B}(\eta\to\gamma\gamma)} \times \frac{\epsilon_K}{\epsilon_{\gamma\gamma}}.$$

This imply the assumption that (true as a first approximation) the relative error on the ratio N_{B_u}/ϵ_K is the value of the cuts to optimize. The optimization method we adopted determines the set of cut values $\vec{\alpha} = (\alpha_1, \alpha_2, ...)$ on the chosen variables such that the expectation value of the limit on the *branching ratio* of the searched decay is minimum. In order to obtain the limit with the `POILIM` program we need a determination on the absolute number of expected background events and a value of the efficiency for the signal, for each value of $\vec{\alpha}$. After that we can calculate for each $\vec{\alpha}$ the expectation value for the limit on the *branching ratio* starting from the expectation value on the number of events $N^{90\%}$ attributed to the searched process, with a background equal to $N_B \pm \sigma_{N_B}$. More explicitly, given $\vec{\alpha}$ we will determine the corresponding value of $N_B \pm \sigma_{N_B}$, and from this the probability distribution on the expected events in an experiment, $\mathcal{P}(N_{obs}|N_B \pm \sigma_{N_B})$; each possible value N_{obs} of observed events determines a different $N^{90\%}(N_{obs})$, and then the expectation value on the limit, $< N^{90\%} > |_{\vec{\alpha}}$, can be simply calculated as weighted average.

$$< N^{90\%} > |_{\vec{\alpha}} = \sum_{N_{obs}=0}^{\infty} \mathcal{P}(N_{obs}|N_B \pm \sigma_{N_B}) \times N^{90\%}(N_{obs}).$$

This implies the execution of the program `POILIM` several tens of time for each chosen $\vec{\alpha}$, after having determined the true corresponding distribution of $\mathcal{P}(N_{obs})$; $\mathcal{P}$ can be obtained choosing randomly a value N_B^* out from a gaussian distribution of N_B average and width σ_{N_B}, determining a Poisson distribution $P(N_B^*)$ with average value N_B^*, and repeating 10000 times the procedure:

$$\mathcal{P}(N_{obs}) = 10^{-4} \sum_{i=1}^{10000} \left(\frac{e^{-N_{B,i}^*} {N_{B,i}^*}^{N_{obs}}}{N_{obs}!}\right).$$

The calculation is time consuming, especially because `POILIM` converges very slowly when it receives large values as input for the number of observed events: in order to reduce the calculation time we decided to truncate the sum on the observed counts in the expression just wrote to the cases when N_{obs} satisfies $\mathcal{P}(N_{obs}) > 0.001$, this still guarantees a good approximation for our purposes.

7.2.4 Determinations of the expected background in the B_s window

In order to determine an estimate on the number of events not produced in the decay $B_s \to J/\psi\eta \to \mu\mu\gamma\gamma$ that satisfy all the cuts of the analysis, included the ones under optimization and the invariant mass windows cuts determined in section 6.4.4, we can use a standard and simple technique. Since the signal $B_s \to J/\psi\eta$ populates mainly the region $|M_{\gamma\gamma} - 0.547| < 0.08$ GeV/c^2 in the two photon invariant mass spectrum, and in the B_s mass spectrum the signal is reconstructed mainly in the region $|M_{B_s} - 5.37| < 0.09$ GeV/c^2, we consider the events *not* satisfying these requests for an estimation of the background events satisfying both of them.

Defining $\mathcal{A}$ as the set of events satisfying the cut on $M_{\gamma\gamma}$ and $\mathcal{B}$ the set satisfying the cut on M_{B_s}, we have that:

$$\mathcal{A} \bigcap \mathcal{B} = \frac{\overline{\mathcal{A}} \bigcap \mathcal{B}}{\overline{\mathcal{A}} \bigcap \overline{\mathcal{B}}} \times \mathcal{A} \bigcap \overline{\mathcal{B}}$$

This equation is valid, except for the statistical fluctuations, if there is no correlation between the reconstructed masses $M_{\gamma\gamma}$ and M_{B_s}. Obviously this condition is not strictly fulfilled since the positive correlation of the two quantities is implicit in the cinematic reconstruction. Nevertheless, in suitable mass intervals, including events with both higher and lower invariant masses, with respect to the true value, we expect the equivalence to be respected with good approximation.

It's worthy to notice that the presence of a J/ψ signal allows, in principle, an alternative determination of the background, using the ratio between events inside and outside the accepted mass window 6.4.4. We discarded this approach because of the limited number of events outside the region $|M_{\mu\mu} - 3.097| < 0.03$ GeV/c^2 that will cause a relevant statistical error in the background estimation.

We then define a set of experimental events to be used for the background estimation in the optimization of the kinematic cuts. The events will be selected by the following requests:

- $3067 < M_{\mu\mu} < 3127$ MeV/c^2;
- $397 < M_{\gamma\gamma} < 697$ MeV/c^2;
- $4500 < M_{B_s} < 6500$ MeV/c^2;
- $P_T^{J/\psi} > 4.0$ GeV/c;
- $c\tau^*_{J/\psi} > 0\mu m$;
- no selection on triggers.

So we will use also the events collected by other triggers beside the ones we chose. This will allow to optimize kinematic cuts without using the indirect knowledge on the number of background events for each set of cuts; otherwise we should "follow" the background fluctuations, i.e. choose the cut combination which produce the lowest background expectation –induced by statistic fluctuation of the sidebands– instead than choose the one *a priori* more promising. The background value obtained has then to be rescaled by a scale factor $F_{trig} = 0.69 \pm 0.07$, determined by the ratio between the number of J/ψ (events) contained in the set selected by the three triggers (after the cuts for photon identification, but before the cuts on the invariant mass) and the total number of J/ψ with no trigger request[1].

We can verify the precision of the method of background estimation before the cuts on the P_T and on reconstructed $c\tau^*$ of the J/ψ meson: we observe a total, before the selection of the triggers, of $N_{obs} = 23$ events with mass $467 < M_{\gamma\gamma} < 627$ MeV/c^2 and $5.28 < M_{B_s} < 5.46$ GeV/c^2, to be compared to an expectation of $N_{bgr} = 28.7 \pm 7.1$. Using the scale factor F_{trig} we can extrapolate an estimation of $N_{bgr\,sel} = 19.8 \pm 5.3$ for the events collected by the selected triggers, to be compared to $N_{obs} = 14$ observed events.

On the other hand, applying tough cuts on the two quantities we are studying, we still find a quite good agreement: requiring $P_T^{J/\psi} > 5.8$ GeV/c we find $N_{obs} = 13$ (9) events, to be compared with the estimation of $N_{bgr} = 14.6 \pm 4.7$ ($N_{bgr} F_{trig} = 10.1 \pm 3.41$) respectively for all the events and for only those accepted by the selected triggers. Applying a looser cut on the P_T variable and requiring instead $c\tau^*_{J/\psi} > 450\mu m$ we observe $N_{obs} = 5$ ($N_{obs} = 2$) events, with an estimation of $N_{bgr} = 3.2 \pm 2.4$ ($N_{bgr} = 2.2 \pm 1.7$), respectively with and without the selection on triggers.

As a first look to the selections on the two kinematic variables we explore a grid of 10×10 values: a cut on $c\tau^*$ varying between zero and 450 μm in 10 intervals of 50 μm and a cut on P_T between 4.0 and 5.8 GeV/c in 10 intervals of 0.2 GeV/c.

The results of this first investigation are presented in figure 7.1. It is evident that a cut on the variable $c\tau^*$ in the region between 50 and 200 μm increases the achievable limit on $\sigma_{B_s} \times \mathcal{B}(B_s \to J/\psi\eta) \times \mathcal{B}(\eta \to \gamma\gamma)$, while it seems not helpful to require for the J/ψ to have a P_T lower higher than 4 GeV/c, value that anyhow represents the lower limit for this quantity, due to the cut applied on the muon P_T ($P_T > 2$ GeV/c). In order to investigate more deeply the cut on the $c\tau^*$ variable, we fix the P_T cut and we scan the region between 0 and 500 μm in 100 5 μm intervals. The results are presented in figure 7.2. The optimum choice results to be $c\tau^*_{J/\psi} > 100\mu m$, for which we expect to observe a background equal to

[1]This number is in good agreement with the more precise determination of the total of J/ψ candidates before any selection on photons or on K mesons, $F_{trig} = 0.755 \pm 0.003\%$.

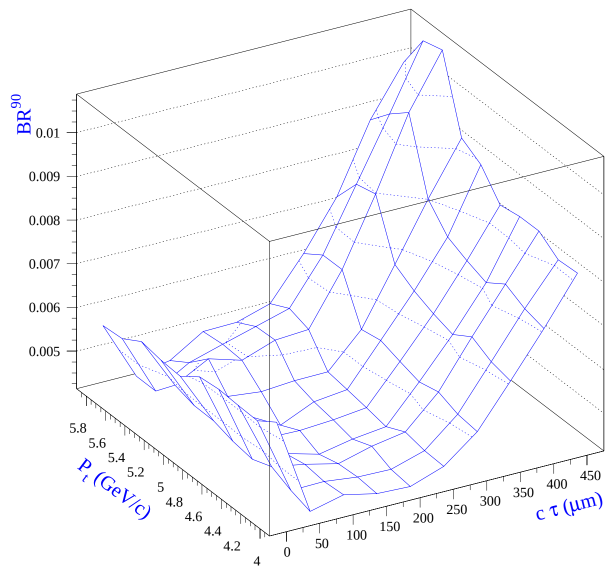

Figure 7.1: *Results of the preliminary study on the cuts on the variables* $c\tau^*_{J/\psi}$ *and* $P_T^{J/\psi}$. *We report, as a function of the cut on these variables, the expectation value on the limit at 90% on the* branching ratio $\mathcal{B}(B_s \to J/\psi\eta)$, *using the method described on the text.*

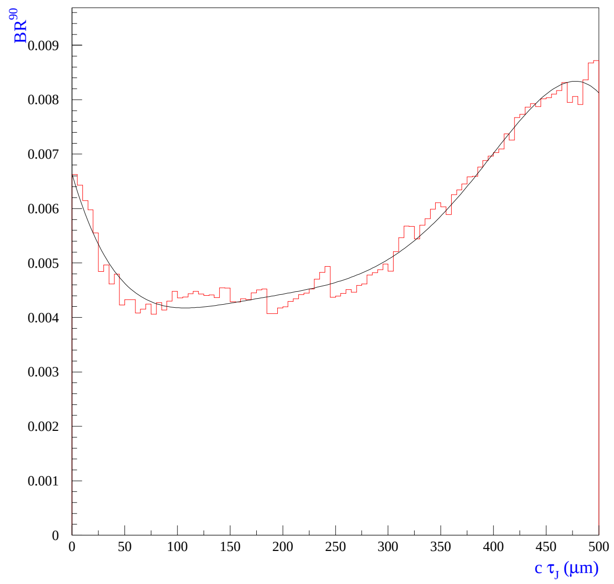

Figure 7.2: .
Study of the cut on the variable $c\tau^*_{J/\psi}$. *We report the estimate on the expectation value of the achievable limit at 90% of* confidence level *on the* branching ratio $\mathcal{B}(B_s \to J/\psi\eta)$ *as a function of the cut value on this variable. The superimposed curve is a polynomial fit, added only to guide the eye.*

$N_{bgr} = 4.86 \pm 2.43$ events after the request on the triggers. Assuming a total systematic error on the efficiencies equal to 30% (included in the calculation of the values shown in figure), the expectation value on the limit at 90% of *confidence level* results $N_{B_s}^{90\%} = 9.14$ events, which correspond approximately to $\mathcal{B}(B_s \to J/\psi\eta) < 4.2 \times 10^{-3}$.

Once we have accurately determined the optimum choice for the cut on $c\tau^*_{J/\psi}$, it is convenient to re-examine the value of the P_T cut. Once fixed $c\tau^*_{J/\psi} > 100\mu m$, we vary the request on the minimum J/ψ P_T in 100 intervals of 20 MeV/c between 4 and 6 GeV/c. The results are presented in figure 7.3. No evident minimum of the expectation value on

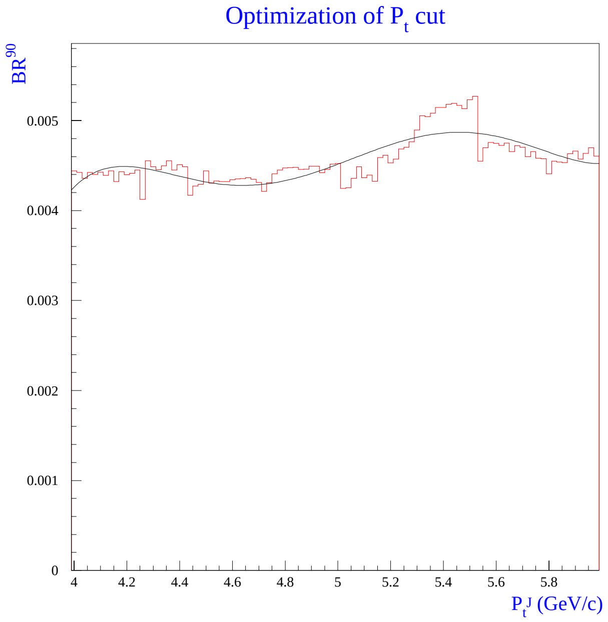

Figure 7.3: .
Study of the cut on the variable $P_T^{J/\psi}$. *We report the estimate on the expectation value of the achievable limit at 90% of* confidence level *on the* branching ratio $\mathcal{B}(B_s \to J/\psi\eta)$ *as a function of the cut value on this variable. The superimposed curve is a polynomial fit, added only to guide the eye.*

the limit, as a function of the P_T cut, is visible; a cut at 4.5 GeV/c seems to be placed in the middle of the wide plateau present between 4 and 5 GeV/c.

We then fix the request at $P_T > 4.5$ GeV/c. The expected background is then equal to $N_{bgr} \times F_{trig} = 4.5 \pm 2.3$ events, and the expectation value of the limit at 90% that can be extracted is of $N^{90\%} = 9.0$ eventi, which corresponds to approximatively $\mathcal{B}(B_s \to J/\psi\eta) < 4.1 \times 10^{-3}$.

7.2.5 k factor calculation

As we previously discussed, the candidates selection for the two decay channels $B_u \to \mu\mu K$ and $B_s \to \mu\mu\gamma\gamma$ is composed by a common part and by a part specific of each process, and in the *branching ratio* calculation the common part cancels, substantially reducing the sources of systematic errors (luminosity, b-quark production cross section σ_b, trigger acceptance, muon identification, kinematic selection on the J/ψ, *branching ratio* $\mathcal{B}(J/\psi \to \mu\mu)$).

The cancellation is complete only as far as concerns the integrated luminosity, the σ_b and the *branching ratio* $\mathcal{B}(J/\psi \to \mu\mu)$, while, in principle, the different production processes of B_s and $B^{\pm}$ mesons and the Q-value of their decay can cause differences in acceptance on the muons selection and on the kinematic requests on the J/ψ meson. In conclusion, these differences are difficult to evaluate since they depend on the production spectra which are not perfectly known. Fortunately these are just small effects, which we

k factor	
$\epsilon_b(B_u)$	k
0.0063	0.914 ± 0.009
0.002	1.068 ± 0.010
$k = 0.914 \pm 0.077$	

Table 7.1: *k factor evaluated for $\epsilon_b(B_u) = 0.0063$ and 0.002. The error on single determinations is only statistic; we assume as total uncertainty on k the half difference between the two determinations.*

decided to group in a k factor. This term is defined as:

$$k = \frac{\epsilon_{Trigger}(\psi K)}{\epsilon_{Trigger}(\psi\eta)} \cdot \frac{\epsilon_{\mu\mu}(\psi K)}{\epsilon_{\mu\mu}(\psi\eta)}$$

where the efficiencies on the right hand side are the ones defined in section 3.1 and that we encountered in equation 3.6.

For an estimation of the k value we can simply use the BGENERATOR Monte Carlo, and compare the acceptance of the kinematic cuts for the two processes $B_u \to J/\psi K$, $B_s \to J/\psi\eta$.

In order to assign a systematic uncertainty to this estimate we have to take in account the uncertainties introduced with the model used for the simulated datasets generation. BGENERATOR generates B_s and $B^{\pm}$ mesons with the same P_T spectrum, using the Peterson parametrization[6] of the momentum fraction $z = \frac{P_T^B}{P_T^b}$ transferred from the b-quark to the meson (see equation 1.1 and figure 3.3); the value we adopted in both the generations is $\epsilon_b = 0.0063$. In the calculation of the cross sections ratio for the two processes, the choice of the ϵ_b parameter is not fundamental, since the effect of the mesons P_T spectrum on the selection acceptance cancels at a first approximation. Nevertheless it is not certain that the B_s and $B^{\pm}$ mesons have the same fragmentation function: intuitively we should deem that the fraction of momentum carried by the meson is in average lower for the B_s case, since at low P_T the light quark mass could be not negligible.

As shown in table 7.1, the acceptance of the kinematic cuts for the process $B^{\pm} \to J/\psi K^{\pm}$ undergoes a quite significant variation in choosing $\epsilon_b = 0.002$, which raise the average P_T. Since this value is not in disagreement with the CDF experimental data for the B hadron differential cross section production measurements $d\sigma/dP_T$[7], we then decide to estimate the systematic error on the k factor by varying, as said, the ϵ_b parameter in the $B^{\pm}$ mesons generation. By using this prescription results $k = 1.068$, this value is quite different from the one previously estimated. Still, we have to notice that, although the value $\epsilon_b = 0.002$ is not in disagreement with the experimental data, assuming for the B_s and $B^{\pm}$ two values at the extrema of the acceptable interval for the Peterson parameter is a drastic choice. Besides, there is for sure a partial correlation between this variation and the error on the f_u/f_s ratio determined at CDF, which again depends obviously on the model assumed for the fragmentation.

Finally we decide to assume as total uncertainty on k the half difference between the two determinations, i.e. $k = 0.914 \pm 0.077$. Considering as uncorrelated the uncertainty on k and the one on the f_u/f_s ratio is then a conservative choice for the limit calculation, since we ignore the details related to the different B_s and $B^{\pm}$ productions.

7.3 *branching ratio* limit extraction

7.3.1 Ingredients for the calculation

After the event selection accepted by triggers and after all the kinematic requests, included the requests $P_T^{J/\psi} > 4.5$ GeV/c and $c\tau^*_{J/\psi} > 100$ μm and the cuts on the reconstructed masses $|M_{\mu\mu} - 3.097| < 0.03$ GeV/c^2, $|M_{\gamma\gamma} - 547| < 80$ MeV/c^2, and $|M_{\mu\mu\gamma\gamma} - 5.37| < 0.09$ GeV/c^2, we observe 4 candidates with an expected background equal to 4.0 ± 2.5 events.

For the calculation of *branching ratio* limit which corresponds to these value we have to collect all the statistic and systematic uncertainties on the factors which appear on the formula we rewrite here: $\mathcal{B}(B_s \to J/\psi\eta) \leq k\frac{f_u}{f_s}\frac{N^{90\%}_{B_s}}{N_{J/\psi K}}\frac{\mathcal{B}(B_u \to J/\psi K)}{\mathcal{B}(\eta \to \gamma\gamma)}\frac{\epsilon_K}{\epsilon_{\gamma\gamma}}$

In the `POILIM` algorithm, the calculation of the upper limit $N^{90\%}_{B_s}$ on the number of events $B_s \to J/\psi\eta$ absorbs the total effect of the uncertainties on all the factors that contributes to the determination of the limit on the *branching ratio*. We here resume these values:

- $\sigma_{f_u/f_s} f_s/f_u = 0.162$;
- $\sigma_{\mathcal{B}(\eta\to\gamma\gamma)}/\mathcal{B}(\eta \to \gamma\gamma) = 0.007$;
- $\sigma_{\mathcal{B}(B_u\to J/\psi K)}/\mathcal{B}(B_u \to J/\psi K) = 0.050$;
- $\sigma_{\epsilon_K}/\epsilon_K = 0.034$;
- $\sigma\epsilon_{\gamma\gamma}/\epsilon_{\gamma\gamma} = 0.087$;
- $\sigma k/k = 0.085$;
- $\sigma_{\epsilon_{M_\eta}}/\epsilon_{M_\eta} = 0.060$;
- $\sigma_{\epsilon_{M_{B_s}}}/\epsilon_{M_{B_s}} = 0.011$;
- $\sigma_{N_{B_u}/N_{B_u}} = 0.099$;

The total uncertainty to insert in `POILIM`, in the hypothesis of no correlation among these elements, can be calculated by summing them in quadrature and results 36.6%.

7.3.2 Results and comments

The result of the calculation of the *branching ratio* limit is the following:

$$N^{90\%}_{J/\psi\eta} = 7.132;$$
$$\mathcal{B}(B_s \to J/\psi\eta) < 3.0 \cdot 10^{-3}$$

This result improves the previous limit, obtained by the L3 experiment in 1997 [11]. However we have to say that the value here adopted for the f_u/f_s ratio, obtained by the CDF measurements, ($f_u/f_s = 2.35 \pm 0.75$) leads to a better limit than the one obtained with the f_u/f_s world average presented in the summer 2002[2] by the LEP Working Group ($f_u/f_s = 4.31 \pm 0.54$). If we don't consider the possibility that the B_s and $B^\pm$ meson production ratios depend on the primary interacting particles, hypothesis that could explain the disagreement between the CDF measurement and the other measurements at the e^+e^- colliders, we can recalculate the limit on the *branching ratio* assuming the LEP Working Group result. In this case the total acceptance uncertainty is equal to 21.83%. and the limit is:

$$N^{90\%}_{J/\psi\eta} = 6.202;$$
$$\mathcal{B}(B_s \to J/\psi\eta) < 4.8 \cdot 10^{-3}$$

We prefer not to discard or accept any of the two measurements, since both the choices present pros and cons: from a methodological point of view, a measurement of f_u/f_s obtained in the same experimental environment should be more desirable; the most conservative choice however is to use the highest value, which is subject to a lower relative uncertainty.

At the end of the discussion we present also the calculation of the limit on the *branching ratio* without the background subtraction. Using the CDF estimate for f_u/f_s the result is:

$$N^{90\%}_{J/\psi\eta} = 10.65;$$
$$\mathcal{B}(B_s \to J/\psi\eta) < 4.5 \cdot 10^{-3}$$

Bibliography

[1] T. Affolder *et al.*, "Measurement of b-Quark Fragmentation Fractions in $p\overline{p}$ Collisions at $\sqrt{s} = 1.8$ TeV", *Phys. Rev. Lett.* **84**, 1663 (2000)

[2] "31st International Conference on High Energy Physics, ICHEP02, Amsterdam (The Netherlands)", July 24-31, 2002
see also:
ALEPH, CDF, DELPHI, L3, OPAL, SLD, "Combined results on b-hadron production rates and decay properties", CERN-EP/2001-050, Jun 2001

[3] K. Hagiwara *et al.*, "Review of Particle Physics", *Phys. Rev. D* **66**, 010001 (2002)

[4] P. Z. Skands, "Branching ratios for $B_{d,s} \to J/\psi\eta$ and $B_{d,s} \to \eta\ell^+\ell^-$, extracting γ from $B_{d,s} \to J/\psi\eta$, and possibilities for constraining C_{10A} in semileptonic B decays", *J. High Energy Phys*, 01 008 (2001)

[5] J. Neyman, *Phil. Trans. Royal Soc. London A*, **236**, 333 (1937)
reprinted in:
A Selection of Early Statistical Papers on J.Neyman, University of California Press, Berkeley 1967

[6] G. Zech, "Upper limits in experiments with background or measurement errors", *Nucl. Instr. Meth. Phys. A* **277**, 608 (1989)

[7] T. Huber *et al.*, "Search for mixing of muonium and antimuonium", *Phys. Rev. D* , 2709 (May 1990)

[8] R. Cousins, mnm "Why Isn't Every Physicist a Bayesian?" *Am. J. Phys.* **63**, 398 (1995)

[9] R. Cousins, V. Highland, "Incorporating systematic uncertainties into the upper limit" *Nucl. Instr. Meth. Phys. Res. A* **320**, 331 (1992)

[10] J. Conway, K. Maeshima, "Upper Limits on Poisson Processes Incorporating Uncertainties in Acceptance and Background", **CDF** internal note **4476**, (Oct 1998)

[11] M. Acciari *et al.* (L3 Collaboration), "Search for exclusive B decays to J and η or π^0 with the L3 detector", *Phys. Lett. B* **391**, 481-490 (1997)

Conclusions and Run II and perspectives

The study of the $B_s \to J/\psi\eta$ decay in the dataset collected at CDF during Run Ib ($\sim 90\text{pb}^{-1}$) led to the extraction of a limit on the *branching ratio* which is competitive with the only currently existing measurement, performed at the L3 experiment (LEP).
By using the value obtained at CDF for the B_u and B_s meson fragmentation fraction, f_u/f_s, we estimated a 90% C.L. limit equal to:

$$\mathcal{B}(B_s \to J/\psi\eta) < 3 \cdot 10^{-3}$$

This measurement has been mainly limited by the uncertainty on the fragmentation ratio and by the poor energy resolution of the CDF electromagnetic calorimeter. In fact, most of our efforts have been devoted to the reconstruction of low energy photons in a calorimeter not designed for this application.

This study can be considerer as a first step of an analysis aimed to reconstruct B_s meson decays to the CP final eigenstates $B_s \to J/\psi\eta$ and $B_s \to J/\psi\eta'$. For this second channel the theoretical expectations provide a *branching ratio* higher (by a factor $1.5-2$) than the first channel; the final state can be fully identified by the η' reconstruction in one of the two decays:

- $\eta' \to \rho^0\gamma$
  final state with one photon and two charged pions

- $\eta' \to \eta\pi^+\pi^-$
  in this case the η is reconstructed as in the direct decay $B_s \to J/\psi\eta$ and then two opposite charge tracks (pions) are attached to obtain the η'.

With the data under collection since the beginning of this year, CDF aims not only for the reconstruction of these channels, but also for the measurement of a CP violation in these decays, which will provide a direct measurement of the χ angle (see equation 1.63) of the CKM **sb** triangle.
In the Standard Model picture the asymmetry expectation is quite small, of the order of few percents. A precise study of the CDF sensitivity is now in progress for all the described channels, but a preliminary analysis on the $B_s \to J/\psi\eta$ channel highlighted that it will be very difficult to observe the asymmetry; nevertheless, the measurement of a value higher than $\mathcal{O}(\lambda^2)$ will provide an unambiguous signal of new physics beyond the Standard Model. For this reason not only CDF, but also future experiments as BTeV and LHCB, are interested on this measurement.

During the Run II CDF expects to collect 2 fb^{-1} of new data, in comparison to the Run I this means roughly an increase of a factor 20 in the integrated luminosity. To the gain in term of pure statistic we have to add the major upgrades on the CDF detector, in particular regarding the tracking system.
The new SVXII microvertex detector is now 96 cm long and covers approximatively 2.5 σ of the interaction region, reaching a $b-tagging$ acceptance close to 100% (where the Run I had a value around 60%). Besides, the increase in the number of layers and, more important, the use of double side sensors improves the *pattern recognition*.
Just outside SVXII has been also added the ISL detector[2], a two layers silicon device, the inner one with a coverage of $|\eta| < 1$ and the outer one of $1 < |\eta| < 2$ so that to compensate to the lack of efficiency of the COT at high rapidities. The core of the tracking system at CDF is the drift chamber, COT, which covers the region $|\eta| < 1$. The coverage of the μ chambers has been extended up to $|\eta| < 1.5$ and also the azimuthal coverage of CMX has increased. These improvements provide also an increase in the acceptance and efficiency for the $J/\psi \to \mu^+\mu^-$ selection, for a global factor equal to 3.6. This increase is related also to the changes on the requests applied at trigger level by the XFT[3] which requires a transverse momentum $P_T(\mu) > 1.5$ GeV/c for the μ candidates pointing to CMU chambers ($P_T(\mu) > 2.0$ GeV/c for the CMX); also, the minimum azimuthal separation allowed has been halved to $\Delta\phi = 2.5°$.
Besides, the increase of the center of mass energy to 2 TeV on the Run II implies a corresponding increase of around 10% in the b production cross section. CDF is also studying the possibility to design a trigger for the $J/\psi \to e^+e^-$ signal which will increase the available dataset by almost 50%.

Putting all these factors together (see also [1]), we can estimate the number of expected events for the $B_s \to J/\psi\eta$ channel by extrapolating from the number of expected events for the $B^\pm \to J/\psi K^\pm$ channel. During the whole Run I a total of ~ 400 $B^\pm \to J/\psi K^\pm$ events has been reconstructed; given the gain factors for the Run II we expect to be able to reconstruct approximatively 50000 events.
Figure 7.4 shows the events (around 150) reconstructed in the first 18 pb^{-1}; the procedure here used applies cuts which are slightly different from the ones applied for the signal estimation, and also it must be noticed that during the first period of data taking only a limited portion of the μ detector and of the silicon tracker were active. In order obtain an estimation of the expected number of events for the $B_s \to J/\psi\eta$ in 2 fb^{-1} we can again use the relation 3.4, relation yet used for the BR limit extraction. Assuming $f_s/f_u = 0.426$, value used at CDF for all the Run II estimations, and $\mathcal{B}(B_s \to J/\psi\eta) = 5 \times 10^{-4}$, the number of expected events is equal to 1100. This evaluation takes into account only the $B_s \to J/\psi\eta$ decay with $\eta \to \gamma\gamma$.

We discuss here a possible photon reconstruction strategy alternative to the calorimetric measurement. This strategy is based on the photon reconstruction using $\mathrm{e}^+\mathrm{e}^-$ conversions. This methodology has yet been used during the CDF Run I for the reconstruction of radiative decays $B_d \to K^{*0}\gamma$, $B_s \to \phi\gamma$ and $\Lambda_b \to \Lambda\gamma$ [2], leading to really good results in terms both of efficiency both of resolution, since the energy measurement is based on the tracking system.
On the Run II the conversion probability is increased with respect to the Run I since a photon has to face a larger amount of material before to enter the central drift chamber

[2] *Intermediate Silicon Layer.*
[3] *EXtra Fast Tracker*; in the Run II the COT infos can be used for the Level 1 decision.

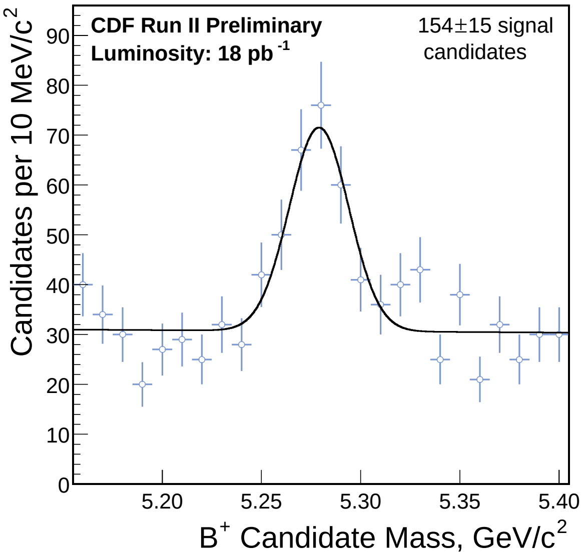

Figure 7.4: $B^{\pm} \to J/\psi K^{\pm}$ *invariant mass distribution for data in Run II.*

(a preliminary estimate quotes the increment to be around 30%). In figure 7.5 we show the material distribution as a function of the distance from the beam line for the Run II data (left) and Run I data (right).

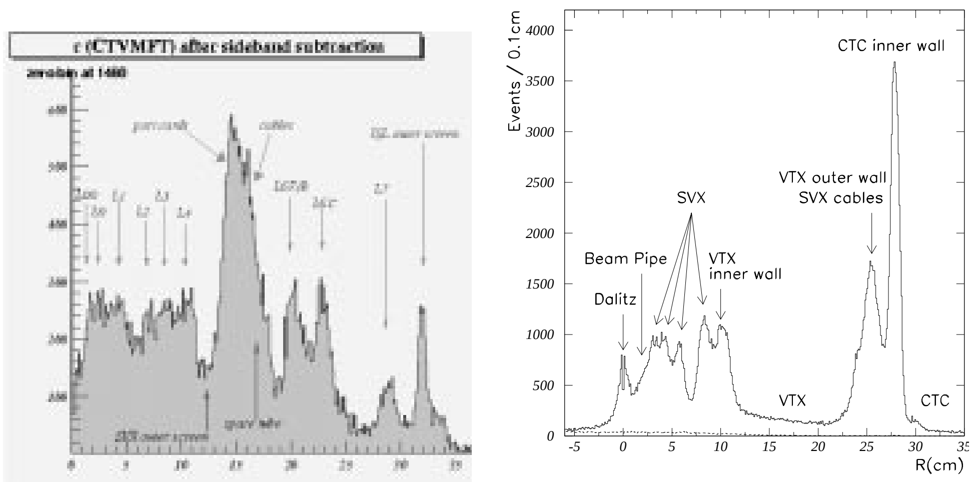

Figure 7.5: *Distribution of the inert material as a function of the distance from the beam line as evaluated from data for the Run II (left) and Run I (right).*

The use of this technique can be usefully extended, with some good sense, also to the study of the channel $B_s \to J/\psi\eta$ with $J/\psi \to \mu\mu$ and $\eta \to \gamma\gamma$. The presence of two photons to be reconstructed prevents, in term of efficiency, requiring two conversions in the same event, it is instead possible to reconstruct one photon in the calorimeter and the second one using its conversion in e^+e^-. This method presents some advantages. In the first place the presence of two photon in the event (almost) doubles the probability to have a conversion. Secondly, by means of the kinematic fit, where the η particle mass is constrained, all the momenta in the event will end to have the resolution of the tracking system since the measurement of the photon energy in the calorimeter results to be the only independent variable affected by a relevant error before to apply the mass constraint. An approximative estimation based on a toy Monte Carlo provides an increase on the resolution on the B_s invariant mass close to a factor 2.

It is instead difficult to give an estimation of the events we expect to reconstruct in the channels of $B_s \to J/\psi\eta'$ since for this calculation the efficiency reconstruction for soft pions must be known, and now is not. Still, can be useful to report the number of events that BTeV estimates to reconstruct with an integrated luminosity of 2 fb^{-1} in the different channels to have an idea of the various contributions; we have nevertheless to keep in mind that BTeV will use a totally different detector from the CDF one, with very good electromagnetic calorimeter which will allow to reconstruct neutral particles with good efficiency and purity down to 300 MeV momenta [1].

	$\eta \to \gamma\gamma$	$\eta' \to \gamma\rho^0$	$\eta' \to \eta\pi^+\pi^-$
N^o of events	1920	5670	1610

Table 7.2: *Number of expected events $B_s \to J/\psi\eta^{(')}$ in 2fb^{-1} from BTeV*

We can then estimate that BTeV can reconstruct around 9000 events and that after the B flavor tagging reduce to around 900. Besides, assuming to have a spatial resolution good enough to be able to resolve the B_s oscillation, the error on $\sin(2\chi)$ results equal to 0.033.

These considerations suggest that the CP violation measurements beyond the first unitarity triangle at the Tevatron and in particular at CDF will be performed at the edge of the experimental sensitivity, but also that they could open a window through phenomena of new physics beyond the Standard Model.

Bibliography

[1] "B Physics at the Tevatron: Run II and Beyond" Fermilab-Pub-01/197.

[2] D. Acosta *et al.*, (CDF Collaboration), "Search for Radiative b-Hadron Decays in $p\bar{p}$ Collisions at $\sqrt{s} = 1.8$ TeV, FERMILAB-PUB-02/146-E. Submitted to *Phys. Rev. D* (June 2002)

Appendix

Kinematic fit

General issues

The kinematic fit we used is a least square interpolation, so it searches for a set of m parameters α_i which minimizes the function

$$\chi^2 = \sum_l \frac{(y_l - f_l(\alpha))^2}{\sigma_l^2},$$

where the measured quantities are y_l, the functional relation $y_l = f_l(\alpha_i)$ and σ_l are the errors on the measurements. The request for having a minimum on the χ^2 is guaranteed by the m equations

$$\frac{\partial \chi^2}{\partial \alpha_i} = 0.$$

These equations might be non linear, as a function of the parameters α_i, and then there is no general method for finding the solution. The procedure here adopted doesn't look for the solutions of these equations, but the solutions for equations derived after a power series expansion, to the first order, around an approximate solution:

$$f_l(\alpha) = f_l(\alpha_A) + \sum_i (\alpha_i - \alpha_{iA}) \frac{\partial f_l(\alpha)}{\partial \alpha_i}\bigg|_{\alpha_A} \equiv f_{lA} + \sum_i A_{li}\eta_i.$$

With this approximation the χ^2 can be rewritten as

$$\chi^2 = \sum_l \frac{(y_l - f_{lA} - \sum_i A_{li}\eta_i)^2}{\sigma_l^2} \equiv \sum_l \frac{(\Delta y_l - \sum_i A_{li}\eta_i)^2}{\sigma_l^2}$$

At this point it is useful to introduce a matrix notation

$$\chi^2 = (\mathbf{\Delta y} - \mathbf{A}\eta)^t \mathbf{V}_y^{-1} (\mathbf{\Delta y} - \mathbf{A}\eta)$$

where $\mathbf{A}$ is the matrix of A_{ij} elements defined before and $\mathbf{V}_y^{-1}$, η, $\mathbf{y}$ are given by

$$\mathbf{V}_y^{-1} = \begin{pmatrix} 1/\sigma_1^2 & 0 & \cdots & 0 \\ 0 & 1/\sigma_2^2 & \cdots & 0 \\ \vdots & \vdots & \ddots & \vdots \\ 0 & 0 & \cdots & 1/\sigma_n^2 \end{pmatrix}, \quad \eta = \begin{pmatrix} \eta_1 \\ \eta_2 \\ \vdots \\ \eta_m \end{pmatrix}, \quad \mathbf{y} = \begin{pmatrix} y_1 \\ y_2 \\ \vdots \\ y_n \end{pmatrix}.$$

Calculating the partial derivatives of the χ^2 with respect to the parameters η we obtain the m equations

$$\mathbf{A}^t\mathbf{V}_y^{-1}(\mathbf{\Delta y} - \mathbf{A}\eta) = \mathbf{0},$$

defining $\mathbf{V}_A = (\mathbf{A}^t\mathbf{V}_y^{-1}\mathbf{A})^{-1}$ we obtain

$$\eta = \mathbf{V}_A\mathbf{A}^t\mathbf{V}_y^{-1}\mathbf{\Delta y},$$

The value of the parameters α after the fit can be simply obtained by $\boldsymbol{\alpha} = \boldsymbol{\alpha_A} + \boldsymbol{\eta}$

Constrained fit

If the physics of the studied process provides further informations, for example that two tracks originate from a common vertex, or have a defined invariant mass, it is useful to introduce a mechanism that exploit these informations.
Generally speaking, a set of r constraints can be described by means of equations like:

$$\mathbf{H}(\alpha) = \mathbf{0}.$$

Coherently with the procedure introduced before we can expand to the first order around an α_A and obtain the linearized equations

$$\mathbf{H}(\alpha_A) + (\alpha - \alpha_A)\partial\mathbf{H}(\alpha_A)/\partial\alpha \equiv \mathbf{D}\eta + \mathbf{d} = \mathbf{0},$$

where $\mathbf{D}$ is a $r \times m$ matrix, $\mathbf{d}$ is a vector of r elements.
The search for a maximum or a minimum in a manifold defined by constraints is a problem that can be faced using the *Lagrange multipliers* method. In order to take into account the presence of the constraints in the calculation of the minimum a new term is added to the χ^2,

$$\chi^2 = (\mathbf{\Delta y} - \mathbf{A}\eta)^t\mathbf{V}_y^{-1}(\mathbf{\Delta y} - \mathbf{A}\eta) + 2\lambda^t(\mathbf{D}\eta + \mathbf{d});$$

the search is then performed by equating to zero the partial derivatives calculated with respect to η and λ. The equation $\partial\chi^2/\partial\lambda = \mathbf{0}$ generates the constraint conditions. The solution to the equations shows that η is equal to η_0 plus a term proportional to λ, so the constraints move the η parameters from their unconstrained values η_0. This result suggests that the solution might be "factorized" in two terms:
- as a first step we solve the unconstrained equations, looking for η_0
- then we apply the constraints and we find η in terms of η_0.

All the uncertainties on the data measurement had been absorbed into the $\mathbf{V}_{\eta_0} = \mathbf{V}_A$ matrix.
After some algebra the χ^2 can e rewritten as

$$\chi^2 = (\mathbf{\Delta y} - \mathbf{A}\eta_0)^t\mathbf{V}_y^{-1}(\mathbf{\Delta y} - \mathbf{A}\eta_0) + (\eta - \eta_0)^t\mathbf{V}_{\eta_0}^{-1}(\eta - \eta_0) + \lambda^t(\mathbf{D}\eta + \mathbf{d}).$$

The first term is constant and is the χ^2 for the unconstrained fit. The method here adopted moves from the values obtained from the unconstrained fit and then introduces the constraints using a new χ^2

$$\chi^2 = (\eta - \eta_0)^t\mathbf{V}_{\eta_0}^{-1}(\eta - \eta_0) + 2\lambda^t(\mathbf{D}\eta + \mathbf{d}).$$

The equations $\partial\chi^2/\partial\eta = \mathbf{0}$ and $\partial\chi^2/\partial\lambda = \mathbf{0}$ give

$$\begin{aligned} \mathbf{V}_{\eta_0}^{-1}(\eta - \eta_0) + \mathbf{D}^t\lambda &= \mathbf{0} \\ \mathbf{D}\eta + \mathbf{d} &= \mathbf{0} \end{aligned}$$

which, when solved, give

$$\begin{aligned} \lambda &= \mathbf{V}_D(\mathbf{D}\eta_0 + \mathbf{d}) \equiv \mathbf{V}_D\alpha \qquad (\alpha = \mathbf{D}\eta_0 + \mathbf{d}) \\ \eta &= \eta_0 - \mathbf{V}_{\eta_0}\mathbf{D}^t\lambda \\ \mathbf{V}_D &= (\mathbf{D}\mathbf{V}_{\eta_0}\mathbf{D}^t)^{-1} \\ \mathbf{V}_\lambda &= \mathbf{V}_D \\ \mathbf{V}_\eta &= \mathbf{V}_{\eta_0} - \mathbf{V}_{\eta_0}\mathbf{D}^t\mathbf{V}_\lambda\mathbf{D}\mathbf{V}_{\eta_0}. \\ \chi^2 &= \lambda^t\mathbf{V}_D^{-1}\lambda = \alpha^t\mathbf{V}_D\alpha = \lambda^t\alpha = \alpha^t\lambda \end{aligned} \qquad (*)$$

Application to $B_s \to J/\psi\eta$

The $B_s \to J/\psi\eta$ has a 4 bodies final states; two charged tracks and two photons. The two tracks from the μ have been previously interpolated by another *vertex-constrained* kinematic fit providing the following variables to define the dimuon system:

y_1	X_{SV}	X coordinate of secondary vertex
y_2	Y_{SV}	Y coordinate of secondary vertex
y_3	Z_{SV}	Z coordinate of secondary vertex
y_4	$C(\mu_1)$	First track curvature
y_5	$\phi_0(\mu_1)$	μ_1 direction in xy at the point of minimum approach
y_6	$cot\theta(\mu_1)$	Cotangent of the polar angle at the minimum approach of μ_1
y_7	$C(\mu_2)$	Second track curvature
y_8	$\phi_0(\mu_2)$	μ_2 direction in xy at the point of minimum approach
y_9	$cot\theta(\mu_2)$	Cotangent of the polar angle at the minimum approach of μ_2

These variables describe completely a two track system originating from the same vertex. Besides, the fit provides the covariant matrix $\mathbf{V}_y^{9\times 9}$ for this block of variables.
The two photons on the final state are described by means of their (common) origin that is assumed to be the secondary vertex, the reconstructed position on the CES that is defined by the local coordinates X_{loc} and Z_{loc} and by their energy red on the calorimeter (after the recalibration). The remaining 6 variables are then:

y_{10}	$E_{\gamma 1}$	first photon energy
y_{11}	X_{loc1}	X local coordinate on the CES for the first photon
y_{12}	Z_{loc1}	Z local coordinate on the CES for the first photon
y_{13}	$E_{\gamma 1}$	second photon energy
y_{14}	X_{loc2}	X local coordinate on the CES for the second photon
y_{15}	Z_{loc2}	Z local coordinate on the CES for the second photon

The covariant matrix for these quantities is assumed to e diagonal and given by:

$$\begin{aligned} \sigma_{E_\gamma}^2 &= E_\gamma^2\left(\frac{0.02}{E_\gamma}\right)^2 + \frac{0.135^2}{E_{T\gamma}} \\ \sigma_{X_{loc}}^2 &= \frac{(Pitch_X)^2}{12} \\ \sigma_{Z_{loc}}^2 &= \frac{(Pitch_Z)^2}{12} \cdot \frac{1}{sin(\theta)} \end{aligned}$$

The $\mathbf{V}_y$ matrix takes the shape:

$$\left(\begin{array}{c|c} 9\times 9 & \dots \\ \text{CTVMFT} & \mathbf{0} \\ cov.\quad matrix & \dots \\ \hline \dots & 6\times 6 \\ \mathbf{0} & \gamma \\ \dots & diagonal\quad matrix \end{array}\right)$$

After defining the 15 variable y_l and their covariance matrix we still have to define the α_i parameters. These are

$$\begin{array}{lll} \alpha_1 = X_{SV} & \alpha_4 = p_x^{\mu 1} & \alpha_7 = p_x^{\mu 2} \\ \alpha_2 = Y_{SV} & \alpha_5 = p_y^{\mu 1} & \alpha_8 = p_y^{\mu 2} \\ \alpha_3 = Z_{SV} & \alpha_6 = p_z^{\mu 1} & \alpha_9 = p_z^{\mu 2} \end{array}$$

$$\begin{array}{ll} \alpha_{10} = q_x^{\gamma 1} & \alpha_{13} = q_x^{\gamma 2} \\ \alpha_{11} = q_y^{\gamma 1} & \alpha_{14} = q_y^{\gamma 2} \\ \alpha_{12} = q_z^{\gamma 1} & \alpha_{15} = q_z^{\gamma 2} \end{array}$$

Since these parameters are as much as the variables this implies that they can be exactly calculated from $\mathbf{y}$ without need for an interpolation. The constraints on the $M_{\mu\mu}$ and $M_{\gamma\gamma}$ invariant mass are then introduced for the two requirements :

$$\begin{aligned} \mathrm{H}_1 &= 2\cdot(E_{\mu 1}E_{\mu 2} - \overline{p}_{\mu_1}\cdot\overline{p}_{\mu_2} + M_\mu^2) - M_{J/\psi}^2 = 0 \\ \mathrm{H}_2 &= 2\cdot(E_{\gamma 1}E_{\gamma 2} - \overline{q}_{\gamma_1}\cdot\overline{q}_{\gamma_2}) - M_\eta^2 = 0 \end{aligned}$$

The request for a common originating vertex for μ and photons is yet present since on the two tracks has been applied a *vertex constrained* fit, while the photons have the origin on the secondary vertex by construction.
Now we have all the ingredients to proceed with the calculation. The values of the 15 $\boldsymbol{\alpha}$ parameters obtained by inversion from the 15 $\mathbf{y}$ parameters become the initial $\boldsymbol{\alpha_A}$ values around which to expand both the χ^2 equations both the $\mathbf{H}$ constraints.

The whole interpolating procedure is now only a boring calculation of the matrices $\mathbf{D}(2\times 15)$ and $\mathbf{A}(15\times 15)$. The result of the fit is then obtained by matrix manipulation using $\mathbf{V}_{\eta_0} = (\mathbf{A}^T\mathbf{V}_y^{-1}\mathbf{A})^{-1}$ and the formulas (*) listed in the previous section.

List of Figures

List of Tables

Ringraziamenti

Scrivo questa pagina in italiano di proposito. Sono ringraziamenti sentiti, che voglio esprimere nella mia lingua.

Sono molte le persone che devo ringraziare al termine di questo lavoro.

Il gruppo di CDF di Padova in toto mi ha supportato durante questi tre e più anni di dottorato, come aveva fatto durante il mio periodo di tesi di laurea. È un gruppo dalle caratteristiche eccezionali, che riunisce in sè competenza, entusiasmo, umanità.

Un ringraziamento particolare lo devo al prof. Bisello e al prof. Busetto che hanno continuato a spronarmi anche durante i momenti più difficili. Se sono qui ora a scrivere questa pagina lo devo in gran parte a loro.

A Donatella devo praticamente tutto quello che so ora di fisica del B, e anche qualcosa che va oltre la sola fisica.

A Nicola devo uno dei periodi più difficili, esaltanti e gratificanti che abbia mai trascorso, mentre in Tommaso, tra le altre cose, ho riconosciuto ancora l'entusiasmo per una materia che mi ha da sempre affascinato a che mi spinse ad intraprendere questa strada.

Jeff è stato elemento di stabilità durante tutto l'ultimo anno di tesi e in particolare durante le ultime concitate fasi di stesura.

Luca è stato mio prezioso compagno di ventura durante l'intero dottorato, mentre ad Andrea devo la amichevole presenza durante le, non poche, notti insonni trascorse al lavoro all'interno del dipartimento.

Un ringraziamento infine va a tutti i "ragazzi" del laboratorio, in particolare a Devis, la cui lucida follia ho finito per condividere ed apprezzare.